LBL-5731

OBSERVATION OF THE FORBIDDEN MAGNETIC DIPOLE TRANSITION $6^2P_{1/2} \rightarrow 7^2P_{1/2}$ IN ATOMIC THALLIUM

Steven Chu
(Ph. D. thesis)

October 1976

Prepared for the U. S. Energy Research and Development Administration under Contract W-7405-ENG-48

LBL-5731

DISCLAIMER

OBSERVATION OF THE FORBIDDEN MAGNETIC DIPOLE TRANSITION $6^2P_{1/2} \rightarrow 7^2P_{1/2}$ IN ATOMIC THALLIUM

BY

Steven Chu

Lawrence Berkeley Laboratory
University of California
Berkeley, California 94720

This work was done with support from the U. S. Energy Research and Development Administration.

CONTENTS

ABSTRACT v

I. INTRODUCTION 1

A. Neutral Currents in Atomic Physics 2

B. Parity Violation in Atomic Transitions 8

C. Outline of the Experiment 10

II. THEORY 14

A. Outline of the M1 Calculation 14

1. Relativistic Corrections 14

2. Hyperfine Mixing 19

3. Configuration Mixing 21

B. M1-Stark E1 Interference 25

III. EXPERIMENTAL METHOD 37

A. Description of the Laser 40

1. Laser Head and Dye System 40

2. Electrical Discharge Circuit 43

3. Optical Cavity 52

4. Generation of U-V Light 55

B. Thallium Cell and Oven 57

C. Counting Electronics 64

D. Data Handling 66

IV. EXPERIMENTAL RESULTS 68

A. Field-Induced E1 Transition 68

B. E1-M1 Asymmetry 75

1. Cascade Depolarization 79

2. Resonance Trapping of 535 nm Light 83

3. Collisional Depolarization 85

4. Instrumental Depolarization 87

5. Experimental Value for the M1 Matrix Element 89

V. BACKGROUNDS 91

A. Backgrounds Not Involving Thallium 91

B. Electric Field Dependent Background 93

C. Electric Field Independent Background 96

D. Possible Sources for the Zero-Field Background 100

1. Rayleigh Scattering 100

2. Raman Transitions 100

3. Collision Induced Transitions 102

4. Molecular Transitions 106

VI. FUTURE EXPERIMENTS 108

ACKNOWLEDGEMENTS 109

REFERENCES 110

OBSERVATION OF THE $6^2P_{1/2} - 7^2P_{1/2}$ TRANSITION IN THALLIUM

Steven Chu

Materials and Molecular Research Division, Lawrence Berkeley Laboratory
and Department of Physics, University of California
Berkeley, California 94720

ABSTRACT

This thesis describes a measurement of the $6^2P_{1/2} \rightarrow 7^2P_{1/2}$ forbidden magnetic dipole matrix element in atomic thallium. A pulsed, linearly polarized dye laser tuned to the transition frequency is used to excite the thallium vapor from the $6^2P_{1/2}$ ground state to the $7^2P_{1/2}$ excited state. Interference between the magnetic dipole M1 amplitude and a static electric field induced E1 amplitude results in an atomic polarization of the $7^2P_{1/2}$ state, and the subsequent circular polarization of 535 nm fluorescence. The circular polarization is seen to be proportional to $\langle M1 \rangle / \langle E1 \rangle$ as expected, and measured for several transitions between hyperfine levels of the $6^2P_{1/2}$ and $7^2P_{1/2}$ states. The result is

$$\langle M1 \rangle = -(2.11 \pm 0.30) \times 10^{-5} \frac{|e|\hbar}{2mc} ,$$

in agreement with theory.

I. INTRODUCTION

Neutral currents, originally predicted by gauge theories of weak interactions of Weinberg (Wei, 67) and Salam (Sal, 1968), have been observed in high energy neutrino experiments at CERN, (Has, 73), FNAL (Ben, 74), (Bar, 74) (Bar, 75b), ANL (Bar, 75) and BNL (Lee, 75). Details of the experiments are given in a review by Cundy, (Cun, 74). The experiments all measure muon-less reactions between muon neutrinos ν_μ and nucleons of the form

$$\nu_\mu + N \rightarrow \nu_\mu + N' \ . \tag{1}$$

Although the neutral current may have the familiar V-A form of the charged current, various combinations of V and A have been suggested as alternatives to the Weinberg-Salam model (Wei, 71), (Sak, 74), (Che, 74). Other authors have observed that scalar, pseudoscalar, and tensor terms are also consistent with the data, (Kin, 74, 75), (Kay, 74), (Yan, 74), (Big, 74).

Tests for parity violation of neutral currents in high energy physics have been limited so far to the measurement of the ratio, R_ν, of the neutral current cross-section, given by Eq. (1), and the charged current cross-section,

$$\nu_\mu + N \rightarrow \mu + N'' \ . \tag{2}$$

By comparing R_ν to the corresponding ratio $R_{\bar{\nu}}$, the Harvard-Penn-Wisconsin group (Ben, 76) has found that muon neutrino-nucleon neutral currents are consistent with a pure V-A interaction, but the results

are three standard deviations from that expected for purely vector or axial vector couplings. Further work is in progress at FNAL to improve the cross-section measurements, but there are some reservations about conclusions that are drawn from these experiments. The calculations require that the reactions of ν ($\bar{\nu}$) to nucleons differ only by their left (right) handed helicities. Also, R_ν and $R_{\bar{\nu}}$ are assumed to have the same energy dependence, but there is only fragmentary evidence to support this claim.

A. Neutral Currents in Atomic Physics

In contrast to the reactions in Eq. (1) neutral current weak interactions between the charged leptons $\mu^\pm$, $e^\pm$ and hadrons have not been observed. A great deal of effort is now being spent on tests of these currents in atomic physics (Jar, 74), (Bro, 76), (Bou, 76). Although parity violation due to weak interactions was first suggested by Zel'dovich more than fifteen years ago (Zel, 59), and subsequently discussed by Drell and Sullivan (Dre, 65) and Curtis-Michel (Mic, 65), intense interest did not develop until a series of papers by M.A. and C.C. Bouchiat (Bou, 74a, 74b, 75a). Experimental efforts are now in progress in Oxford (Lov, 75), Seattle (Sor, 76), Berkeley (Chu, 76), and Ann Arbor (Lew, 75) as well as Paris (Bou; 75b, 76a, 76b).

The basic idea behind neutral current phenomena in atoms is simple enough. Just as a lepton can interact with a nucleon in electromagnetic interactions via a photon, (Fig. 1a) it may also interact via the weak neutral current in lowest order (Fig. 1b). Inspection of the Feynman diagrams leads us to expect a potential of magnitude $G\delta^3(x)A$,

where G is the weak coupling constant, and a is the nuclear mass number.

Even without neutral currents, higher order diagrams permit a weak

Electromagnetic Interaction (Fig. 1a.)

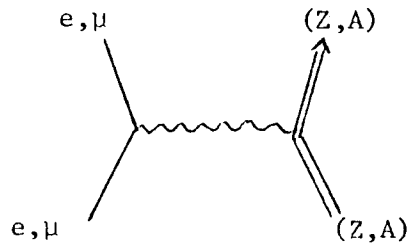

$$\text{Propagator} = \frac{1}{q^2} \Rightarrow A_\mu = \left(-\frac{Ze^2}{r}, 0\right) \text{ in coordinate space.}$$

q = momentum transfer

Neutral Current Interaction (Fig. 1b.)

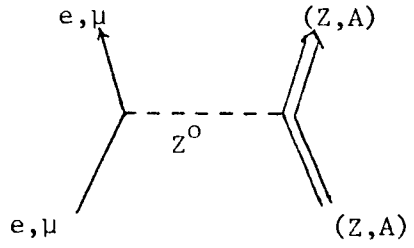

$$\text{Propagator} = \frac{1}{q^2 - M_{Z^o}^2} \approx \frac{1}{M_{Z^o}^2} \Rightarrow \text{Amp} \approx G\delta^3(x)A$$

Charge Current Interaction (Fig. 1c)

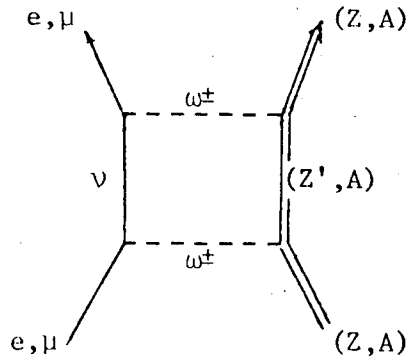

$$\text{Amp} \approx \alpha G^2 \delta^3(x)$$

charged coupling between leptons and the nucleus (Fig. 1c.), but these effects are smaller by a factor of αG relative to the neutral current diagram, and are too small to be observable.

The parity violating potential between the valence electron and the nucleus follows from a non-relativistic reduction of a relativistic current-current interaction. We use the simplest version of the $SU_2 \times U_1$ gauge model (Weinberg-Salam model) in the limit where the mass of the intermediate vector boson Z_o is infinite. Then, the effective Hamiltonian density $\mathcal{H}(x)$ is given by

$$\mathcal{H}(x) = \frac{G}{\sqrt{2}} J_\mu(x) J^\mu(x) \quad , \tag{3}$$

and the current $J_\mu(x)$ is split into the relevant leptonic part $J_\mu^{\ell}(x)$ and hadronic part $J_\mu^{h}(x)$:

$$J_\mu^{\ell}(x) = \frac{1}{2} [\bar{e}(x)\gamma_\mu e(x)(4\sin^2\theta_\omega - 1) - \bar{e}(x)\gamma_\mu\gamma_\sigma e(x) + (e \to \mu,\ \nu_e \to \nu_\mu)] \tag{4}$$

$$J_\mu^{h}(x) = J_{\mu,3}(x) + J_{\mu,3}^{5}(x) - 2\sin^2\theta_\omega\, J_\mu^{em}(x) \tag{5}$$

Here, $e(x)$, $\nu_e(x)$, etc... represent the Dirac fields of the electron, neutrino, etc. ...; $J_\mu^{em}(x)$ is the electric current density for hadrons, and $J_{\mu,3}(x)$, $J_{\mu,3}^{5}(x)$ are the usual hadronic isospin (axial isospin) operators. The two-component reduction (see Appendix III of (Bou, 74b)) gives the result for the parity violating non-relativistic potential

$$V_{p.V.}^{e.N.} = \frac{G}{4\sqrt{2}\, m_e} [\mathcal{Q}\cdot\mathcal{p}\ \delta^3(\mathcal{r}) + \delta^3(\mathcal{r})\mathcal{Q}\cdot\mathcal{p}] Q_\omega \tag{6}$$

with

$$Q_\omega = -[(4\sin^2\theta_\omega - 1)Z + N] \tag{7}$$

m, $\frac{1}{2}\hbar\underset{\sim}{\sigma}$, $\underset{\sim}{p}$ and $\underset{\sim}{x}$ are the mass, spin, momentum and position of the electron, Z, (N) are the number of protons (neutrons) in the nucleus, and θ_ω, the so-called Weinberg angle, is a parameter in the gauge theory we are using. The $\bar{\nu}_e$-e scattering experiments (Rei, 76) give a value for $\sin^2\theta_\omega = .29 \pm .05$.

The general form of the Hamiltonian can be given a physical interpretation. First of all, the only pseudoscalar, time-reversal invariant quantity that can be constructed from the operators $\underset{\sim}{x}$, $\underset{\sim}{p}$, and $\underset{\sim}{\sigma}$ is $\underset{\sim}{\sigma}\cdot\underset{\sim}{p}$. The $\delta^3(\underset{\sim}{x})$ factor follows from the short range of the weak interaction, and Q_ω exhibits the additive effect of the nucleons coupling to the electron. Since the electron wave function at the nucleus scales $\sim Z$, the momentum P of the electron scales $\sim Z$, and the quantity Q_ω in Equation (7) scales $\sim Z$, the parity violating potential has $\sim Z^3$ dependence; thus, the parity-violating effects are enhanced in heavy atoms.

There is also a parity violating electron-electron potential and a term for interactions involving nuclear spin, but these contributions are shown to be small (Bou, 74a). Finally, there is a parity conserving term

$$V_{p.C.}^{e.N.} \sim G\delta^3(\underset{\sim}{x})Q_\omega \tag{8}$$

that will be responsible for very small energy shifts of the order of $G(mZ\alpha)^3 Z$. While it is in fact possible to measure energy splittings

to the desired accuracy,(in hydrogen, the effect in the ground state hyperfine structure is predicted to be 10^4 times larger than the experimental uncertainty (Jar, 74)) it would be impossible to distinguish the weak interaction shifts from nuclear and quantum electrodynamic effects.

The parity-violating potential given in Eqs. (6) and (7) might give rise to physically observable effects. The potential mixes states of opposite parity, and transitions forbidden by electromagnetic parity selection rules are allowed to order G^2. Similar effects in nuclear transitions have already been studied (Gar, 73), (Fis, 73), (Mck, 70). However, if transitions can proceed by <u>both</u> the normal electromagnetic channels and by the parity mixing of the weak Hamiltonian, interference effects, linear in G, will appear. For example, matrix amplitudes that are normally only magnetic dipole will contain a small electric dipole admixture, and the interference of the two amplitudes will give circular polarization effects that are proportional to $E1_{p.V.}/M1$.

The present experiments in search of parity violation due to neutral currents are either optical rotation experiments or absorption experiments, but they all exploit the possibility of interference effects enhanced in heavy atoms. The optical rotation experiments look for a very small rotation in Bismuth vapor due to an interference between an allowed M1 transition and the parity violating E1 transition. This interference produces a difference in the refractive index for right and left circularly polarized light and leads to a rotation of the plane of polarization of linearly polarized light. The rotation

is given by

$$\phi = \frac{4\pi(n-1)L}{\lambda} \quad \frac{-iE1_{p.V.}}{M1} \tag{9}$$

where n is the index of refraction, L is the path length, and λ is the wavelenth of the transition. M1 is much larger than $E1_{p.V.}$ and is a real quantity, while $E1_{p.V.}$ is imaginary given a conventional choice of phase. The quantity ϕ should follow a dispersion curve about the absorption line, and has been calculated by Khriplovich (Khr, 74), and Henley and Wilets (Hen, 76) to be a few times 10^{-7} radians per absorption length based on the simple Weinberg model. Both Fortson (For, 76) and Sandars (San, 76) have already reported upper limits of 10^{-7} rad./abs. length. However, due to the extremely small rotation, the experiment is very delicate and subject to serious systematic effects.

The alternative class of experiments uses highly forbidden M1 transitions to further enhance the parity violating effects, which scale as E1/M1. In these experiments, a difference in the absorption between left and right circularly polarized light is expected to be 10^{-4} to a few times 10^{-3} of the total absorption, and has been calculated by M.A. and C.C. Bouchiat (Bou; 74b, 75a) and Khriplovich (Khr, 76) in the case of cesium, and by Neuffer (Neu, 76) for thallium. Although the parity violating effects are relatively large, the small M1 amplitudes present many experimental problems, and it is a formidable task just to observe these transitions. This thesis represents the first step in our group's effort to detect parity violation in atoms due to neutral currents.

For the sake of completeness, brief mention should be made of other tests for parity violating transitions. Muonic atoms are being considered since the muon wave function at the nucleus is approximately two orders of magnitude larger than the corresponding electron wave function. A number of calculations have been made (Fei, 74), (Mos, 74), (Ber, 74) and circular polarizations as large as 10% are estimated for muonic Li and Be. Heavy helium-like ions are also being examined theoretically (Gor; 74, 75) and may soon be in the realm of experimental possibility. Finally, scattering experiments with polarized electrons are now in the planning stages (Hug, 76), (Ott, 76) and could yield results in the next few years.

B. Status of Parity Violation in Atomic Transitions

Measurements of static electric dipole moments in elementary particles, atoms, and molecules have already placed stringent limits on any interaction that violates both parity and time reflection. For more details, we refer the reader to reviews given by Sandars (San, 75) and Commins (Com, 71). Following the reasoning of Yang and Lee in their paper suggesting the possibility of parity violation in β - decay (Lee, 56), we can estimate the magnitude of the dipole moment d as

$$d \sim eF \times (\text{dimension of system}) \qquad (10)$$

where F is the degree of mixing of states of opposite parity. The experiments on heavy atoms by Sandars, et al. (Car, 68), (Pla, 70), (Har, 69), (Gou, 70) have placed a lower limit of $EDM_{electron} \leq 10^{-24}$ e-cm, which gives a value for $F \leq 10^{-15}$. Ramsey (Ram. 76) has recently

reported a comparable upper limit on the electric dipole moment of the neutron. Although the Weinberg model of neutral currents are P and C instead of P and T violating, the extremely small upper limits on the electric dipole moments can be reinterpreted to yield information on the nature of the weak interaction coupling. We describe the parity violating neutral current interactions between electrons and nucleons as

$$\mathcal{H} = \sum_{\substack{K=V,A,S,\\ P,T}} iC_K G(\bar{\psi}_n \Gamma_K \psi_n)(\bar{\psi}_e \Gamma_K \gamma_5 \psi_e) \tag{12}$$

where K spans the usual set of vector, axial vector, scalar, pseudoscalar and tensor combination of Dirac matrices. The first two terms are the familiar V,A interactions, (cf Eq. 4) while the final three terms violate both parity and time reversal invariance. C. Bouchiat, (Bou, 75c) and Hinds, Loving, and Sandars (Hin, 76) have concluded that the dipole moment measurements require the coupling constants for any scalar-pseudoscalar or tensor-pseudotensor interaction between electrons and nucleons to be at least three orders of magnitude less than the Fermi constant.

The limits on parity violating interactions that may be time-reversal invariant are not as stringent. Previous work on forbidden transitions in O_2,[30] Pb,[31] and Tm[32] has been reviewed by the Bouchiats (Bou, 74b). In fact, the current work being done in Paris, Oxford, Seattle, and Berkeley represents the best test of parity violation in atomic electromagnetic transitions by several orders of magnitude.

C. Outline of the Experiment

We now outline the experiment to measure the forbidden M1 transition amplitude in thallium. The lowest lying energy levels are indicated schematically in Fig. 2. In going from the $6^2P_{1/2}$ to $7^2P_{1/2}$ states, the only possible single photon transition for an unperturbed atom is an M1 transition, but since the magnetic dipole operator is given by $\underset{\sim}{\mu} = \frac{eh}{2mc}(\underset{\sim}{L}+2\underset{\sim}{S})$, the orthogonality of the non-relativistic radial wave functions gives a zero M1 matrix element. Only by including relativistic effects and hyperfine mixing, or configuration mixing does the M1 rate become non-zero.

A tunable laser is used to excite the Tl atoms to the $7^2P_{1/2}$ state via 292.7 nm light. The atoms then cascade first to the $7^2S_{1/2}$ state, and then go to either the $6^2P_{3/2}$ state or back to the ground state. Although the branching rates for the latter transitions are approximately equal, the 377.6 nm radiation to the ground state is resonantly trapped at our typical operating densities and converted into 535 nm light.

A large non-resonant background prevents us from scanning the frequency of our laser around 293 nm to search for an increase in the amount of 535 nm light detected by the phototubes on resonance. Following a suggestion by Bouchiat and Bouchiat (Bou, 75a), we measure the M1 amplitude through its interference with an E1 rate induced by a static electric field that mixes the P-states with neighboring $S_{1/2}$ and $D_{3/2}$ states. The interference between the M1 and E1 amplitudes results in an atomic polarization of the $7^2P_{1/2}$ state along a direction

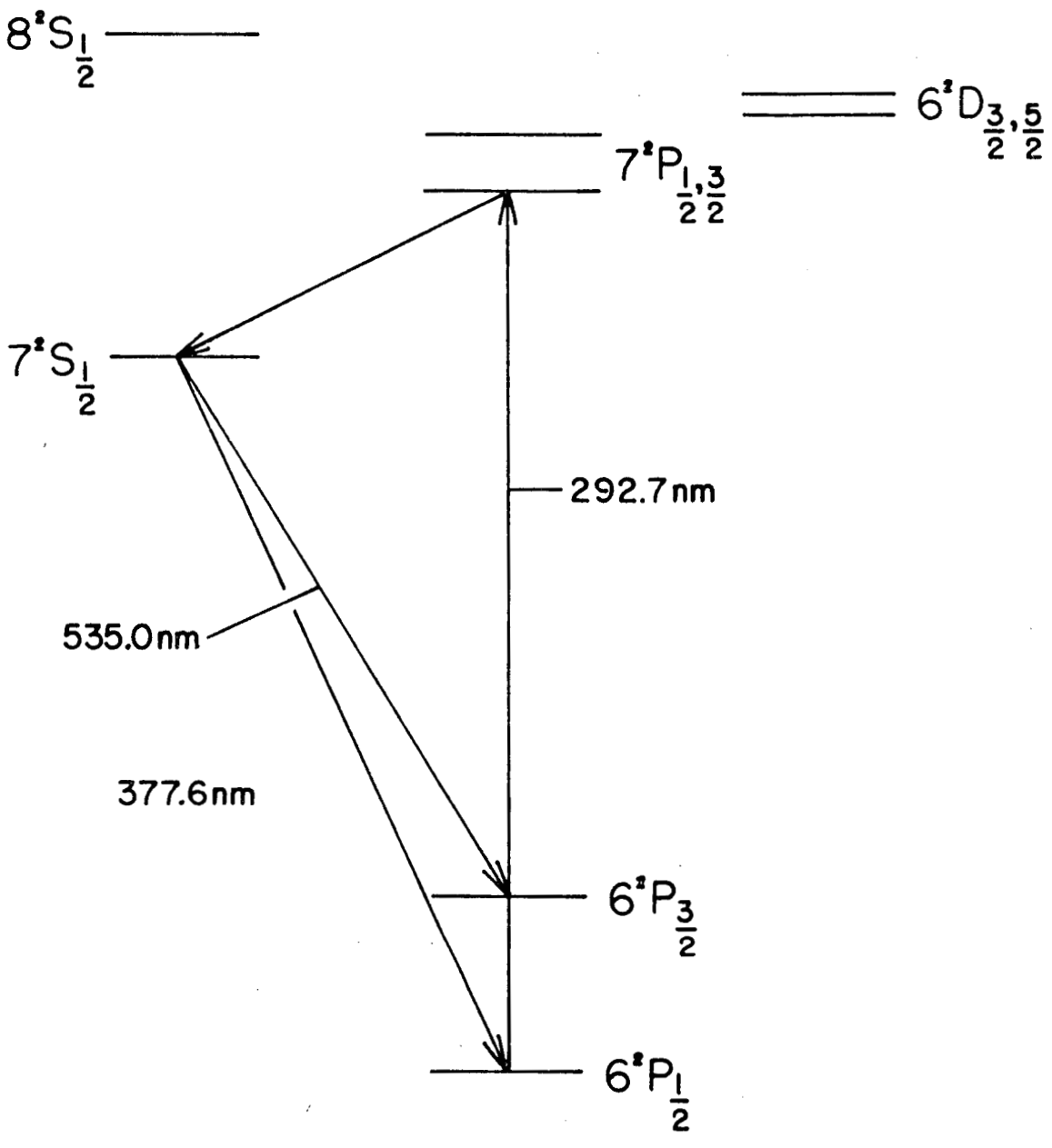

XBL 768-10237

Fig. 2. Energy level scheme for the lowest lying states of thallium.

perpendicular to both the static field and the direction of propagation of the incident light. The atomic polarization is measured by the subsequent emission of circularly polarized light. (see Fig. 3). If the atomic polarization is oriented along the positive z-axis, the radiation emitted in that direction will be predominately left-circularly-polarized, while radiation emitted along the negative z-axis will be right circularly polarized. When the electric field changes sign, the atomic polarization also reverses and the interference is seen as a difference in the counting rates for positive and negative electric fields. Two detectors are used to provide an added degree of symmetry: since both phototubes can detect only left-circularly-polarized light, when one tube counts higher for an equivalent amount of unpolarized photons the other counts lower and the polarization can also be seen as a difference in the absolute counting rates of both detectors. This technique of taking "differences of differences" has proved to be very powerful and makes it possible to avoid a great deal of instumental asymmetry. For example, the effects of fluctuations in the thallium density or in the incident power of laser light are cancelled.

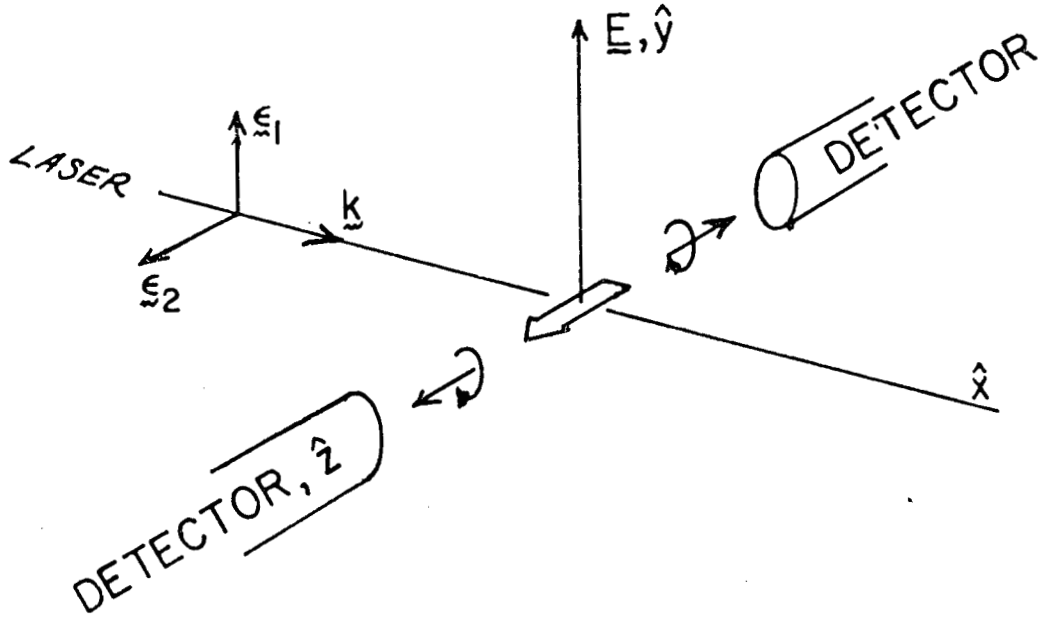

XBL 768-10240

Fig. 3. The incident light has linear polarization $\underset{\sim}{\varepsilon}_1$ or $\underset{\sim}{\varepsilon}_2$, and wave vector $\underset{\sim}{K}$. The electric field is along the $\hat{y}$-axis and the final-state polarization is directed along the $\hat{z}$-axis. Both detectors have left-circular polarizers in front of the photomultiplier tubes.

II. THEORY

A. Outline of the M1 Calculation

The single photon magnetic dipole transition (M1) follows the selection rules $\Delta J = 0, \pm 1$, no parity change. However, the usual form of the magnetic dipole operator

$$\underline{\mu} = \frac{e\hbar}{2mc} (\underline{\ell} + \underline{s}) \tag{1}$$

vanishes when taken between two states of different principle quantum numbers, in the non-relativistic approximation, and a more detailed calculation is necessary. Measurements of forbidden magnetic dipole transitions in normal atoms are limited to the $2^3S_1 - 1^1S_0$ transition in helium by Woodworth and Moos (Moos, 73) and the $6^2S_{1/2} - 7^2S_{1/2}$ transition in cesium by Bouchiat and Pottier (Bou, 76a). Beam-foil techniques, first used by Schmieder and Marrus (Sch, 70), have extended the measurements of "forbidden" magnetic dipole transition rates in hydrogen and helium-like heavy ions to a range of more than 12 orders of magnitude (Sel, 76).

1. Relativistic Corrections

There are many calculations of hydrogen and helium-like forbidden M1 decays (Fei, 71), (Bei, 71), (Dra, 71, 72), (Fen, 72), (Joh, 74), (Sch, 70); and recently, estimates have been made for the $6^2S_{1/2} - 7^2S_{1/2}$ transition in cesium by Bouchiat and Bouchiat (Bou, 75b, 76a) and Khriplovich (Khr, 76). A more detailed calculation using Dirac wave

functions for thallium and cesium generated numerically from a modified Tietz potential has been carried out by Neuffer (Neu, 76). The calculation is done using the fully relativistic notation of Berestetskii, Lifshitz, and Pitaevskii (Ber, 71) and it would be inappropriate to outline the calculation in this work. Instead, a more intuitive approach in calculating the forbidden M1 matrix element will be taken, in which first order relativistic corrections to the Pauli approximation are used. This treatment is taken from the work of Schwartz. (Sch, 70)

The general procedure begins with the Dirac equation for an electron in an electromagnetic field, ($\hbar$=c=1)

$$\mathcal{H} = \underset{\sim}{\alpha}\cdot(\underset{\sim}{p}-e\underset{\sim}{A}) + \beta m + e\phi \tag{2}$$

and application of the Foldy-Wouthoysen transformation is used to decouple the Dirac equation into two-component equations; one reducing to the Schrodinger-Pauli description in the non-relativistic limit, and the other describing the negative energy states. The transformation yields the hamiltonian

$$\mathcal{H} = m + \mathcal{H}_0 + \mathcal{H}'$$

$$\mathcal{H}_0 = \left(\frac{\underset{\sim}{p}-e\underset{\sim}{A}}{2m}\right)^2 - \frac{e}{2m}\,\underset{\sim}{\sigma}\cdot\underset{\sim}{B} + e\phi$$

$$\mathcal{H}' = \frac{1}{8m^3}\left[(\underset{\sim}{p}-e\underset{\sim}{A})^2 - e\underset{\sim}{\sigma}\cdot\underset{\sim}{B}\right]^2 - \frac{ie}{8m^2}\,\underset{\sim}{\sigma}\cdot(\underset{\sim}{\nabla}\times\underset{\sim}{E})$$

$$- \frac{e}{4m^2}\,\underset{\sim}{\sigma}\cdot\underset{\sim}{E}\times(\underset{\sim}{p}-e\underset{\sim}{A}) - \frac{e}{8m^2}\,(\underset{\sim}{\nabla}\cdot\underset{\sim}{E}) \tag{3}$$

Except for the additional terms in $\underset{\sim}{A}$, $\underset{\sim}{B}$ in $\mathcal{H}'$, the Hamiltonian is identical to the standard textbook formula. (Bjo, 64) Indeed, the

terms involving the relativistic mass increase, the electrostatic and magnetic dipole energies, the spin-orbit interaction and the Darwin terms can all be easily identified. Keeping terms linear in $\underset{\sim}{A}$ and $\underset{\sim}{B}$, we get

$$\mathcal{H} = T_1 + T_2 ,$$

$$T_1 = \frac{-e}{2m} [\underset{\sim}{p}\cdot\underset{\sim}{A} + \underset{\sim}{A}\cdot\underset{\sim}{p} + \underset{\sim}{\sigma}\cdot\underset{\sim}{B}],$$

$$T_2 = -\frac{1}{4m^2}(p^2T_1 + T_1p^2) - \frac{e\omega}{8m^2}\underset{\sim}{\sigma}\cdot\underset{\sim}{B} + \frac{ei\omega}{4m^2}\underset{\sim}{\sigma}\cdot\underset{\sim}{A}\times\underset{\sim}{p}$$

$$- \frac{e^2}{4m^2}\underset{\sim}{\sigma}\cdot(\underset{\sim}{\nabla}\phi)\times\underset{\sim}{A} + \frac{ei\omega}{8m^2}(\underset{\sim}{\nabla}\cdot\underset{\sim}{A}) \qquad (4)$$

where

$$\dot{\underset{\sim}{A}} = i\omega\underset{\sim}{A} . \qquad (5)$$

Now, set $A = \underset{\sim}{\varepsilon}e^{-i\underset{\sim}{k}\cdot\underset{\sim}{r}}$ with $\underset{\sim}{\varepsilon}\cdot\underset{\sim}{k} = 0$ and perform the standard multipole expansion in order to pick out the magnetic dipole part,

$$\underset{\sim}{A}(M1) = \frac{i}{2}(\underset{\sim}{\varepsilon}\times\underset{\sim}{k})\times\underset{\sim}{r}\,(1 - \frac{1}{10}k^2r^2 + \ldots) . \qquad (6)$$

We then get

$$\mathcal{H} = -i(\underset{\sim}{\varepsilon}\times\underset{\sim}{k})\cdot\underset{\sim}{\mu} ,$$

where the magnetic dipole moment operator is

$$\underset{\sim}{\mu} = \frac{e}{2m}[\underset{\sim}{\ell}(1 - \frac{1}{10}k^2r^2) + \underset{\sim}{\sigma}(1 - \frac{1}{5}k^2r^2) + \frac{1}{10}k^2\underset{\sim}{r}(\underset{\sim}{\sigma}\cdot\underset{\sim}{r})$$

$$- \frac{p^2}{2m^2}(\underset{\sim}{\ell}+\underset{\sim}{\sigma}) + \frac{\omega}{4m}\underset{\sim}{\sigma} - \frac{i\omega}{4m}\underset{\sim}{r}\times(\underset{\sim}{p}\times\underset{\sim}{\sigma}) - \frac{e}{4m}\underset{\sim}{r}\times(\underset{\sim}{\nabla}\phi\times\underset{\sim}{\sigma})] \qquad (7)$$

The term $\frac{\omega}{4m}\,\underset{\sim}{\sigma}$ can be dropped since it is only a multiple of the non-relativistic term, and will give no contributions when sandwiched between "non-relativistic" wave functions. (Note that there are two kinds of corrections to the M1 matrix element in the Pauli approximation: One is the relativistic correction to the magnetic dipole operator extracted via the Foldy-Wouthuysen transformation, and is of order $Z^2\alpha^2$. The other is the correction to the wavefunctions due to relativistic terms in the atomic Hamiltonian and is of order $Z^4\alpha^4$.) The terms from the finite wavelength (k^2r^2) of the photon (the so-called "retardation effects" due to the phase difference between the waves emitted at different points of the atomic volume) have been kept only in the T_1 part. The remaining term with ω can be reduced by the following commutator trick: (Sch, 70)

$$\omega = E_i - E_f$$

$$\omega\langle f|\underset{\sim}{r}\times(\underset{\sim}{p}\times\underset{\sim}{\sigma})|i\rangle = \langle f|[\underset{\sim}{r}\times(\underset{\sim}{p}\times\underset{\sim}{\sigma}),\ H_o]|i\rangle$$

$$= \langle f|-ie\underset{\sim}{r}\times(\underset{\sim}{\nabla}\phi\times\underset{\sim}{\sigma}) + \frac{i}{m}\,\underset{\sim}{p}\times(\underset{\sim}{p}\times\underset{\sim}{\sigma})|i\rangle \qquad (8)$$

Finally, we get

$$\underset{\sim}{\mu} = \frac{e}{2m}\Big[\underset{\sim}{\ell}\left(1 - \frac{1}{10}\,k^2r^2\right) + \underset{\sim}{\sigma}\left(1 - \frac{1}{5}\,k^2r^2\right) + \frac{1}{10}\,k^2\underset{\sim}{r}(\underset{\sim}{\sigma}\cdot\underset{\sim}{r})$$

$$- \frac{p^2}{2m^2}\,(\underset{\sim}{\ell}+\underset{\sim}{\sigma}) + \frac{1}{4m^2}\,\underset{\sim}{p}\times(\underset{\sim}{p}\times\underset{\sim}{\sigma}) - \frac{e}{2m}\,\underset{\sim}{r}\times(\underset{\sim}{\nabla}\phi\times\underset{\sim}{\sigma})\Big]\ . \qquad (9)$$

From the form of $\underset{\sim}{\mu}$ in the last equation, we can see how relativistic corrections have introduced operator terms that affect the radial

portion of the M1 matrix element. Drake (Dra, 71) has shown that a relativistic treatment using the formalism found in Berestetskii, et al. (Ber, 71) (and similar to the pioneering work of Breit and Teller, (Bre, 40) who unfortunately neglected to include the retardation terms) yields the same numerical result as the Pauli approximation for hydrogenic wave functions.

The angular integrals can be written as averages over the spatial variables p and r. Typical terms reduce as follows

$$\frac{1}{4\pi} \int d\Omega_p \langle f|\underset{\sim}{p}\times(\underset{\sim}{p}\times\underset{\sim}{r})|i\rangle$$

$$= \frac{1}{4\pi} \int d\Omega_p \langle f|(\underset{\sim}{p}\cdot\underset{\sim}{\sigma})\underset{\sim}{p} - (\underset{\sim}{p}\cdot\underset{\sim}{p})\underset{\sim}{\sigma}|i\rangle$$

$$= \langle f|\frac{1}{3} p^2\underset{\sim}{\sigma} - p^2\underset{\sim}{\sigma}|i\rangle \qquad (10)$$

where

$$\frac{1}{4\pi} \int d\Omega_p (\underset{\sim}{p}\cdot\underset{\sim}{\sigma})p_j = \frac{1}{3}\sigma_j p^2 \ .$$

Thus,

$$\underset{\sim}{\mu} = \frac{e}{2m} [\underset{\sim}{\ell}(1 - \frac{1}{10} k^2r^2) - \frac{p^2}{2m}\underset{\sim}{\ell}$$

$$+ \underset{\sim}{\sigma}(1 - \frac{1}{6} k^2r^2 - \frac{2p^2}{3m} + \frac{e}{3m} (\underset{\sim}{r}\cdot\underset{\sim}{\nabla}\phi))] . \qquad (11)$$

When $\underset{\sim}{\ell} = 0$, Eq. (11) reduces to the formula used by Bouchiat and Bouchiat (Bou, 75b) to estimate the $6^2S_{1/2} - 7^2S_{1/2}$ M1 matrix element of cesium. The matrix elements $\langle 7^2P_{1/2}\ F,m_F|\underset{\sim}{\mu}|6^2P_{1/2}F,m_o\rangle$ of thallium are calculated by writing the initial and final state as the product of a radial wave function and angular momentum part constructed from

wavefunctions of nuclear spin, electron spin, and orbital angular momentum, using the usual vector addition of angular momenta. The parts of the matrix elements involving $\underline{\ell}$ and $\underline{s}$ are easily evaluated, and we are left with radial integrals of the form

$$\int f^{*}_{7^2P_{1/2}} k^2 r^2 f_{6^2P_{1/2}} r^2 dr, \int f^{*}_{7^2P_{1/2}} p^2 f_{6^2P_{1/2}} f^2 dr, \text{ etc.} \qquad (12)$$

The radial wavefunctions are generated by Neuffer (Neu, 76) by assuming one electron orbits in a spherically symmetric Tietz potential. The parameters of the potential are adjusted to produce wavefunctions that are consistent with the known energy level structure of thallium. As a check, the wave functions are then used to calculate oscillator strengths, fine structure and hyperfine structure splittings and compared with experimental values. From these checks, we believe the radial integrals are accurate to at least 10%.

Once we have the wavefunctions of thallium, a numerical integration can be performed to evaluate Eq. (12) and the complete matrix elements. Neuffer finds that the relativistic contribution to the $6^2P_{1/2} - 7^2P_{1/2}$ M1 matrix element of thallium is

$$\langle \mu \rangle = -1.81\times10^{-5} \frac{|e|\hbar}{2mc} \qquad (13)$$

2. Hyperfine Mixing

There are other effects that could possibly effect the M1 rate, notably hyperfine mixing and configuration mixing. In the case of hyperfine mixing, the perturbing Hamiltonian is given by

$$\mathcal{H}' = \text{const.} \times \underline{I}\cdot\underline{J} \qquad (14)$$

where $\underset{\sim}{I}$ is the spin of the nucleus and $\underset{\sim}{J}$ is the total angular momentum of the electrons. The perturbed wavefunctions can be written approximately as

$$|\overline{7P_{1/2}F',m_F}\rangle = |7P_{1/2}F',m_F\rangle + \frac{|6F',m_F\rangle \langle 6F',m_F|\mathcal{H}'|7F',m_F\rangle}{E_{7P} - E_{6P}} ,$$

and

$$|\overline{6P_{1/2}F,m_F}\rangle = |6P_{1/2}F,m_F\rangle + \frac{|7F,m_F\rangle \langle 7F,m_F|\mathcal{H}'|6F,m_F\rangle}{E_{6P} - E_{7P}} . \qquad (15)$$

The magnetic dipole transition amplitude can then be written as

$$\begin{aligned}
\langle \underset{\sim}{\mu} \rangle &= \langle \overline{7P_{1/2}F',m_F}|\underset{\sim}{\mu}|\overline{6P_{1/2}F,m_F}\rangle \\
&= \langle 7P_{1/2}F',m_F|\underset{\sim}{\mu}|6P_{1/2}F,m_F\rangle \\
&+ \frac{1}{E_{7P}-E_{6P}} \{\langle 7F',m_F|\mathcal{H}'|6F',m_F\rangle \langle 6F',m_F|\underset{\sim}{\mu}|6F,m_F\rangle \\
&- \langle 7F',m_F|\underset{\sim}{\mu}|7F,m_F\rangle \langle 7F,m_F|\mathcal{H}'|6F,m_F\rangle \} \qquad (16)
\end{aligned}$$

The first term in Eq. (16) is our original M1 matrix element, while the second term consists of a product of a g-factor for either the $6^2P_{1/2}$ or $7^2P_{1/2}$ state and the off-diagonal terms of the hyperfine splitting matrix elements. From $\underset{\sim}{F} = \underset{\sim}{I} + \underset{\sim}{J}$, we can write

$$\begin{aligned}
\underset{\sim}{I}\cdot\underset{\sim}{J} &= \frac{1}{2}\,[F(F+1) - I(I+1) - J(J+1)] \\
&= \frac{1}{2}\,[F(F+1) - 3/2]
\end{aligned} \qquad (17)$$

Also, in the non-relativistic approximation

$$g = \langle 6F', m_F | \underset{\sim}{\mu} | 6F, m_F \rangle = \langle 7F', m_F | \underset{\sim}{\mu} | 7F, m_F \rangle \ , \tag{18}$$

so the second term of Eq. (16) can be written as

$$\frac{g}{E_{7P}-E_{6P}} \{ \langle 7F', m_F' | \text{const.} \times \underset{\sim}{I} \cdot \underset{\sim}{J} | 6F' m_F' \rangle - \langle 7F, m_F | \text{const.} \times I \cdot J | 6F, m_F \rangle \} \ . \tag{19}$$

From the operator $\underset{\sim}{I} \cdot \underset{\sim}{J}$ given in Eq. (17), we immediately can write the selection rules for the non-zero hyperfine mixing contribution as $\Delta F \neq 0$ and $\Delta m_F = 0$.

Finally, it can be shown that

$$\langle 7P | \mathcal{H}' | 6P \rangle \approx \sqrt{\langle 7P | \mathcal{H}' | 7P \rangle \langle 6P | \mathcal{H}' | 6P \rangle} \ , \tag{20}$$

so that the scale of the hyperfine correction is of the order

$$\frac{\text{hyperfine splitting}}{E_{7P} - E_{6P}} \mu_B \approx \frac{10^9 - 10^{10} \text{Hz}}{10^{15} \text{Hz}} \mu_B \approx (10^{-6} - 10^{-5}) \mu_B \tag{21}$$

A detailed calculation by Neuffer shows that the hyperfine correction gives a 16% change for $\Delta F = 1$ transitions in thallium and no change for $\Delta F = 0$ transitions (Neu, 76)

$$\langle \mu \rangle_{\text{hyperfine}} = \begin{cases} -2.5 \times 10^{-6} \ |\mu_B| & \text{for} \quad F = 0 \rightarrow 1 \\ +2.5 \times 10^{-6} \ |\mu_B| & \text{for} \quad F = 1 \rightarrow 0 \end{cases}$$

2. Configuration Mixing

The perturbation of electrostatic interactions $\sum_{i \neq j} \frac{e^2}{r_{ij}}$ were first considered in relation to atomic g-factors. The experiments

measuring nuclear magnetic moments done by Millman and Kusch (Mil,41) had assumed that the gound state alkali atoms had a $g_J = 2$ to the precision of their experiments, which was better than one part in 3000. (The value of the gyromagnetic ratio follows directly from a single s-electron moving in a central field of the nucleus and core electrons and the non-QED g-factor of the electron). At that time, Margenau (Mar, 40) showed that relativistic corrections could only cause

$$\frac{\Delta g}{g} = \frac{g_{atom} - g_{electron}}{g_{atom}} \approx 10^{-5} \tag{22}$$

in cesium. Phillips (Phi, 41) examined the electrostatic interaction that would give configurations with excited core states, but since $\frac{e^2}{r_{ij}}$ mixes only those states having the same orbital angular momentum and spin, the higher configurations could only be states differing in principle quantum number. Hence, the usual orthogonality of these states would demand that the g-factor would not be affected. After the anomalous magnetic magnetic moment of the electron was recognized (Kus, 47, 48a, 48b), (Sch, 48), Phillips reexamined perturbations of atomic g-values due to configuration mixing by extending the perturbation calculation to sufficiently high orders until $\frac{\Delta g}{g} \neq 0$ (Phi, 52). In her second attempt, Phillips found that the combined perturbation of

$$H' = \sum_{i \neq j} \frac{e^2}{r_{ij}}$$

and

$$H' = \sum_i \frac{1}{2m^2} \frac{1}{r} \frac{d\phi}{dr} \underset{\sim}{\ell}_i \cdot \underset{\sim}{s}_i \tag{20}$$

to fourth order was necessary. The calculation has been performed in detail by Neuffer (Neu, 76) and only the barest outline will be presented here.

The unperturbed ground state of thallium has the configuration

$$|\psi_o\rangle = 6s^2(^1S_0)6p\ ^2P_{1/2}\ , \tag{21}$$

where the two 6s electrons may be thought to form a $^1S_0$ state, which then combines with the 6p state to form the $^2P_{1/2}$ state. The interaction e^2/r_{ij} gives non-zero matrix elements of the form

$$\langle 6s^2 6p|\frac{e^2}{r_{ij}}|6sns6p\rangle\ ,$$
$$\langle 6s^2 6p|\frac{e^2}{r_{ij}}|6sns7p\rangle\ ,$$
$$\langle 5d^{10}6s^2 6p|\frac{e^2}{r_{ij}}|5d^9 6s^2 6pnd\rangle\ ,\ \text{etc.} \tag{22}$$

Let us consider only configurations that involve higher s-states. For example,

$$|\tilde{\psi}_i\rangle = |\psi_o\rangle + a|\psi_1\rangle$$

where

$$|\psi_1\rangle = 6s7s(^3S_1)6p\ ^2P_{1/2}\ , \tag{23}$$

and a is the usual first order perturbation coefficient. Recall that e^2/r_{ij} commutes with both $\underset{\sim}{J}$ and $\underset{\sim}{S}$ so the total state must still be $^2P_{1/2}$, and $\langle\tilde{\psi}_f|\mu|\tilde{\psi}_i\rangle$ will still be zero. We can now include the $\underset{\sim}{L}\cdot\underset{\sim}{S}$ perturbation which allows a spin change, and hence a total state $^4P_{1/2}$. Phillips shows that only second-order wave functions are needed for the fourth order calculation. As far as the magnetic dipole transition

is concerned, the general expression

$$|\tilde{\psi}\rangle = |\psi_0\rangle + \sum_i \frac{|\psi_i\rangle\langle\psi_i|\frac{e}{r_{ij}}|\psi_0\rangle}{E_0 - E_i} + \sum_{i,j} \frac{|\psi_k\rangle\langle\psi_k|\xi\underset{\sim}{L}\cdot\underset{\sim}{S}|\psi_i\rangle\langle\psi_i|\frac{e}{r_{ij}}|\psi_0\rangle}{(E_0-E_1)(E_0-E_k)} \qquad (24)$$

reduces to wavefunctions of the form

$$|\tilde{6p}\rangle = |6s^2 6p\ ^2P_{1/2}\rangle + a_1|6s7s6p\ ^4P_{1/2}\rangle + a_2|6s7s7p\ ^4P_{1/2}\rangle + a_3|6s^2 7p\ ^2P_{1/2}\rangle ,$$

$$|\tilde{7p}\rangle = |6s^2 7p\ ^2P_{1/2}\rangle + b_1|6s7s6p\ ^4P_{1/2}\rangle + b_2|6s7s7p\ ^4P_{1/2}\rangle + b_3|6s^2 6p\ ^2P_{1/2}\rangle .$$

Orthogonality of the wave functions $|\tilde{6p}\rangle$ and $|\tilde{7p}\rangle$ gives the relation

$$a_1 b_1 + a_2 b_2 + a_3 + b_3 = 0 .$$

Hence,

$$\begin{aligned}\langle\tilde{7p}|\mu|\tilde{6p}\rangle &= a_1 b_1\langle{}^4P_{1/2}|\mu|{}^4P_{1/2}\rangle + a_2 b_2\langle{}^4P_{1/2}|\mu|{}^4P_{1/2}\rangle \\ &\quad + a_3\langle{}^2P_{1/2}|\mu|{}^2P_{1/2}\rangle + b_3\langle{}^2P_{1/2}|\mu|{}^2P_{1/2}\rangle \\ &= (a_1 b_1 + a_2 b_2)\,[g({}^4P_{1/2}) - g({}^2P_{1/2})] . \qquad (25)\end{aligned}$$

The single particle states are calculated separately by assuming that each electron orbits in a central potential. A several-electron wavefunction is then formed by combining the single electron functions in the proper antisymmetric state, and the a and b coefficients are then calculated by evaluating the integrals (Eq. 17) numerically. Neuffer

finds that the configuraton mixing is responsible for a 5% change in the M1 matrix element.

The configuration mixing calculation is uncertain. First of all, it is not a bona-fide many-particle calculation as in the Hartree-Fock type calculations, and while the central potential approximation is perfectly adequate for a single electron outside a closed shell, as in the case of the 6s electron in cesium or the 6p electron in thallium, it may not be as justifiable for the inner electrons. (One of the 6s electrons in thallium would hardly be expected to see a central potential due to the other 6s electron and the 6p electron.) Furthermore, the configurations involving excited d-states may play a significant role in the mixing and cannot be neglected a priori. In fact, Phillips (Phi, 52) surmised that the d-state contribution would be larger than that of the s-states, but their inclusion make the calculation extremely difficult. A summary of Neuffer's M1 calculations is given in Table I.

B. Interference Between the Magnetic Dipole Amplitude and the Electric Dipole Amplitude Induced by a Static Electric Field

As we have stated in the introduction, a large, non-resonant background (see section V for more details) prevents us from observing the M1 rate directly. Following a suggestion by Bouchiat and Bouchiat (Bou, 75a) we measure the M1 rate through its interference with an E1 rate induced by a static electric field, a technique also used by Bouchiat and Pottier (Bou, 75b, 76a) to measure the $6^2S_{1/2} - 7^2S_{1/2}$ transition is cesium. The calculation of the signal we expect from the M1-E1 interference will be outlined here, using straightforward but

Table I. Contribution to $6^2P_{1/2} - 7^2P_{1/2}$ M1 matrix element of Thallium.

Relativistic contribution

$$\langle M1 \rangle = -1.7\times10^{-5} \ |\mu_B|$$

Hyperfine mixing contribution

$$\langle M1 \rangle = -.25\times10^{-5} \ |\mu_B| \quad \text{for } F = 0 \rightarrow 1$$

$$= +.25\times10^{-5} \ |\mu_B| \quad \text{for } F = 1 \rightarrow 0$$

$$= 0 \quad \text{for } F = 0 \rightarrow 0 \text{ or } 1 \rightarrow 1$$

Configuration mixing contribution

$$\langle M1 \rangle = -0.1\times10^{-5} \ |\mu_B|$$

The parity violating E1 matrix element for the $6^2P_{1/2} - 7^2P_{1/2}$ transition is also calculated by Neuffer:

$$E1_{P.V.} = i1.9\times10^{-10} \ Q_W\mu_B$$

$$|\text{Asymmetry}| = \frac{2|E1_{P.V.}|}{|M1|} = 2.1 \ 10^{-5} \ Q_W = 2.9\times10^{-3} \ .$$

Using

$$\sin^2\theta_\omega = .29$$

and

$$Q_W = -[(4\sin^2\theta_\omega - 1)Z + N] = 136$$

unsophisticated techniques. For, more elegant treatments in a general tensor notation, the reader is referred to the publications by Bouchiat and Bouchiat (Bou, 75b) and Neuffer (Neu, 76).

The Hamiltonian describing an M1 and E1 transition is given by

$$\mathcal{H}' = \underset{\sim}{d}\cdot\underset{\sim}{E} + \underset{\sim}{\mu}\cdot\underset{\sim}{B} \ . \tag{1}$$

Using the coordinate system shown in Fig. 3, photons directed along the $\hat{x}$-axis will have some polarization $\hat{\varepsilon}$ at an angle θ with respect to the y-axis,

$$\hat{\varepsilon} = \hat{y}\cos\theta + \hat{z}\sin\theta \ . \tag{2}$$

Since

$$\underset{\sim}{B}(\underset{\sim}{x},t) = \hat{x} \times \underset{\sim}{E}(\underset{\sim}{x},t) \ ,$$

the Hamiltonian can be written as

$$\mathcal{H}' = e\underset{\sim}{r}\cdot\underset{\sim}{\varepsilon} + \underset{\sim}{\mu}\cdot(\hat{x}\times\underset{\sim}{\varepsilon})$$

$$= e(y\cos\theta + z\sin\theta) + \mu_z$$

The magnetic dipole operator can be formally written as

$$\underset{\sim}{\mu} = \mu_0(\underset{\sim}{L}+2\underset{\sim}{S}) \ , \quad \mu_0 = -\frac{|e|\hbar}{2mc} \ . \tag{3}$$

We will use the spherical operators

$$d_+ = \frac{-(x+iy)}{\sqrt{2}} \ , \quad d_- = \frac{(x-iy)}{\sqrt{2}} \ . \tag{4}$$

Thus,

$$\mathcal{H}' = e[\frac{i}{\sqrt{2}}(d_+ + d_-)\cos\theta + z\sin\theta]$$

$$+ \mu_o[(L_z+2S_z)\cos\theta + \frac{i}{2}(L_+ + S_+)\sin\theta - \frac{i}{2}(L_- + 2S_-)\sin\theta] \ . \qquad (5)$$

Because of the perturbation of the static E-field in the y-direction, the initial and final states are

$$\overline{|6^2P_{1/2}F_0,m_0\rangle} = |6^2P_{1/2}F_0,m_0\rangle + \sum_{n,F',m'} \frac{|nF'm'\rangle\langle nF'm'|eEy|6P_{1/2}F_0m_0\rangle}{\Delta_6}$$

$$\overline{|7^2P_{1/2}F,m_F\rangle} = |7^2P_{1/2}F,m_F\rangle + \sum_{n,F',m'} \frac{|nF'm'\rangle\langle nF'm'|eEy|7P_{1/2}Fm_F\rangle}{\Delta_7} \qquad (6)$$

where

$$\Delta_6 = E_{6P_{1/2}} - E_n \quad \text{and} \quad \Delta_7 = E_{7P_{1/2}} - E_n \ ,$$

and the sum is over all S and $D_{3/2}$ states.

Our task is to evaluate the matrix elements

$$\alpha^{F,m_F}_{F_0,m_0} = \langle \overline{7^2P_{1/2}F,m_F}|\mathcal{H}'|\overline{6^2P_{1/2}F_0m_0}\rangle$$

The nuclear spin I of thallium is 1/2 and the two states of interest have an electronic angular momentum J = 1/2. The total state $|F,m_F\rangle$ is constructed out of the wave functions in $\underset{\sim}{L}$, $\underset{\sim}{S}$, and $\underset{\sim}{I}$ using the usual rules of vector addition of angular momentum. The M1 part of $\alpha^{F,m_F}_{F_0,m_0}$ is easily calculated and given in Table II.

Table II. M1 matrix elements $|F, m_F\rangle$

Initial State $6P_{1/2}$ \ Final $7P_{1/2}$ States	$\|0,0\rangle$	$\|1,1\rangle$	$\|1,0\rangle$	$\|1\text{-}1\rangle$
$\|0,0\rangle$	0	$-\mu_{eff}\frac{i}{\sqrt{2}}\sin\theta$	$\mu_{eff}\cos\theta$	$-\mu_{eff}\frac{i}{\sqrt{2}}\sin\theta$
$\|1,1\rangle$	$\mu_{eff}\frac{i}{\sqrt{2}}\sin\theta$	$\mu_{eff}\cos\theta$	$-\mu_{eff}\frac{i}{\sqrt{2}}\sin\theta$	0
$\|1,0\rangle$	$\mu_{eff}\cos\theta$	$\mu_{eff}\frac{i}{\sqrt{2}}\sin\theta$	0	$-\mu_{eff}\frac{i}{\sqrt{2}}\sin\theta$
$\|1,-1\rangle$	$\mu_{eff}\frac{i}{\sqrt{2}}\cos\theta$	0	$\mu_{eff}\frac{i}{\sqrt{2}}\sin\theta$	$-\mu_{eff}\cos\theta$

A similar table is constructed for the static field E1 amplitudes. Although such a table would be too lengthy to include here, a few comments are in order. First, simplifications result from the fact that d_+ and d_- are proportional to the spherical harmonics Y_{11} and Y_{1-1} and behave like raising and lowering operators for $\underset{\sim}{L}$ and hence $\underset{\sim}{F}$. The operators in α_{F_0,m_0}^{F,m_F} appear as combinations of $d_\pm$, $d_\mp$ which connect states of $\Delta m_F = 0$, and as combinations of $d_\pm$, z which combine states of $\Delta m_F = \pm 1$. (The static field E1 amplitude may be thought as a two-photon transition, where one of the photons has a very long wavelength. However, the analogy is not strictly true since $\Delta m_F = \pm 2$ transitions do not appear. The possible transitions are $|1,-1\rangle \rightarrow |1,1\rangle$ and $|1,+1\rangle \rightarrow |1,-1\rangle$, but the nuclear spins for the $|1,1\rangle$ and $|1,-1\rangle$ states are orthogonal.) Second, the angular integrals reduce to an integral of a product of three $Y_{\ell,m}$'s, and these integrals have been tabulated in standard books on angular momentum. (Ros, 57)

The general form of the M1-E1 matrix elements are of the form

$$\alpha_{F,m_0}^{F,m_F} = (\text{M1 PART}) + \text{const.} \times \Big[\sum_{ns} R_{7pns} R_{ns6p} \times (\text{energy denominator}) \Big]$$

$$\times \sum_{F',m'} \langle F,m_F|O|F'm'\rangle\langle F'm'|O|F_0m_0\rangle \qquad (7)$$

+ a similar term for the D-states,

where

$$R_{7PnS} = \int f_{7p}^{*} r f_{ns} r^2 dr \text{ and } O \text{ is the operator } d_\pm \text{ or } z. \qquad (8)$$

We define

$$D_6 = \sum_{nD} R_{7PnD} R_{nD6P} \frac{1}{E_{6p} - E_n}$$

$$D_7 = \sum_{nD} R_{7PnD} R_{nD6P} \frac{1}{E_{7P} - E_n}$$

$$S_6 = \sum_{nS} R_{7PnS} R_{nS6P} \frac{1}{E_{6P} - E_n}$$

$$S_7 = \sum_{nS} R_{7PnS} R_{nS6P} \frac{1}{E_{7P} - E_n} \qquad (9)$$

and the coefficients

$$\alpha(\theta=0) = \frac{e^2 E}{9} (S_6 + S_7 + 2D_6 + 2D_7)$$

$$\beta(\theta=\pi/2) = \frac{e^2 E}{9} (S_6 - S_7 + D_7 - D_6) \qquad (10)$$

We summarize the possible M1-E1 transitions for laser polarizations both parallel and perpendicular to the electric field in Table III, and indicate the selection rules in Figs. 4 and 5. The quantities α and β are calculated from the radials integrals supplied by Neuffer and the coefficients $S_{6,7}$ and $D_{6,7}$ are evaluated by both an explicit sum over the nearest neighboring S and D states and by a Green's function technique that includes all discrete and continuous S and D states. (Neu, 76) The energy denominators are taken from the values of energy levels of thallium listed in the NBS table compiled by C. Moore. (Mor, 52) The results are (in atomic units)

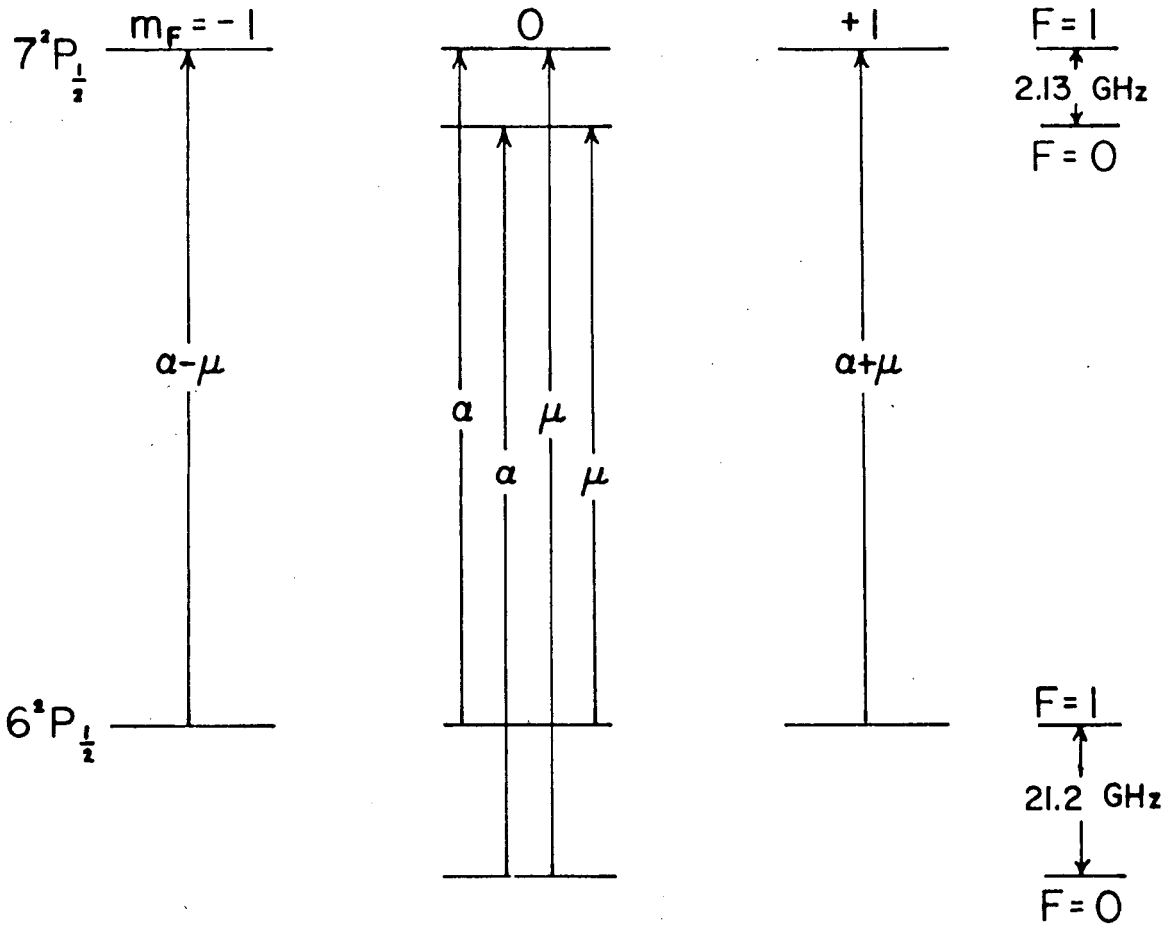

Fig. 4. Matrix elements for laser polarization $\hat{\epsilon}$ parallel to $\underset{\sim}{E}$.

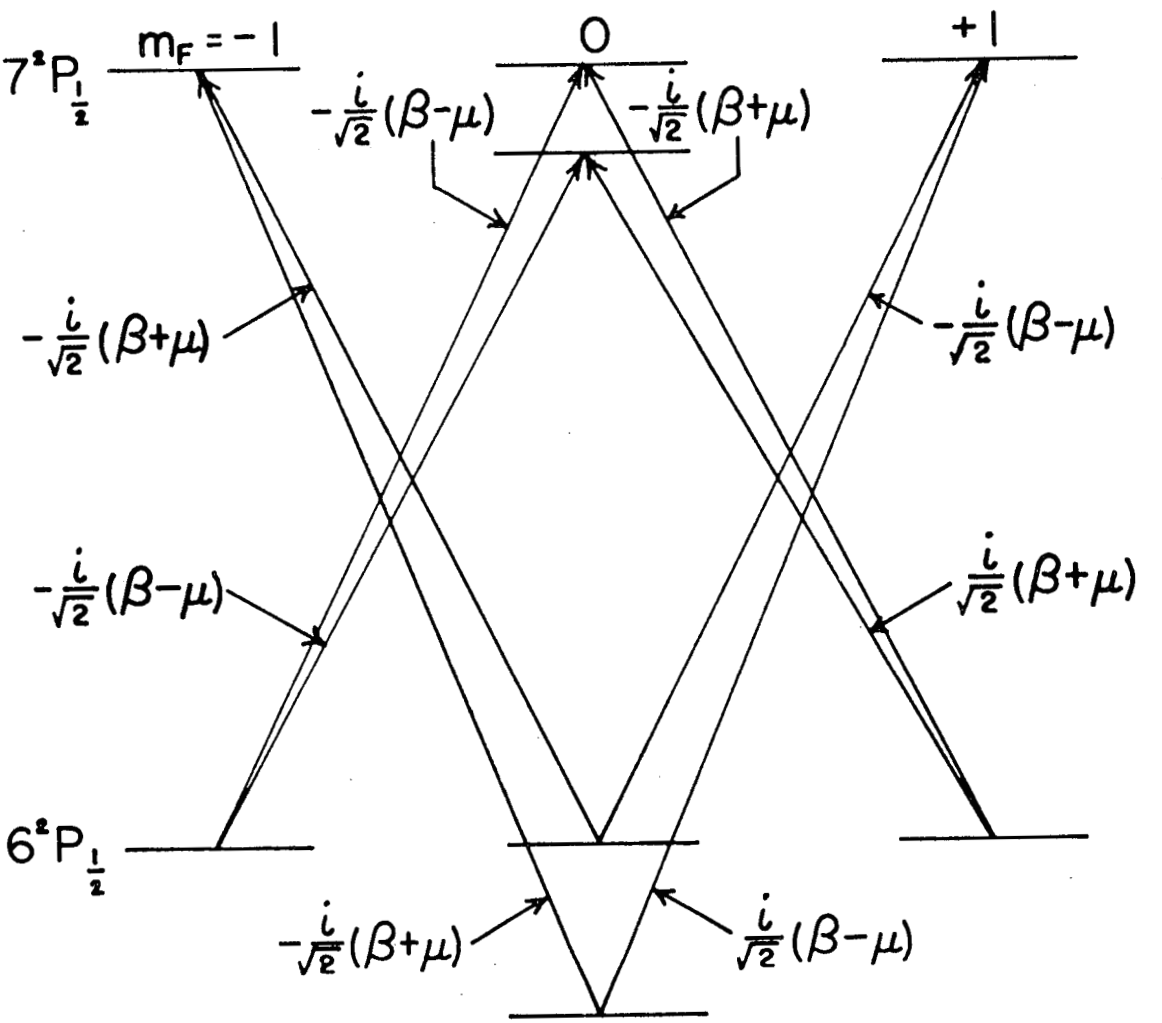

Fig. 5. Matrix elements for laser polarization $\hat{\epsilon}$ perpendicular to $\underset{\sim}{E}$.

Table III.

Incident Light Polarization	Transition $6^2P_{1/2} \rightarrow 7^2P_{1/2}$ $F_o \rightarrow F$	Theoretical Intensity	Calculated Relative Intensity Assuming E Large $\alpha/\beta_{theory} = .80$
$\hat{\varepsilon} \parallel \underset{\sim}{E}_o$	$1 \rightarrow 1$	$\frac{3}{4}\alpha^2 + \frac{1}{4}\mu^2$	3
	$0 \rightarrow 0$	$\alpha^2/4$	1
	$0 \rightarrow 1$	$\mu^2/4$	0
	$1 \rightarrow 0$	$\mu^2/4^2$	0
$\hat{\varepsilon} \perp \underset{\sim}{E}_o$	$1 \rightarrow 1$	$\frac{1}{2}\beta^2 + \frac{1}{2}\mu^2$	1.92
	$1 \rightarrow 0$	$\frac{1}{4}\beta^2 + \frac{1}{4}\mu^2$	
	$0 \rightarrow 0$	0	0
	$1 \rightarrow 0$	$\frac{1}{4}\beta^2 + \frac{1}{4}\mu^2$	.64

Table IV.

Incident Light Polarization	Transition $6^2P_{1/2} \rightarrow 7^2P_{1/2}$ $F \rightarrow F'$	Theor. $7^2P_{1/2}$ Polarization	Theor. $7^2P_{1/2}$ Polarization for large E_o, assuming $\beta/\alpha_{exp.} = .84$
$\hat{\varepsilon} \parallel E_o$	$1 \rightarrow 1$	$\frac{4m\alpha}{3\alpha^2+2m^2}$	$P_{\parallel} = \frac{4}{3}\frac{m}{\alpha}$
	$0 \rightarrow 0$	0	0
$\hat{\varepsilon} \perp E_o$	$1 \rightarrow 1$	$\frac{-m\beta}{\beta^2+m^2}$	Only partially resolved
	$1 \rightarrow 0$	0	
	$0 \rightarrow 1$	$\frac{-2m'\beta}{\beta^2+m^2}$	$P_{\perp} = \frac{-2m'}{\beta} \simeq -2.07\ P_{\parallel}$
		$m' = 1.15\ m$ due to ufs correction.	

$$\alpha = \frac{e^2 E_o}{9}\,(3469.2), \qquad \beta = \frac{e^2 E_o}{9}\,(2777.7)$$

$$\alpha/\beta = .80 \tag{11}$$

The atomic polarization of the final state $7^2P_{1/2}$, is defined to be

$$P = \frac{\sum_{m_F, m_0} m_F \left| \langle \overline{7^2P_{1/2}\ F, m_F | \mathcal{H}' | 6^2P_{1/2}\ F_0, m_0} \rangle \right|^2}{\sum_{m_F, m_0} \left| \langle \overline{7^2P_{1/2},\ F, m_F | \mathcal{H}' | 6^2P_{1/2}\ F, m_0} \rangle \right|^2} \tag{12}$$

where $\mathcal{H}'$ is the M1-E1 Hamiltonian given in Eq. (1) and the wave functions $|6^2P_{1/2},\ F_0 m_0\rangle$, $|7^2P_{1/2}\ F, m_F\rangle$ are given in Eq. (6). We average over the m_0 sublevels of the unpolarized $6^2P_{1/2}$ state. The relative populations of the m_F levels can be taken directly from Figs. 4 and 5, and the results are given in Table IV. The calculations predict that the $F = 0 \to 1$, $\hat{\varepsilon} \perp \underset{\sim}{E}$ atomic polarization should be slightly more than twice as large as the $F = 1 \to 1$, $\hat{\varepsilon} \parallel \underset{\sim}{E}$ polarization and of the opposite sign. Also, the $F = 0 \to 0$ transition clearly cannot yield any final state polarization since there is only one m_F valve.

III. EXPERIMENTAL METHOD

The experimental apparatus is shown schematically in Fig. 6, and photograph of the apparatus is given in Fig. 7. A flashlamp pumped dye laser (1) running at 10-15 pulses per second with energies of 5-10 millijoules per pulse in .5 μsec, and in a bandwidth of a ~ 2 GHz is focused into a 2-cm long ADA doubling crystal (2). The visible light is blocked by a Corning 7-54 absorbing filter (3) that transmits approximately 80% of the 292.7 nm light. The laser light then passes into a quartz Suprasil cell (9) containing the thallium. The electric field is produced by a pair of tantalum electrodes (7) 34 mm long by 12 mm wide and separated by a distance of 6 mm, placed inside the cell and connected to the outside world via tungsten feedthroughs. A stainless steel oven (8) surrounds the cell and is kept at approximately 950°K, corresponding to thallium densities of a few times 10^{14} atoms/cm^3. A stressed quartz half wave plate (5) is used to rotate the plane of polarization of the laser light with respect to the electric field plates. The fluorescent radiation is collected by an f-1 lens, directed through a 5350 Å interference filter, ~ 2nm fwhm (10), a Polaroid HNCP37 left circular polarizer (11) and finally into an RCA 8850 phototube. A Chronectics 169 fast linear gate (13) triggered by a photodiode and discriminator (4) is used to reject any signal not coincident with the laser pulse. The signal is then integrated, amplified, digitized and stored in scalars. After every thousand pulses, in which data are taken alternately with positive and negative

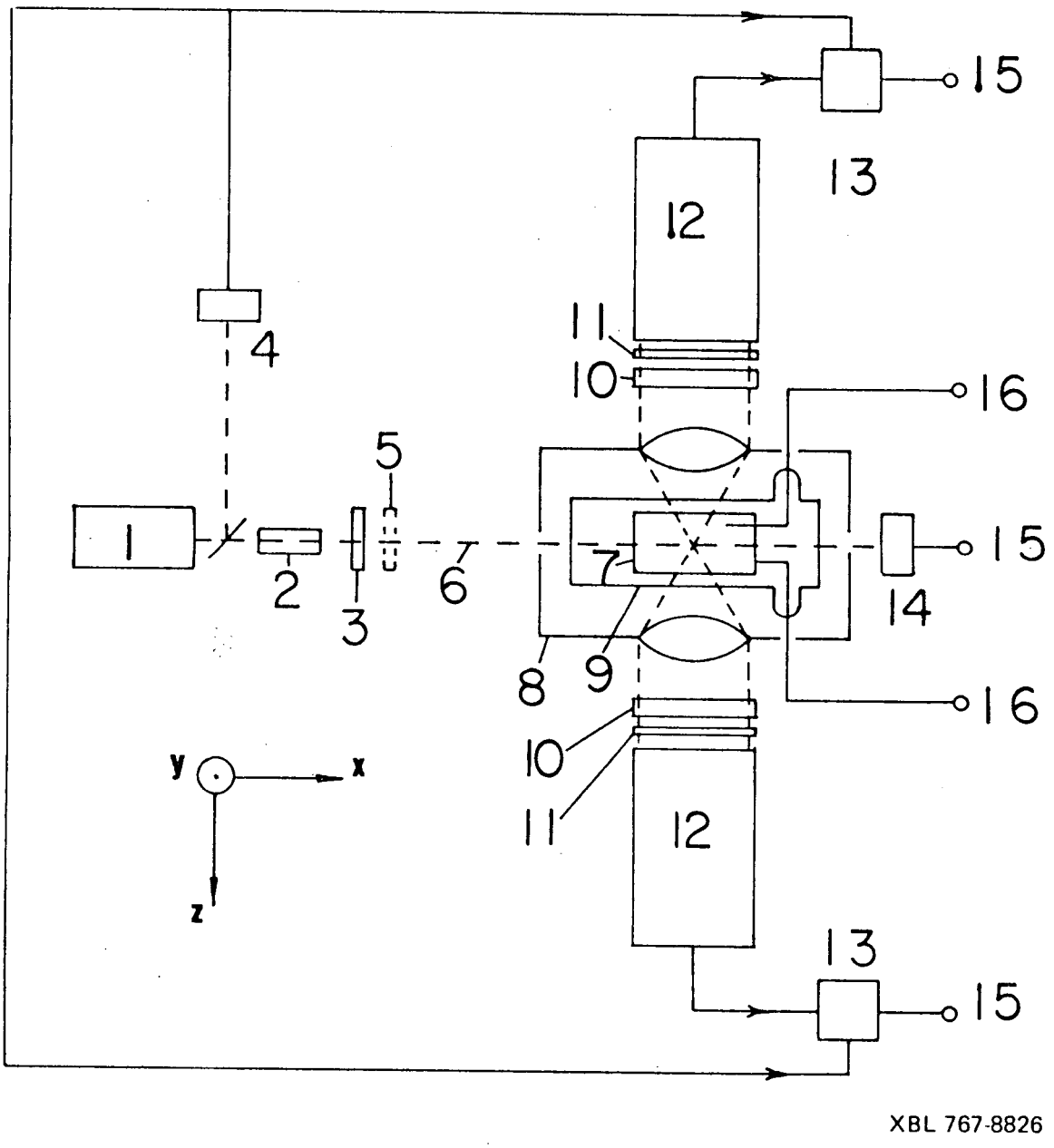

Fig. 6. Schematic diagram of the experimental apparatus.

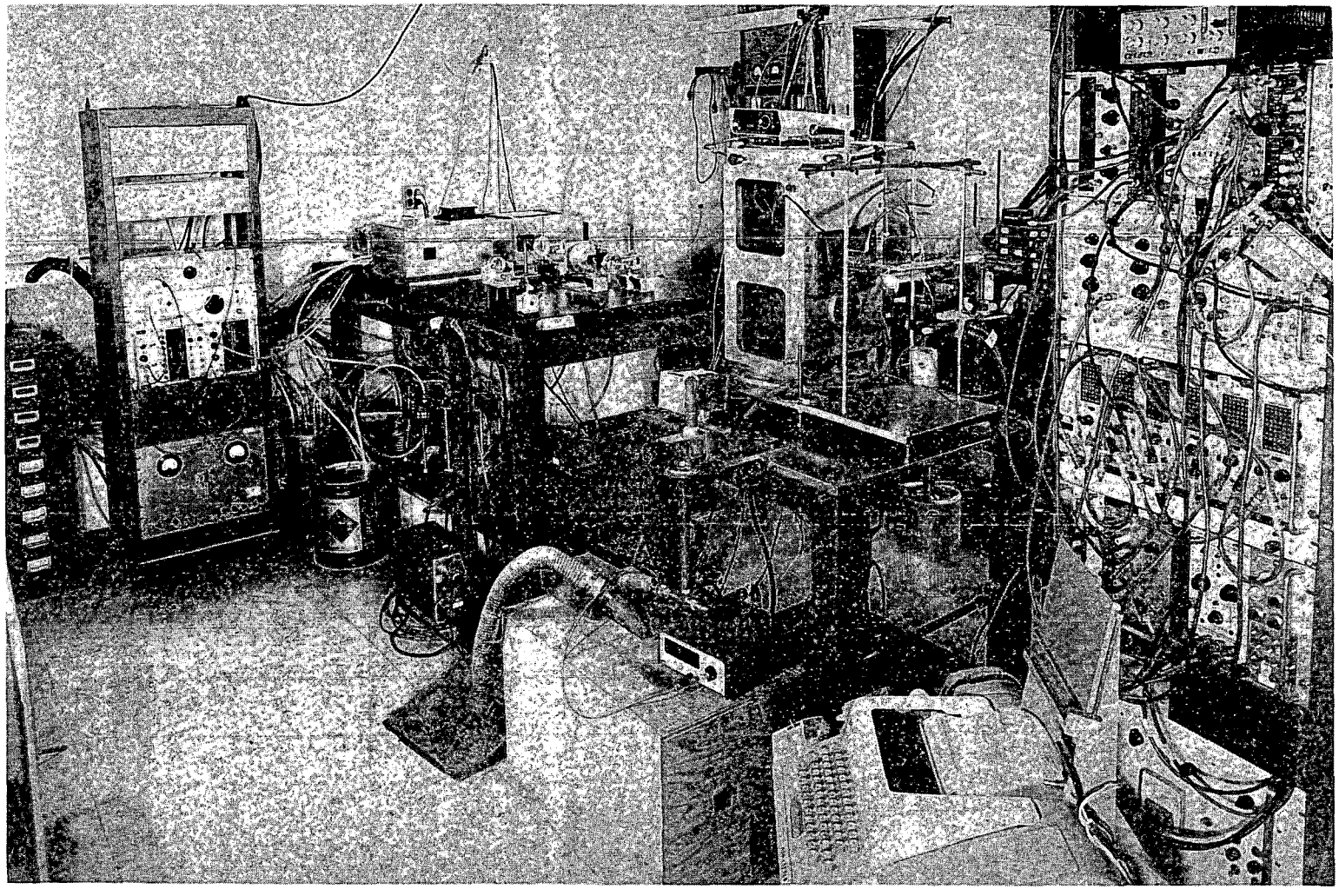

XBB 768-7333

Fig. 7. Overall view of apparatus showing from left to right laser trigger rack, laser and doubling crystal, thallium cell-oven structure, and counting electronics. The aluminum channel that runs above the apparatus is a grounding bus-bar.

electric fields, the contents of the scalars are punched out onto paper tape, and the process is repeated. After approximately 30-40 groups of 1000 laser pulses, the data on paper tape are converted onto computer cards and analyzed with the help of a small off-line computer.

A. Description of the Laser

The light source chosen to excite the $6^2P_{1/2} \rightarrow 7^2P_{1/2}$ transition in thallium is a flashlamp-pumped dye laser. The choice of the laser was dictated by the need of high average power, (much higher than nitrogen laser pumped dye lasers) but with a low duty cycle so that blackbody radiation into the detectors is not a problem. Also, since the ultraviolet light is generated by a non-linear doubling technique, high intensities of at least a few kilowatts are required. The basic principles of dye lasers are contained in many reviews, (Sna, 69), (Sor, 69), (Sch, 73) so only a description of the laser used will be presented here.

1. The Laser Head and Dye System

A diagram of the laser head and dye flow system is shown in Fig. 8. The laser head purchased from Carl Zeiss, Inc., (Model FL3B) is a polished aluminum double elliptical cavity 10 cm long flooded with distilled water, with each ellipse having a major axis of ~ 24 mm and a minor axis of ~ 21 mm. The end windows are quartz flats set at Brewster's angle and the quartz dye cuvette has a 3.4 mm inner diameter × 10 mm outer diameter with its inner surface matted to prevent "whispering" modes from lasing. Rhodamine 6G from New England Nuclear is used in a 1.5×10^{-4} molar soln in 200 proof ethanol; the concentration

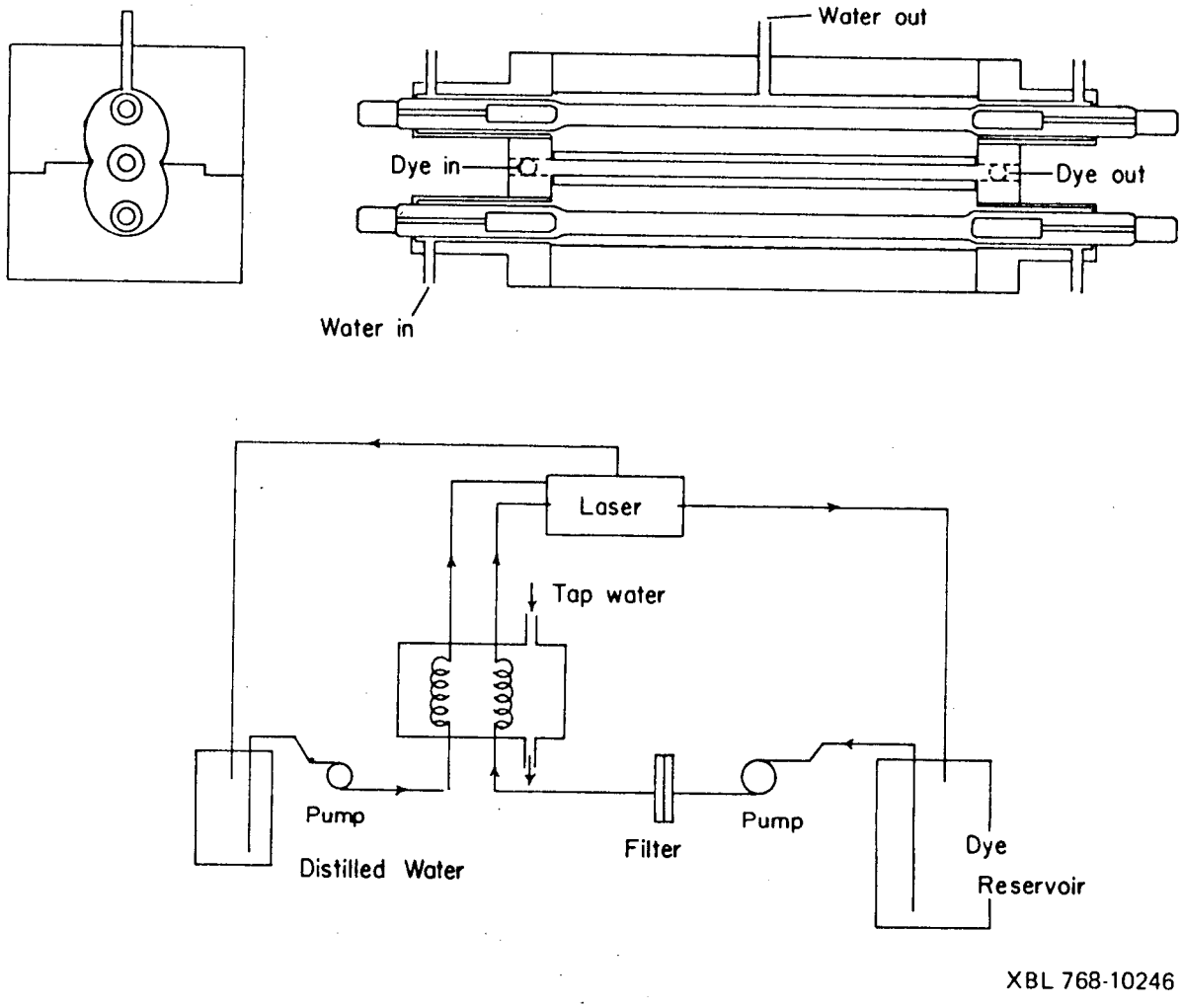

Fig. 8. Laser head and dye-flow system.

adjusted to maximize the power at 590 nm. The dye is circulated from a 5 gal. reservoir through a 5 micron Millipore teflon filter used to remove scattering centers which would decrease the laser output, (Bun, 72) and then into a heat exchanger where both the water flooding the elliptical cavity and the dye solution are brought to identical temperatures. If a heat exchanger is not used, the thermal gradients result in a distorted optical path in the dye cell, due to changes in the index of refraction from local temperature fluctuations. After passing through the heat exchanger, the dye goes directly into the laser head and is finally returned to the reservoir. A Model 12-84-303 Micropump gear pump is capable of maintaining a dye-flow of approximately three liters/min.

The large reservoir of dye is necessary because of the deterioration of R6G from the intense ultraviolet radiation of the flashlamps. We have generally been able to operate for 50,000 pulses with 10 joules of electrical energy per pulse. The problem is well known, (Ipp, 71), (Bee, 72) (Hil, 74) but is far from solved. Hidebrand (Hil, 74) has reported that oxygen is spent in the decay process, and by bubbling oxygen in the dye solution, the deterioration is slowed by a factor of 70. However, when tried on our system, no appreciable increase in the dye lifetime was seen. Filtering of the ultraviolet light below 320 nm with the use of Pyrex dye cuvettes is helpful, but since much of the R6G absorption is below this wave length, the power out of the laser is decreased. Recently, dye curvettes made from rare-earth doped quartz have been introduced by Lambda-Physik and Chromatix, and

will be incorporated into our next generation laser. These doped quartz cells absorb the harmful UV radiation, but fluoresce strongly in the blue region, and hence can extend the dye lifetime without appreciably decreasing the output laser power.

2. Electrical Discharge Circuit

The flashlamps are Model L2339 lamps manufactured by ILC, and have a 3 mm bore, 2 mm thick wall, 4 inch arc length, and are filled with 450 torr of Xenon. In our application, these lamps have shown lifetimes in excess of 4 and 5 million shots when 10 joules are discharged into two parallel lamps in approximately 1 μsec. The lamps age by showing a very gradual decrease in output light accompanied by the collection of quartz powder around the electrode region as the hot plasma ablates the walls of the lamp.

The very long life of the flashlamps results from a rather elaborate discharge circuit that also increases the power output of the laser. Ever since the earliest work with dye lasers, submicrosecond flashlamp pulses were considered desirable because of the eventual relaxation from the excited singlet states to triplet states and the subsequent quenching of the laser output (Sch, 73). Another reason for using short pulse, high current lamps is to produce more radiation in the visible and ultraviolet since it was found that higher current densities increase the temperature of the plasma discharge and the lamps become better radiators at these wavelengths (Hol, 70).

The discharge circuit can be modeled as capacitor in series with an inductor and a non-linear resistance due to the lamp (Gon, 65). (see Fig. 9)

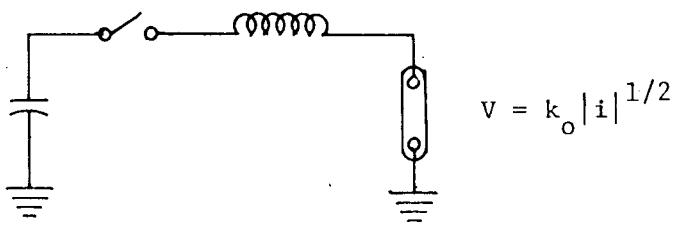

Fig. 9. Model of discharge circuit.

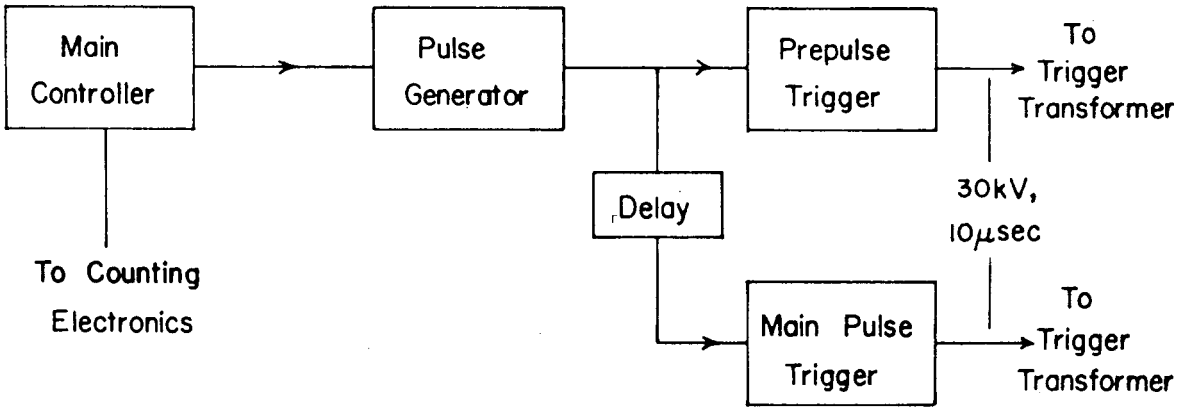

Fig. 10. Timing circuit for prepulse and main pulse flashlamp firing.

The "resistance" parameter k_0 scales with the geometry of the flashlamp as

$$k_0 = k \frac{\ell}{d} \text{ ohm(amp)}^{1/2} \quad (1)$$

where ℓ is the length of the lamp in cm, d is the bore diameter in cm, and k is a function of the pressure and type of gas used in the lamp. Typical valves of k are 1.1-1.3. With careful design of the discharge geometry, the use of a new class of extended-foil, low inductance capacitors, and low inductance spark gaps, the bulk of the inductance and "resistance" is found to lie in the flashlamps. Furthermore, it has been long known that the discharge does not begin uniformly across the entire bore of the lamp, but a very thin streamer is first started and then grows to fill the lamp. (LeC, 56) During the initial growth of the streamer, the circuit independence is much larger than the full volume discharge as given by the empirical Eq. (1).

By running the lamps in a simmering mode, (Jet, 74) in which the lamps always have 40-50 ma of current flowing through them, a thin streamer is already established. The simmer current also apparently reduces the electrode sputtering on to the walls of the flashlamp, hence, greatly increases their lifetime. Finally, the time and amplitude jitter of the discharge is greatly reduced. The speed of the discharge is further enhanced by incorporating a small prepulse several microseconds before the main pulse (Orn, 74). The small discharge does not produce enough light to significantly alter alter the populations of the energy levels of the dye molecules, but the growth period for the plasma to fill the lamp is greatly reduced. The most effective delay

between the prepulse and main pulse seems to be approximately 10 μsec, but the output of the laser is insensitive over delay changes of a few microseconds.

The timing circuit is shown in Fig. 10. The main controller also sequences the data handling electronics. The intermediate pulse generator acts as a buffer, and is needed to boost the logic pulse from the main controller in order to trigger both the prepulse trigger and the delay gate. (Ortec 416A). Both the prepulse and main pulse trigger units are basically SCR's that discharge a .5 μF capacitor charged to approximately 600 volts. Considerable diode protection is necessary since the reaction pulse generated when the laser fires could easily destroy the SCR or the transistor used to trigger the SCR.

The flashlamp firing circuit is shown in Fig. 11. The main discharge circuit consists of a .2 μF, 35 kV capacitor (Condenser Products, L ~ 10 nh) in series with a spark gap and two ILC flashlamps connected in parallel. The spark gap consists of two 1-1/2 inch diameter elkonite electrodes. (a 30% copper - 70% tungsten alloy obtainable from Mallory Corp.) with an adjustable gap, and triggered by a spark plug (see Fig. 12.) Dry nitrogen is cycled through the gap at pressures of roughly 3/4 atmosphere. The spark gap, built to replace a EGG 41-B, worked reliably for over 10^7 shots without the need to clean the electrodes. The spark gap is triggered by a 30 kV pulse from an EGG TR-60 trigger transformer isolated from the discharge circuit by 30 kV, 400 pF "TV-doornob" capacitors. A ballast resistor before the trigger pin allows the high triggering voltages to develop, but prevents large

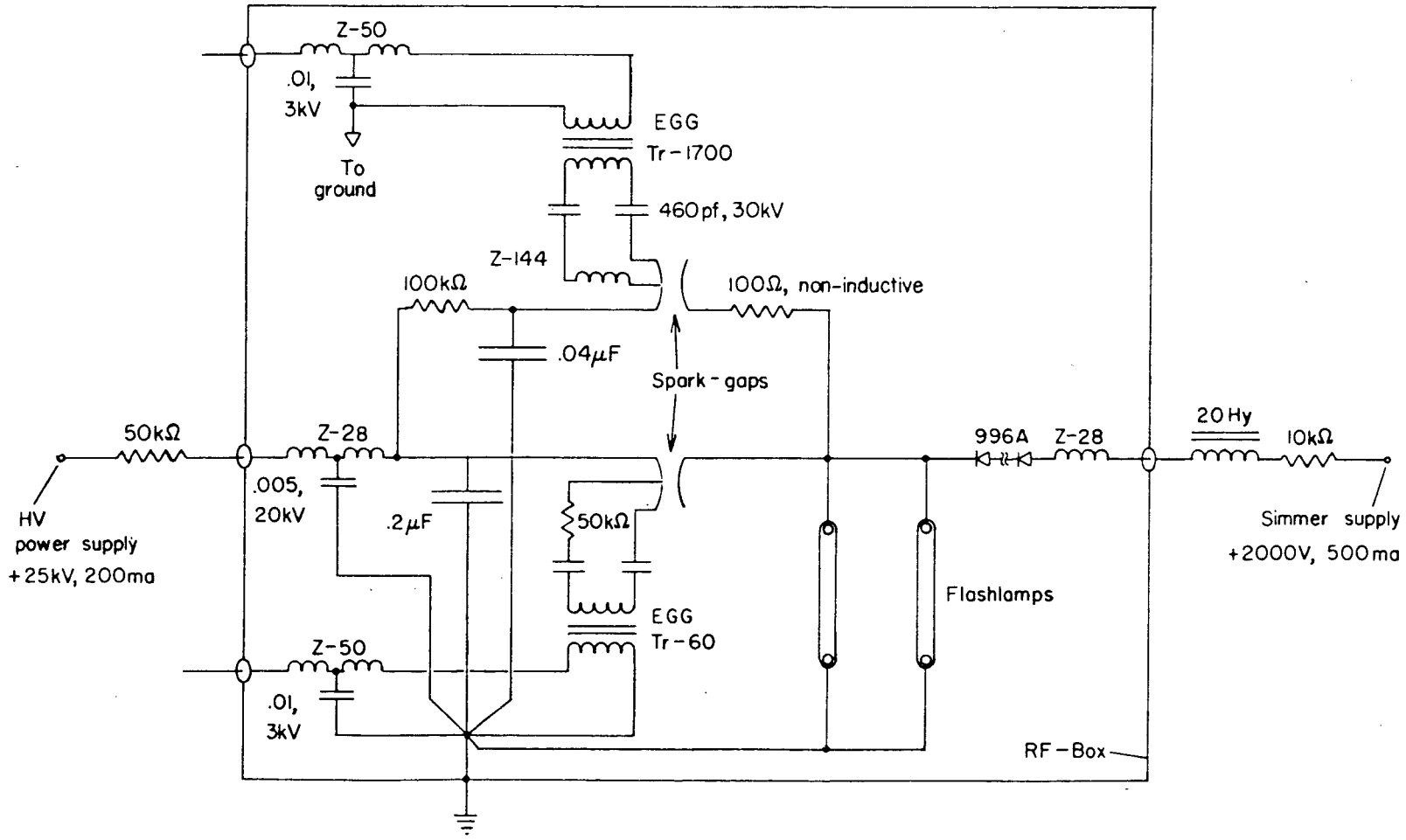

XBL 768-10247

Fig. 11. Flashlamp discharge circuit.

currents that would generate RF noise. The prepulse circuit is similar to the main discharge circuit, except that the energy discharged into the flashlamps is 5 times less and the speed of the discharge is not a consideration. The trigger pins for both discharge circuits are isolated from each other by placing the pins on the side of the spark gap away from the lamps. This geometry prevents the prepulse from also triggering the main circuit. The capacitor is a slow .04μF, 30kV GE Pyranol capacitor. The simmer supply is an unregulated 2500V, 500 ma surplus supply, isolated from the discharge circuit by a 10kΩ resistor, 20 Hy inductor, several rf chokes, and ten 996A diodes. The simmer current usually draws 80-100 ma at +1500V, and the actual voltage drop across the lamps is only a few hundred volts. The main high voltage power supply used to charge the capacitors is capable of +25kV at 200 ma but normal operating conditions call for ~10kV at 40 ma, RMS.

Characteristics of the simmer-prepulse circuit are shown in Figs. 14a and 14b. Since the output power at 293 nm is produced by non-linear "doubling" of 585 nm radiation, the power of the second harmonic varies as the square of the intensity of the fundamental frequency. Hence, even modest increases in the laser output power will result in substantial increase in doubled power.

RF noise is not a trivial problem: discharge currents of tens of thousands of amps in a microsecond or less are placed in the same room with sensitive counting electronic with 300 MHZ bandwidths. Our solution is shown in Fig. 11. The laser head and discharge circuit

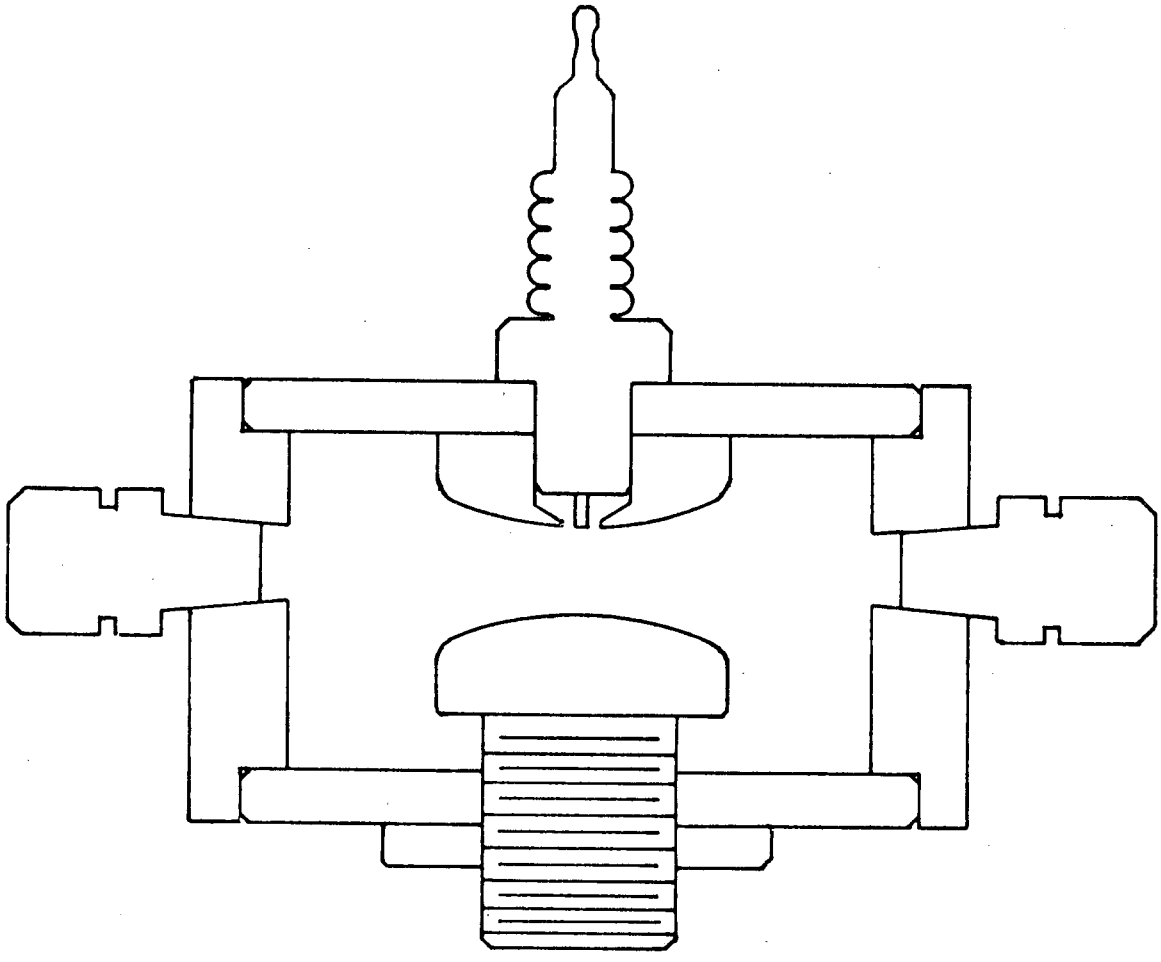

XBL 768-10236

Fig. 12. Schematic view of the sparkgap, showing the sparkplug trigger pin, the adjustable gap spacing and hose attachments for flowing N_2.

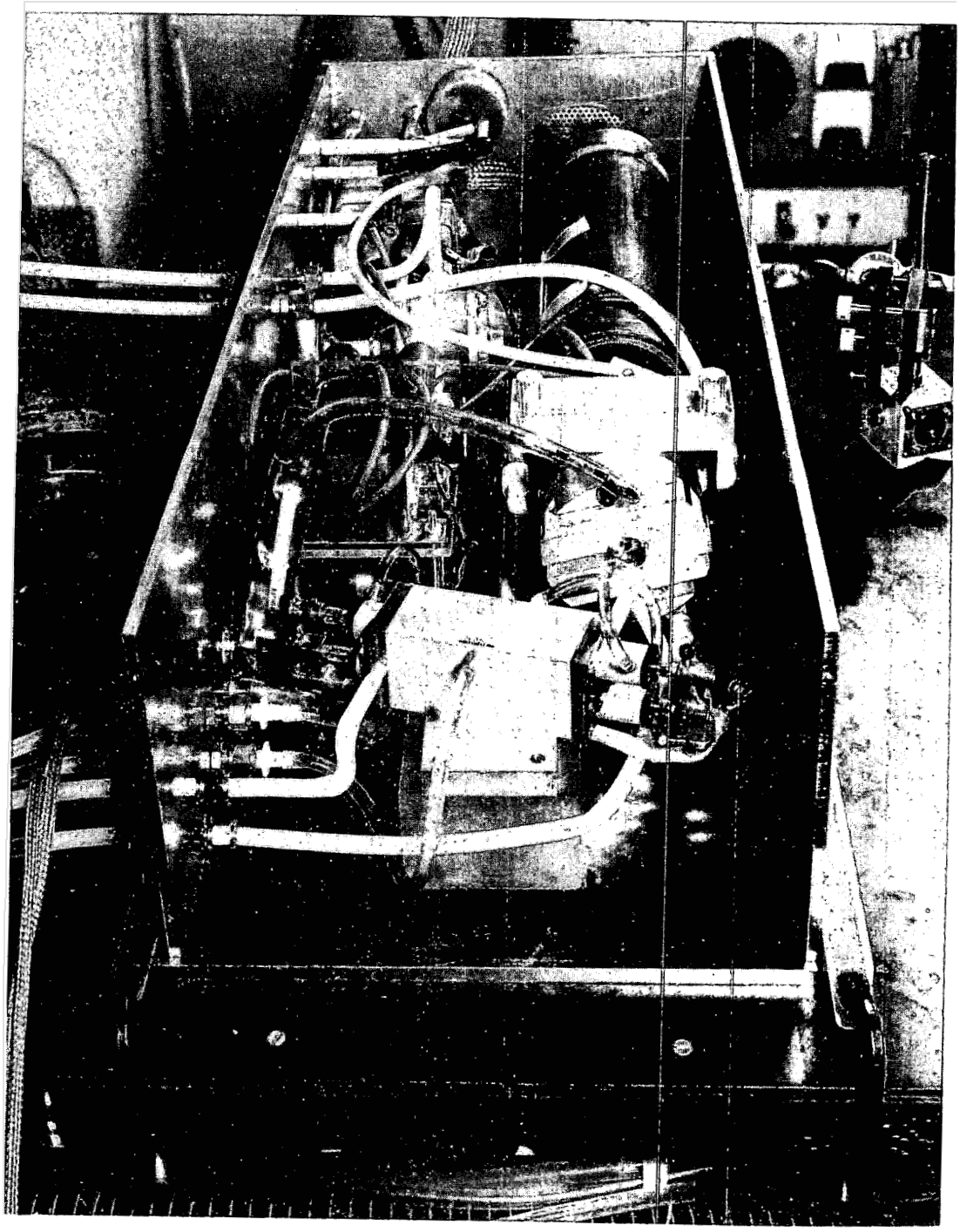

XBB 768-7332

Fig. 13. The laser head and discharge circuit. The main capacitor and spark gap are to the right, while the prepulse capacitor and spark gap are to the left and rear. The trigger transformers for both circuits are stacked on top of each other and are to the left of the main spark gap.

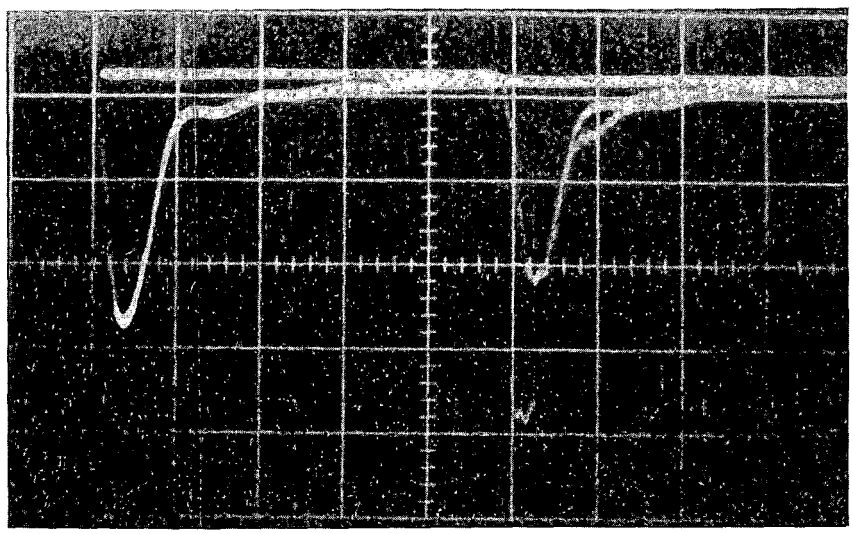

Fig. 14. Flashlamp output with simmer but without prepulse is shown in the trace on the left, and with simmer and prepulse in the right-hand traces for two delay times. The signal is form an RCA 931 photodiode and the sweep speed is 2 μs/div.

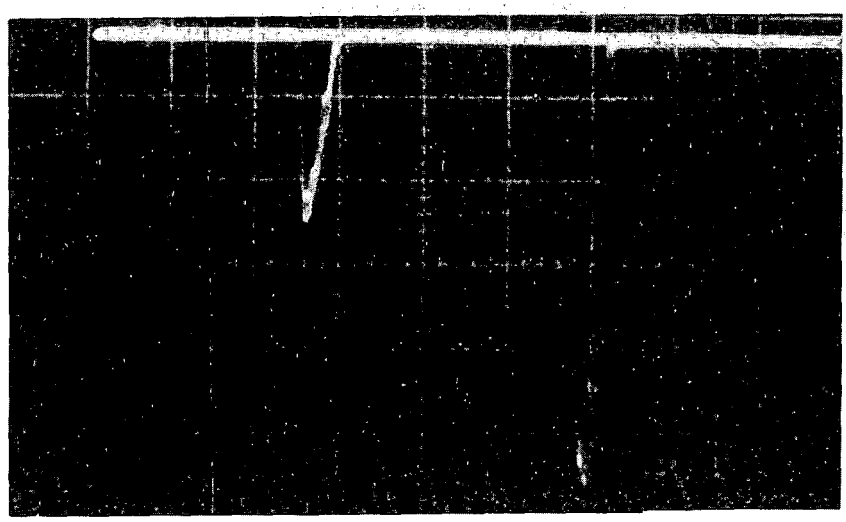

XBB 769-8096

Fig. 14b. Laser output with simmer and both with and without prepulse. The larger pulse corresponds to approximately 7 mj. Sweep speed is 2 μs/div.

is surrounded by an aluminum box and "Tee" RF filters are inserted between the discharge circuit and connections to the outside world. The timing electronics that triggers the laser are placed in a rack separate from the counter electronics, and are also electro-optically isolated from the main controller. Ground connections connect to a common point at the rear of the aluminum box, and the ground is strapped firmly via an aluminum channel beam to the copper pipe gas system that runs through the building. Similar common grounding procedures are used for the power supplies of the counting electronics. Finally, the phototubes and their bases are electrically insulated from the table holding the oven and thallium cell in order to reduce the antenna pick up.

3. Optical Cavity

The optical configuration of the laser is given in Fig. 15. The laser cavity is defined by a totally reflecting mirror (1) (R = 6m) and a 50% output coupler (R = ∞) (2). Tuning is accomplished by three elements. An interference filter (4) (90% transmission, 3 nm fwhm from Carl Zeiss) narrows the broadband lasing to ~ .6 nm with a 30% reduction in power. A 0.2 mm thick quartz etalon (2) (80% reflecting, from Burleigh) further reduces the bandwidth to 5-6 GH with another 40% power reduction. A final low-finesse thick etalon (3) (1 cm thick, 20% reflecting from Coherent Radiation) brings the linewidth down to 1-2 GH, with an additional 40% decrease in power. With clean optics, new dye, and a freshly polished elliptical cavity the dye laser is capable of producing more than 50 mj/pulse in a 6 GHz band width at 4 pulses/second. (Capacitor charged to 20 kV). However, for reliable

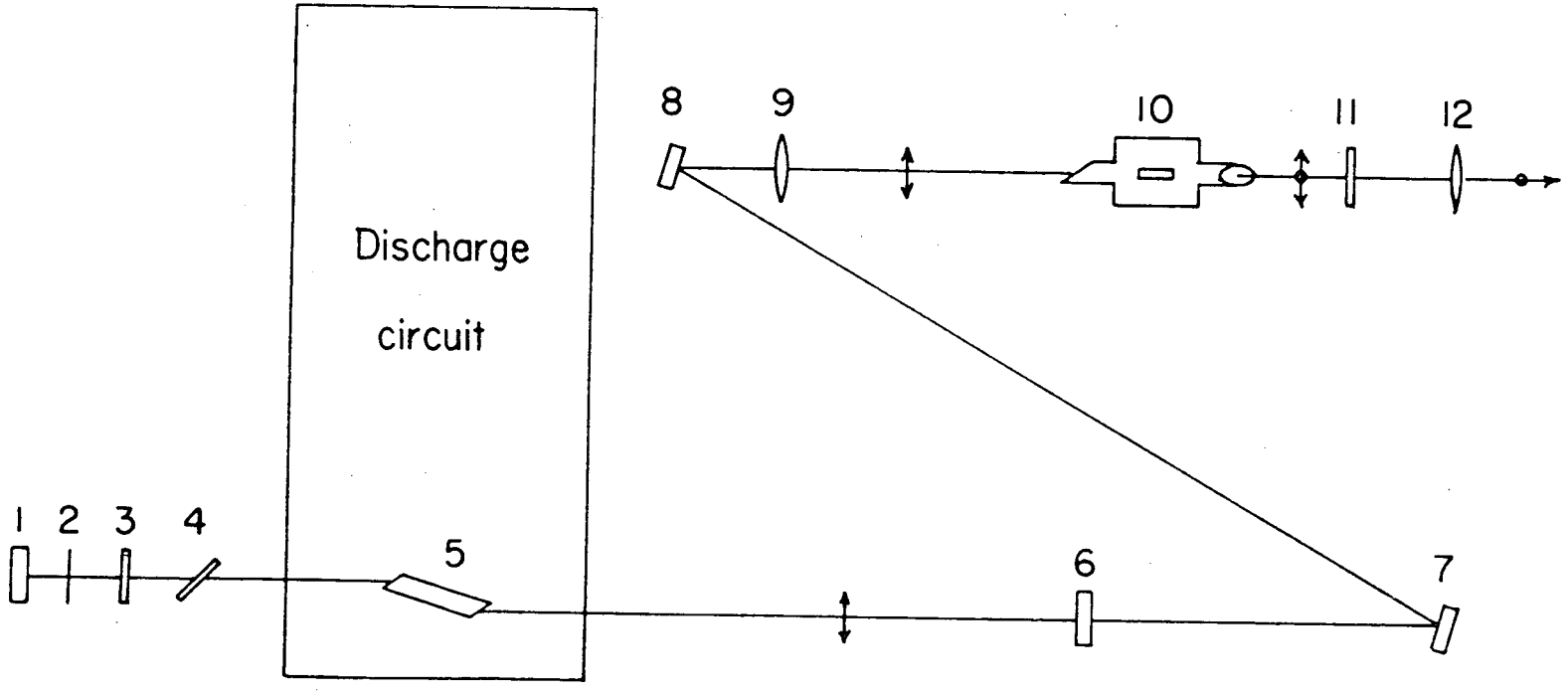

Fig. 15. Optical configuration of the laser and doubling crystal.

XBL 768-10233

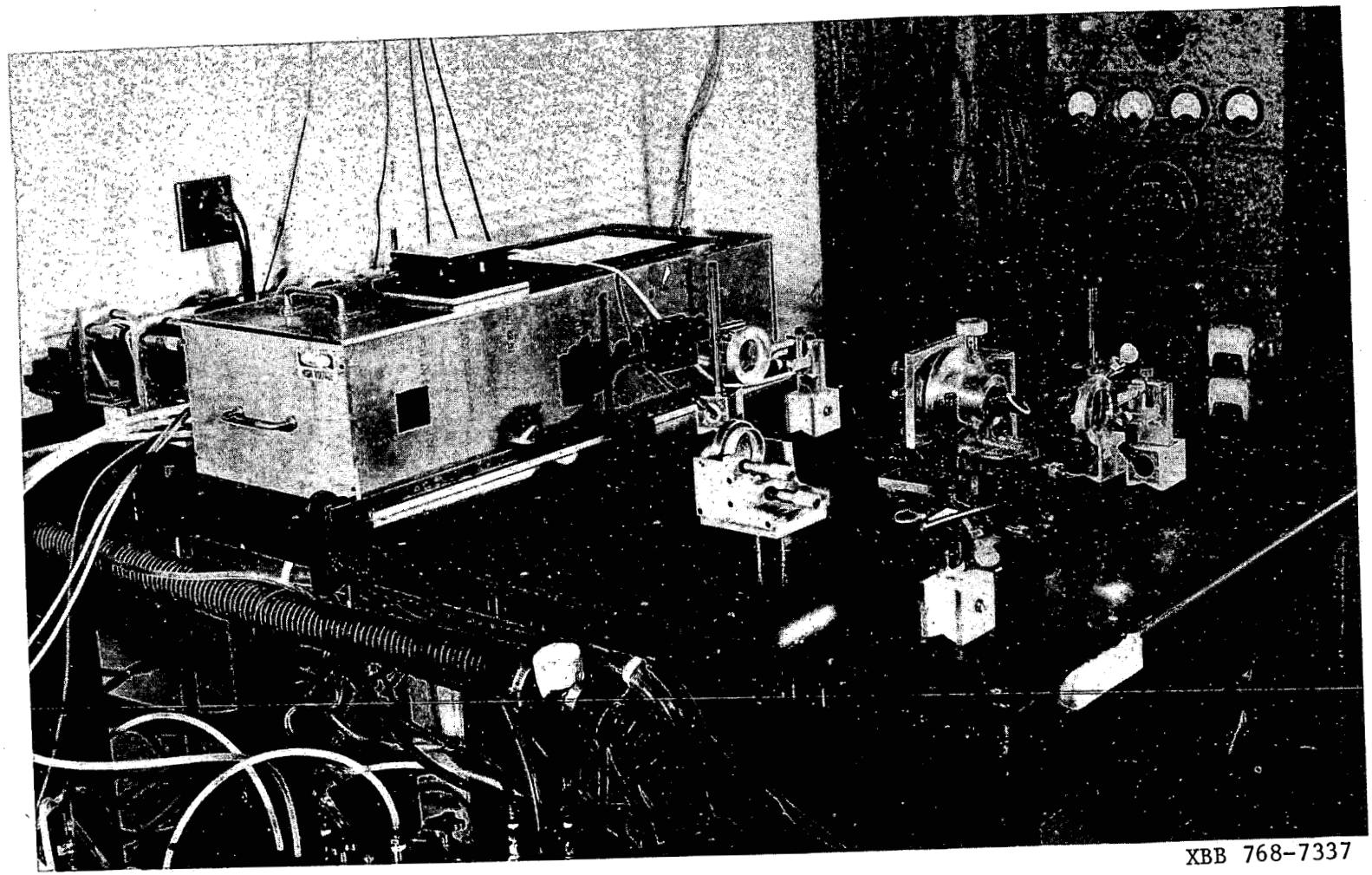

XBB 768-7337

Fig. 10. View of the laser table and the associated optics.

performance for greater than 10^7 shots, the laser is run at 8-10 kV at 10-15 pulses per second, and produces 5-10 mj/pulse in a 2 GHz bandwidth.

4. U-V Generation

After leaving the output coupler, the laser beam is focused into an ADA crystal (10) (6 mm × 6 mm × 2 cm from Cleveland Crystal) and 5-10% of the intensity at the fundamental frequency is converted into 292.7 nm light. The efficient doubling results from 90° phase matching accomplished by temperature tuning the crystal. (Adh, 73). (For a basic introduction to non-linear doubling, see (Yar, 75)). An aluminum oven keeps the crystal at a temperature of approximately 30°C, constant to better than .05°C per °C change in the ambient room temperature. The temperature is sensed with a thermistor (embedded in the oven) that forms one leg of a modified A.C. Wheatstone bridge (from Oven Industries). The output of the bridge is an error signal that is used to drive an immersion heater that heats water which then flows through the aluminum block. The hydroscopic ADA crystal is protected from moisture by a pair of O-ring-sealed brewster windows and dessicant placed in the oven cavity. A 30 cm focal length lens (9) focuses the laser light into the crystal. The focal length is determined by the damage threshold of the crystals, and although damage levels of up to 300 megawatts/cm^2 have been claimed for ADA, we have been unable to obtain crystals of such high purity. The entire oven assembly is mounted to permit small adjustments along all six degrees of freedom.

The 585 nm light is blocked by a Corning 7-54 glass filter (11) that allows ~ 80% of the 293 nm light to pass through. A 25 cm f.l. quartz lens (12) recollimates the beam and directs it into the oven chamber containing the thallium. The zig-zag path of the light is purely a convenience that permits the laser and doubling crystal to sit on a single 3 ft × 6 ft table.

The doubled light is polarized perpendicular to the undoubled light, and normally enters the thallium cell parallel to the static electric field. If we desire the polarization to be perpendicular to the electric field, a half-wave plate is inserted after the 25 cm f.l. quartz lens. By rotating the fast-slow axis of the half-wave plate with respect to the laser polarization, the plane of polarization of the 293 nm light can be rotated by an arbitrary amount. The half-wave plate is made from a stressed fused quartz disk, one inch diameter × 3/8 inch thick. A UV glan-laser prism (Karl Lambrecht) placed before the normalizing photodiode is used to check the effective rotation of the polarization. When the stress axis of the quartz disc is parallel to the light polarization, there is no rotation and the analyzing glan-prism transmits maximally. When the stress axis is rotated 45° away from the incident polarization, maximum extinction occurs. Typical extinction ratios are 100 to 1. Since the stress on the quartz will relax after a long period of time, the extinction ratio is always measured just before and immediately after a run.

B. Thallium Cell and Oven

An elaborate quartz cell was constructed to obtain ultra-pure thallium in an effort to reduce the background. Although the complete system was not used in the eventual experiment, a brief description will be included since it will be pertinent to a discussion of the background.

A quartz cell system is the natural choice since quartz is chemically relatively inert, transparent at 293 nm and 535 nm, workable using conventional glass-blowing techniques, and able to withstand the high temperatures needed to produce the necessary vapor pressure of thallium. After some preliminary work with sealed-off cells, it was realized that the quartz walls were overly permeable to air in the temperature range of 900° - 1000°K (Dus, 62) and we feared that the thallium might combine chemically with hydrogen, nitrogen, and oxygen. Consequently, the entire system was surrounded by a crude mechanical pump vacuum of ~ 30 microns. Also, a means of vacuum distilling thallium into the cell was devised, using a set of three electromagnetically operated quartz valves.

Figure 17 shows a schematic view of the thallium cell and bake-out system, while Figs. 18 and 19 give views of the vacuum system and cell-oven structure. The procedure for filling the cell goes as follows: An initial bake out begins with all valves open and no thallium placed in the system. Region A. is brought to 600°C while regions B and C are kept at 750°-800°C for several hours. The rest of the vacuum system up to a Varian Bakeable valve is kept at ~ 250°C. The system is allowed to cool down and a few milligrams of 99.9999% pure thallium

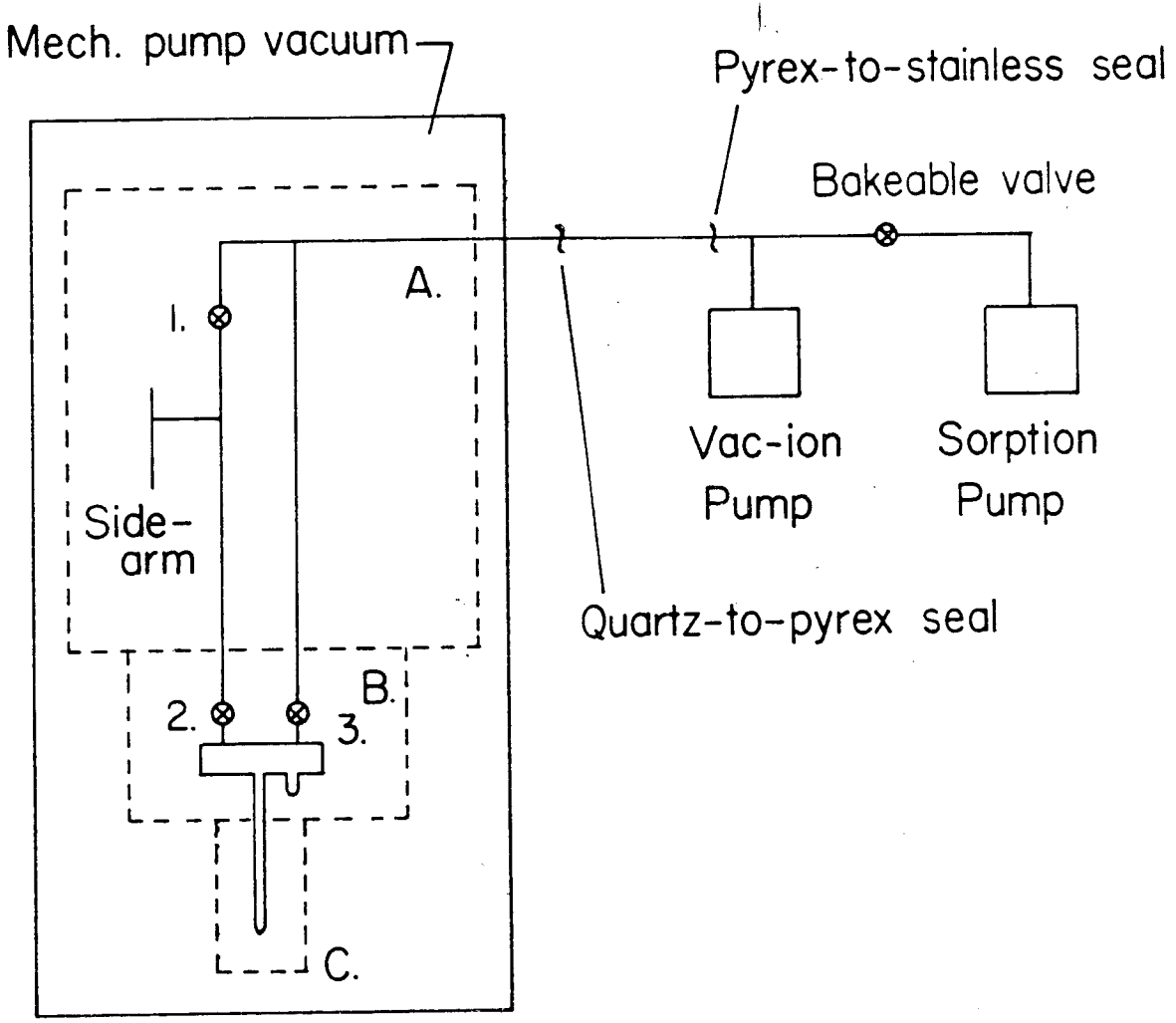

XBL 768-10232

Fig. 17. Schematic view of thallium cell and distillation system.

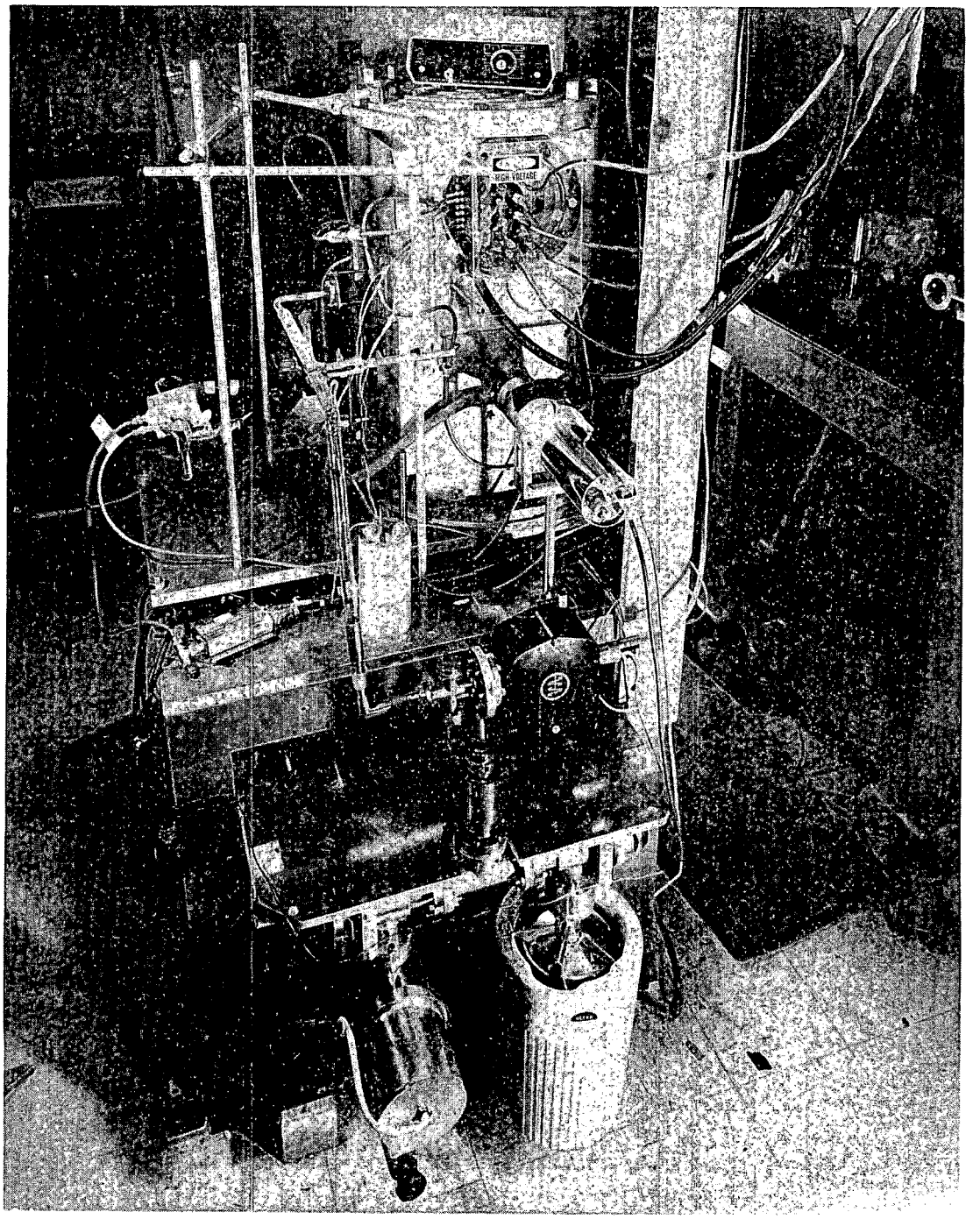

XBB 768-7334

Fig. 18. View of the north phototube, crude vacuum chamber, and vacuum pumping apparatus. The vac-ion pump is in the center of the photograph and the sorbtion pump is seen in the lower right hand corner. A cryolite trap is at the lower corner, and connects to a mechanical pump.

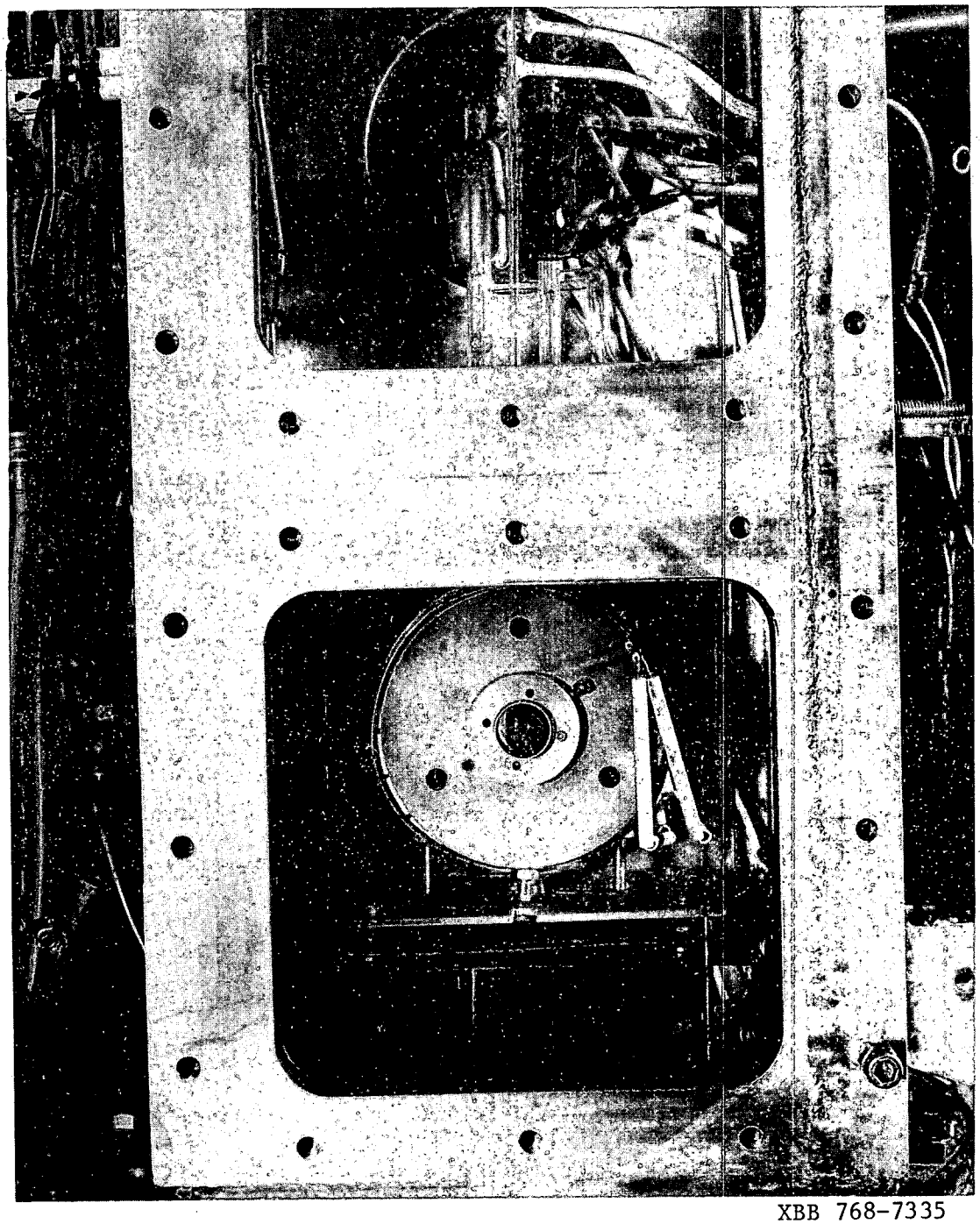

XBB 768-7335

Fig. 19. View of the south-side of the apparatus with the phototube and vacuum chamber panels removed. Coils for lifting the quartz valves are shown above. Half of the radiation shield has been removed to show the main oven. The stem-radiation shield is visible below the main oven assembly.

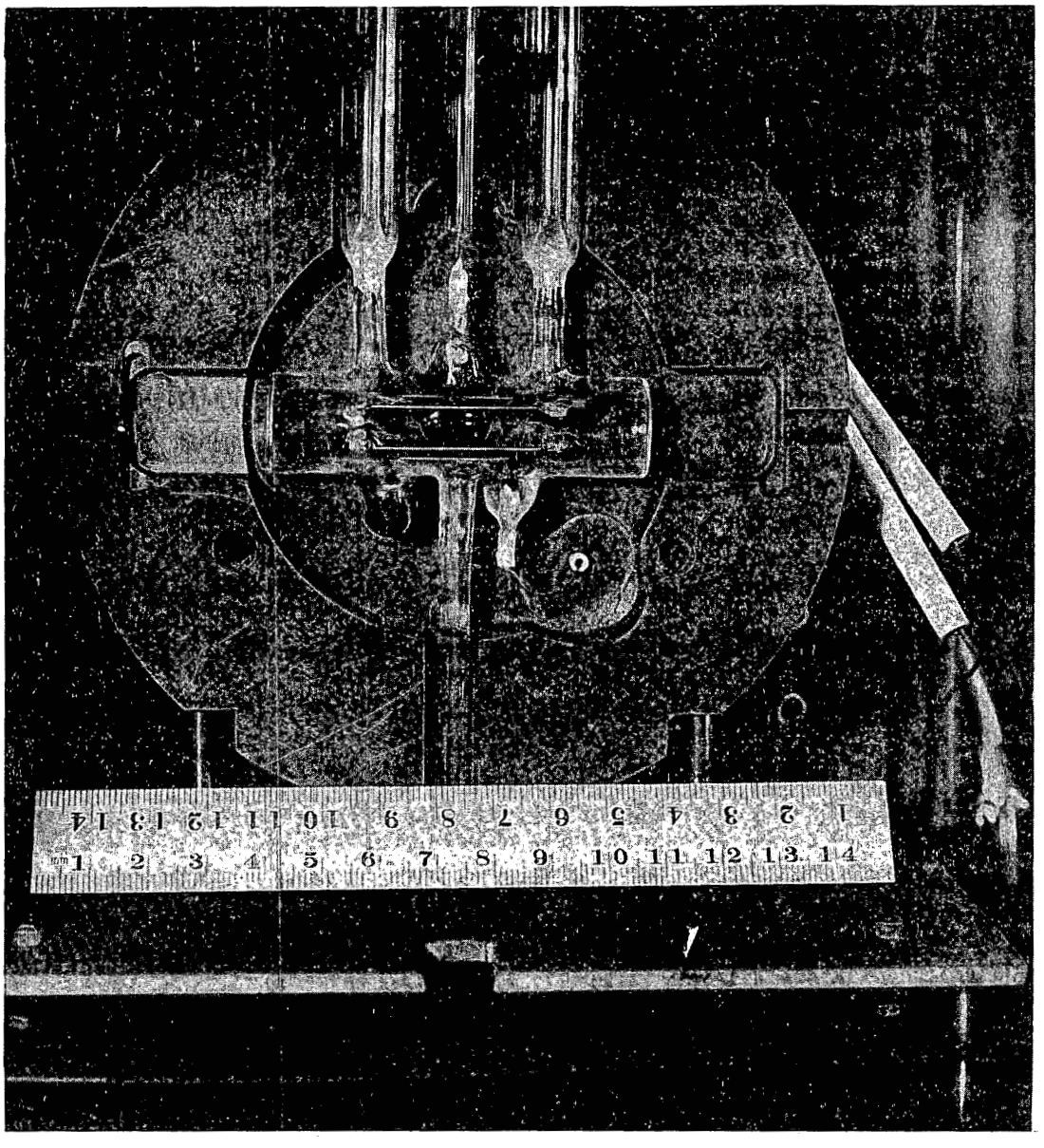

XBB 768-7338

Fig. 20. Detailed view of the thallium cell. Half of the main oven is removed to reveal the electrode structure in the cell and the feed-thru system used to produce the electric fields. The bottom portion of the quartz valves are also visible.

metal (Alfa Ventron) is placed in a side arm. Valve 2 is then shut while valves 1 and 3 are left open and the oven regions are again brought to high bake-out temperatures for a few more hours. Thallium is finally distilled into the stem in region C by closing valves 1 and 3 and opening valve 2. Regions A and B are kept hot while the stem is allowed to cool down. Four to eight hours are required to distill enough thallium into the stem in order to maintain densities of a few times 10^{14} atoms/cc. Periodically, valve 3 is opened to allow any "volatile" impurities to escape from the cell. After a few days of running, the cell becomes very clean and pressures below 10^{-10} torr at the pump are commonly obtained when the system is allowed to cool. Even when the cell is run at 950°K, vacuums at the pump are generally around 10^{-8} torr. The pumping speed of our cell, calculated from standard formulas found in Dushman (Dus, 62), is about 1-2 liters/sec.

The details of the quartz valves are shown in Figs. 19 and 20. The valve is basically a ground ball joint connected to a quartz rod and finally to a steel slug vacuum-sealed in a quartz vial. An electromagnet, made from about 60 turns of no. 14 copper wire wound in 3 layers, is placed around the steel slug. Approximately 12-15 amps are required to lift the valve open. Normally used insulating materials are not capable of withstanding the 600°C used in the distilling procedure. The coils are kept from shorting by winding the copper around a teflon form, springing it slightly and applying several coats of dilute Seuereisen ceramic cement (from the Sauereisen Cement Co.). After the cement dires, another layer of wire is wound and painted

with the cement.

Despite all our attempts to produce ultra-pure thallium, the background persisted, and we now know that such elaborate procedures are unnecessary. The current procedure is simply to place the thallium directly in the stem, bake regions A and B for a few hours while leaving C and the rest of the plumbing cold. The cleanliness is not completely lost since the cell can still be periodically purged of any impurities liberated from the quartz walls or the thallium metal. A small amount of Getterloy (an effective bulk getter that is an alloy of titanium and zirconium) is also placed in a small pocket of the cell to help speed up the cleaning procedure.

The thallium cell, stem, and side-arm constructed from Suprasil quartz, (Amersil) a high purity quartz which is more inert chemically than commercial grade quartz. The remainder of the valve assembly is made of commercial grade quartz. The main oven, (Region B of Fig. 17) made from stainless steel is shown in Fig. 20. (A copper oven was originally used, but the copper reacted with the quartz cell at high temperatures, and frosted the quartz.) Heater elements, made from No. 18 nichrome wire, are wound helically and the toroids are then arranged around the oven to further cancel magnetic fields. The conical section between the cell and the quartz lens, and the tube extending after the lens are used to reduce radiation losses from the center of the cell. Otherwise, these losses could cool the cell to the point where thallium would condense on the sides walls and block the 535 nm light. A separate counterwound helical coil is used the heat the stem

that extends below the cell. Under operating conditions, the stem is kept approximately 50°C cooler than the main oven. A 3-layer, stainless steel heat shield surrounds both the stem and main oven. The shield provides a factor of 2 to 3 reduction in the radiation losses. Typically, 75 volts D.C. at 11 amps are needed to heat the main oven up to 950°K.

All temperatures are monitored by chromel-alumel thermocouples using an ice bath reference and read by a digital voltmeter. Calibration curves are taken from the AIP Handbook (Aip, 63). The density of thallium is then estimated from the known vapor pressure of thallium (Nes, 63) using an effective stem temperature, and a perfect gas law approximation using the cell temperature.

C. Counting Electronics

A block diagram of the counting electronics is given in Fig. 21 along with a schematic of the experimental apparatus already described in the introduction of this chapter. The signals coming from the two phototube channels (12) and the normalizing RCA 935 vacuum photodiode (14) are fed into integrators (18) (modified charge sensitive preamp, LBL # 11×4830) that sum the total charge in each pulse. A charge of 2.10^{-4} coul. is converted into a ~1 volt voltage pulse. The voltage pulse is amplified and shaped by a high rate linear amplifier (19), (LBL #11×5501 P-1) and the peak voltage is held by a pulse stretcher and linear delay (also 19) (LBL # 11×9421 P-2). The signals are then sent sequentially into a mixer, (LBL # 11×5511 P-1), and an ADC (Nuclear Data Model 560). From the ADC, the signals are stored in

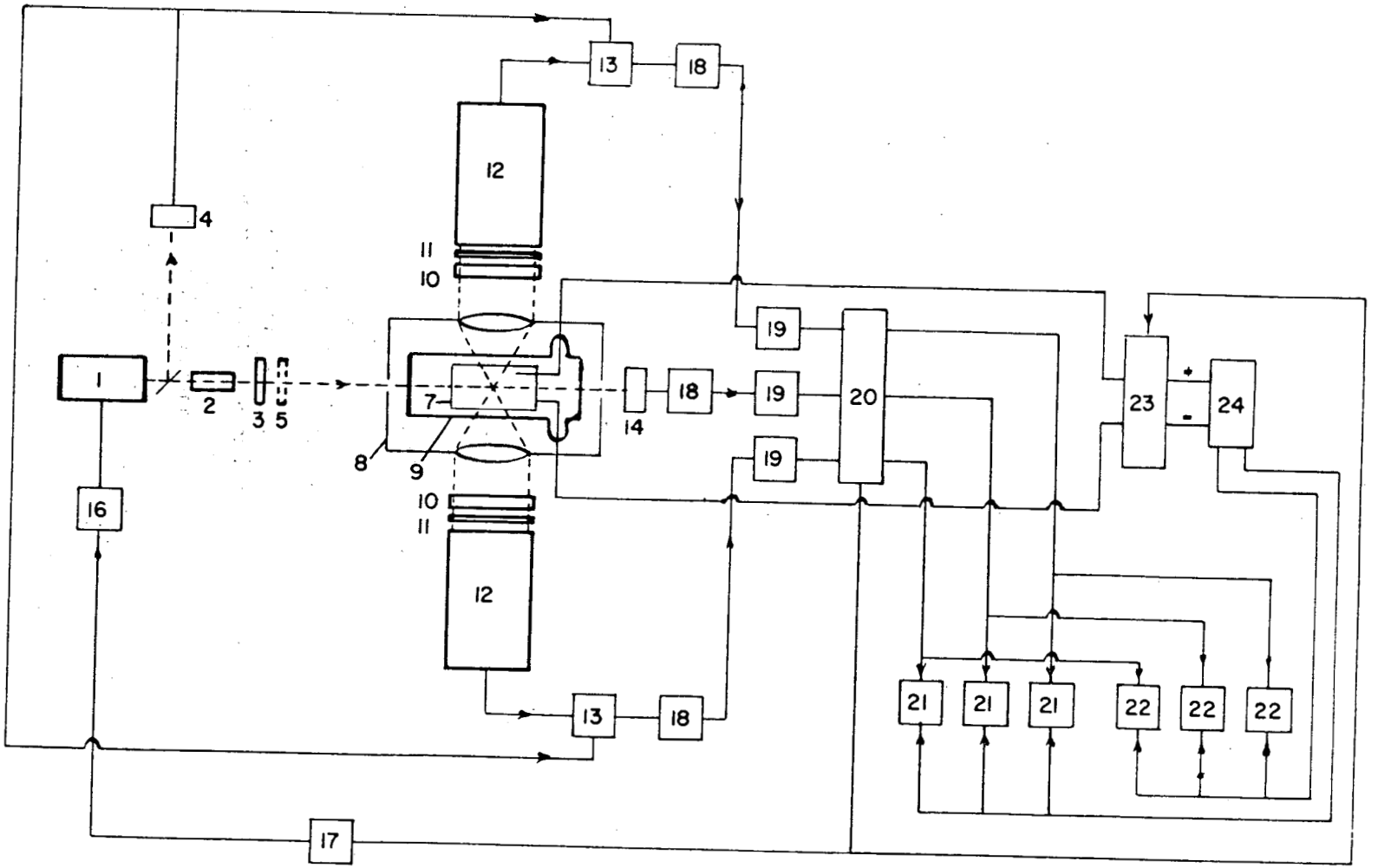

Fig. 21. Schematic diagram of the apparatus and associated counting electronics. XBL 768-10242

either one of two sets of scalers, (Ortec Model 40) corresponding to positive or negative electric fields in the thallium cell (7). A controller (17) that runs from an internal clock (555 timer) coordinates the laser triggering circuits ((16) and Fig. 9) with the electric field switcher (23) and the sequential analog to digital conversion. The scalers are gated on and off (24) so that one set of scalers (21) stores positive electric field signals and the other set (22) stores negative electric field signals. After 1000 shots, the contents of the scalers are printed out on paper and also punched on paper tape by a Teletype. The electric field switcher can reverse the electric field every n laser pulses (n = 1 to 10), but is generally set to switch the field after every pulse. After each run of ~40 sets of 1000 laser pulses, the data on paper tape is punched out onto computer cards and fed into an IBM 1620 computer.

D. Data Handling

We measure the quantities

$n_{\pm}^{on}$ = scaler counts in the north (-z) direction taken on resonance for + and - electric fields

$s_{\pm}^{on}$ = scaler counts in the south (+z) direction taken on resonance for + and - electric fields

$P_{\pm}^{on}$ = normalizing photodiode counts

and similar quantities

$n_{\pm}^{off}$, $s_{\pm}^{off}$, $P_{\pm}^{off}$ for off resonance data

The normalized signals are

$$N_{\pm}^{on} = \frac{n_{\pm}^{on}}{P_{\pm}^{on}} \quad , \qquad N_{\pm}^{off} = \frac{n_{\pm}^{off}}{P_{\pm}^{off}} \quad , \text{ etc.}$$

Now define

$$\Delta_{\pm} = \frac{(N_{\pm}^{on} - N_{\pm}^{off}) - (S_{\pm}^{on} - S_{\pm}^{off})}{(N_{\pm}^{on} - N_{\pm}^{off}) + (S_{\pm}^{on} - S_{\pm}^{off})} \quad .$$

A small correction is applied to all the data because the ADC gives a slight positive baseline offset when the signal out of the ADC is plotted as a function of the signal in. The correction is approximately 5-10% of the total number of scaler counts.

The experimental asymmetry is defined to be

$$\Delta_{+,-} = \frac{1}{2} (\Delta_{+} - \Delta_{-})$$

As a check on our data handling procedure, we also analyze the data in terms of an asymmetry

$$\Delta_{N,S} = \frac{1}{2} (\Delta_{N} - \Delta_{S}) \ ,$$

where

$$\Delta_{N} = \frac{(N_{+}^{on} - N_{+}^{off}) - (N_{-}^{on} - N_{-}^{off})}{(N_{+}^{on} - N_{+}^{off}) + (N_{-}^{on} - N_{-}^{off})} \ , \text{ etc.}$$

The quantities $\Delta_{+,-}$ and $\Delta_{N,S}$ always are found to agree with each other to better than 1%.

IV. THE EXPERIMENTAL RESULTS

A. The Electric Field-Induced E1 Transition

The transitions between the various hyperfine levels of the $6^2P_{1/2}$-$7^2P_{1/2}$ states of thallium in the presence of an electric field are measured with the circular polarizers removed. The reader is referred to Figs. 4, 5 and Table III in part B of section II for a summary of the various predicted selection rules and transition rates for the field induced transitions.

In Fig. 22, the results of a frequency scan are shown. The laser has only one etalon inserted in the cavity so that the bandwidth does not resolve the $7^2P_{1/2}$ hyperfine splitting. The polarization of the laser is parallel to the electric field ($\hat{\epsilon} \parallel \underline{E}$), and the allowed transitions from the two $6^2P_{1/2}$ hyperfine levels are clearly resolved. The ground state hyperfine splittings are well known:

$$\Delta\nu(6^2P_{1/2}, {}^{203}\text{Tl}) = 21.1 \text{ GHz}, \quad \Delta\nu(6^2P_{1/2}, {}^{205}\text{Tl}) = 21.3 \text{ GHz}.$$

The horizontal frequency scale is taken directly from divisions on the differential screw used to tilt the etalon, and the vertical scale is counts in arbitrary units. The 3 to 1 ratio in the rates for the $F = 1 \rightarrow 1$ and $F = 0 \rightarrow 0$ transitions shown in Fig. 22 is simply the ratio of statistical weights. The non-resonant background can also be seen as an upward shift of the resonance curves by one unit. Each data point corresponds to 200 shots and the entire scan is completed in about 3 minutes.

Figure 23 shows a simultaneous scan of the $\hat{\epsilon} \parallel \underset{\sim}{E}$ transition F = 1→1 and the $\hat{\epsilon} \perp \underset{\sim}{E}$ transitions F = 1→0, 1. Both etalons are used in the laser, and the linewidth is estimated to be 2 GHz. For each differential screw setting, 200 laser shots were taken for both polarizations of 292.7 nm light. The incident light polarization is rotated using the stressed quartz half-wave plate. The distorted line shape of the perpendicular polarization shows a barely resolved $7^2P_{1/2}$ hyperfine splitting.

Figure 24 shows transitions originating from the F = 0 ground state of $6^2P_{1/2}$ for both parallel and perpendicular polarizations. The selection rules only allow F = 0→0 when $\hat{\epsilon} \parallel \underset{\sim}{E}$ and F = 0→1 for $\hat{\epsilon} \perp \underset{\sim}{E}$, and the upper state hyperfine splitting becomes clearly resolved. This splitting has been measured recently by Flusberg, et al. (Flu, 76) using a two-photon doppler free spectroscopy method, and is found to be 2.13 GHz. The widths and separation of the resonance curves in Fig. 24 actually provide the best measurement of the linewidth of the doubled laser light. If we assume that the laser width is a gaussian distribution, the total line width measured is given by

$$\Delta\nu_{tot} = \sqrt{(\Delta\nu_{laser})^2 + (\Delta\nu_{doppler})^2} \qquad (1)$$

From Fig. 24, $\Delta\nu_{tot} \approx 1.2\ \Delta\nu_{hfs}(7^2P_{1/2}) = 2.56$ GHz. $\Delta\nu_{doppler} = 1.13$ GHz at 950°K. Hence,

$$\Delta\nu_{laser} = 2.3 \text{ GHz} .$$

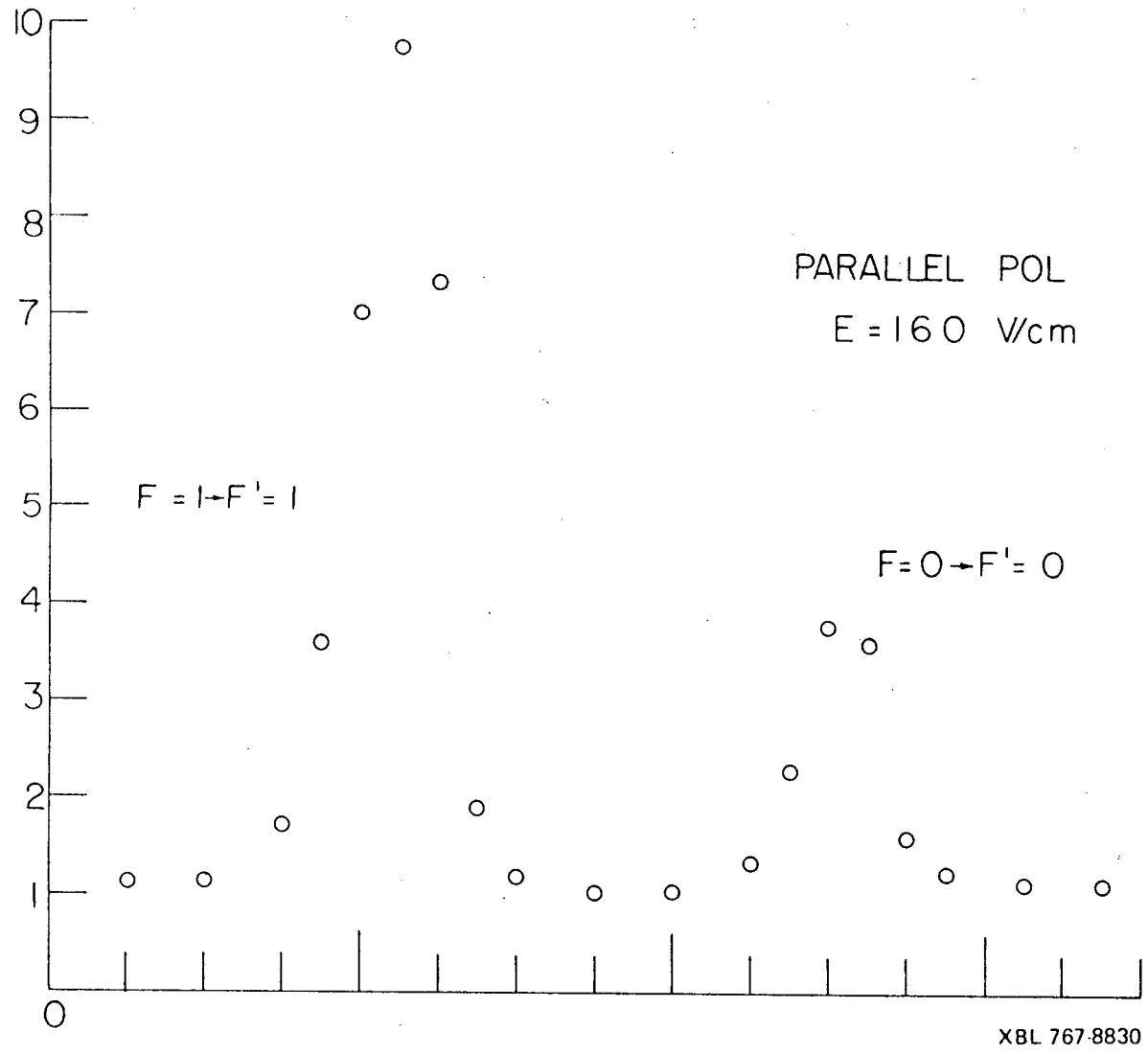

Fig. 22. 535 nm fluorescence intensity in arbitrary units vs. wavelength of the incident laser light in etalon micrometer settings for $\underset{\sim}{\varepsilon} \parallel \underset{\sim}{E}$.

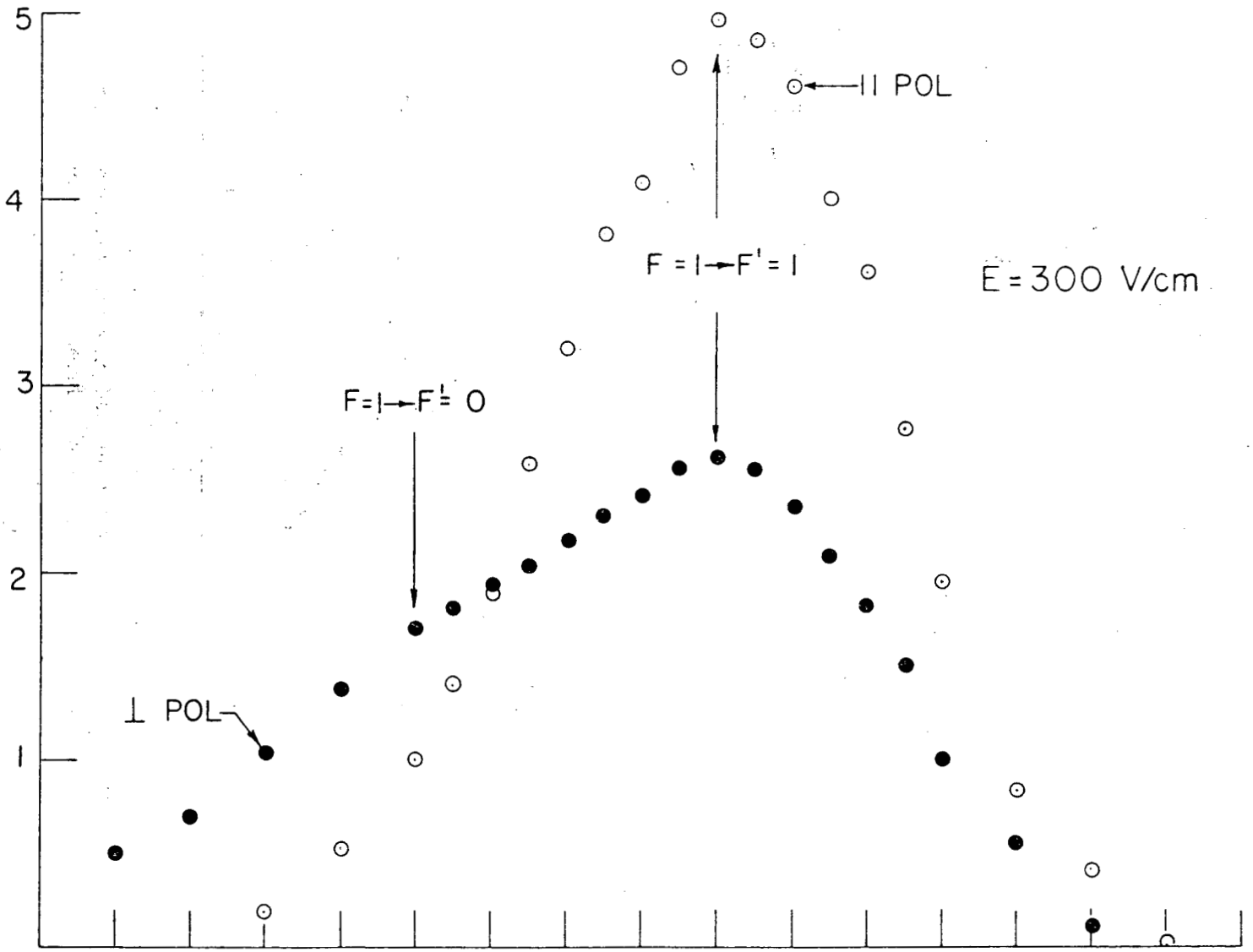

Fig. 23. 535 nm fluorescent signal vs wavelength for $\mathcal{E} \parallel E$ and $\mathcal{E} \perp E$ transitions from the F=0 ground state.

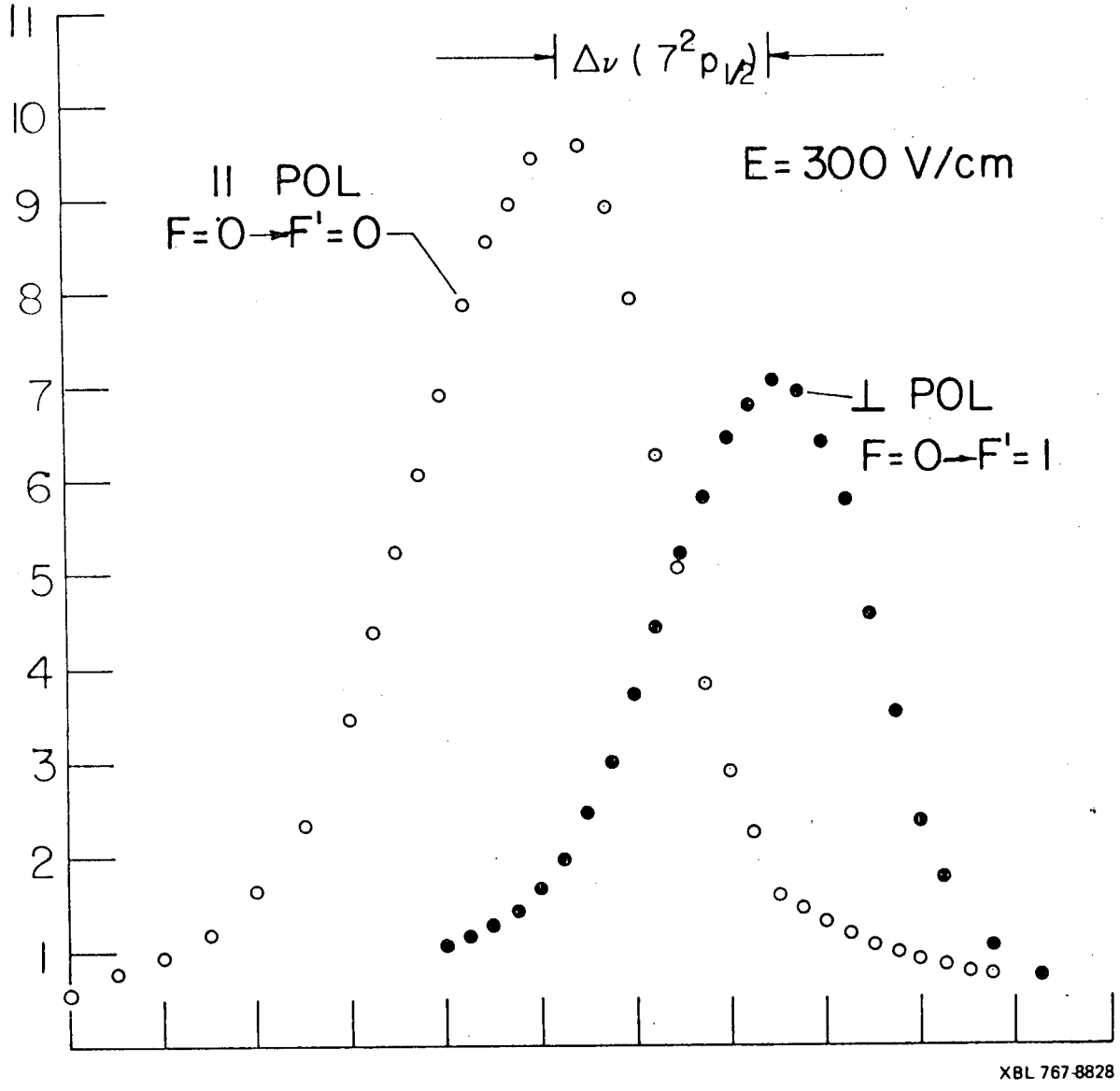

Fig. 24. 535 nm fluorescence signal vs wavelength for $\mathcal{E} \parallel E$ and $\mathcal{E} \perp E$ transitions from the F=0 ground state.

The ratio β/α can be determined from Figs. 23 and 24. From the rates calculated in part B of section II, we have

$$\frac{(F = 1 \to 1,\ 0)}{(F = 1 \to 1)_{\parallel}} = \frac{\frac{3}{4}\beta^2}{\frac{3}{4}\alpha^2} \quad , \tag{2}$$

and

$$\frac{(F = 0 \to 1)_{\perp}}{(F = 0 \to 0)_{\parallel}} = \frac{\frac{1}{4}\beta^2}{\frac{1}{4}\beta^2} \quad . \tag{3}$$

The curves in Figs. 23 and 24 are integrated numerically and are found to agree with each other. They yield

$$\left(\frac{\beta}{\alpha}\right)_{\text{expt.}} = .84 \pm .05 \, .$$

The estimated error arises primarily from the uncertainty in the base-line shift due to the background and slow temperature drifts in the tuning etalons that select the frequency of the laser.

The angular dependence of the $F = 1 \to 1$ line should vary as

$$\alpha^2 \cos^2\theta + \beta^2 \sin^2\theta \, , \tag{4}$$

where θ is the angle between $\hat{\epsilon}$ and $\underline{E}$. The results are shown in Fig. 25. The solid line is the equation $a\cos^2\theta + b\sin^2\theta$ where $b/a = .81$.

Although, there is reasonably good agreement with $\beta/\alpha)_{\text{expt.}}$ the angular dependence measurement is not very reliable since the stressed quartz plate is slightly wedged and a rotation will shift the laser beam position in the cell. Hence, the lenses will collect light with

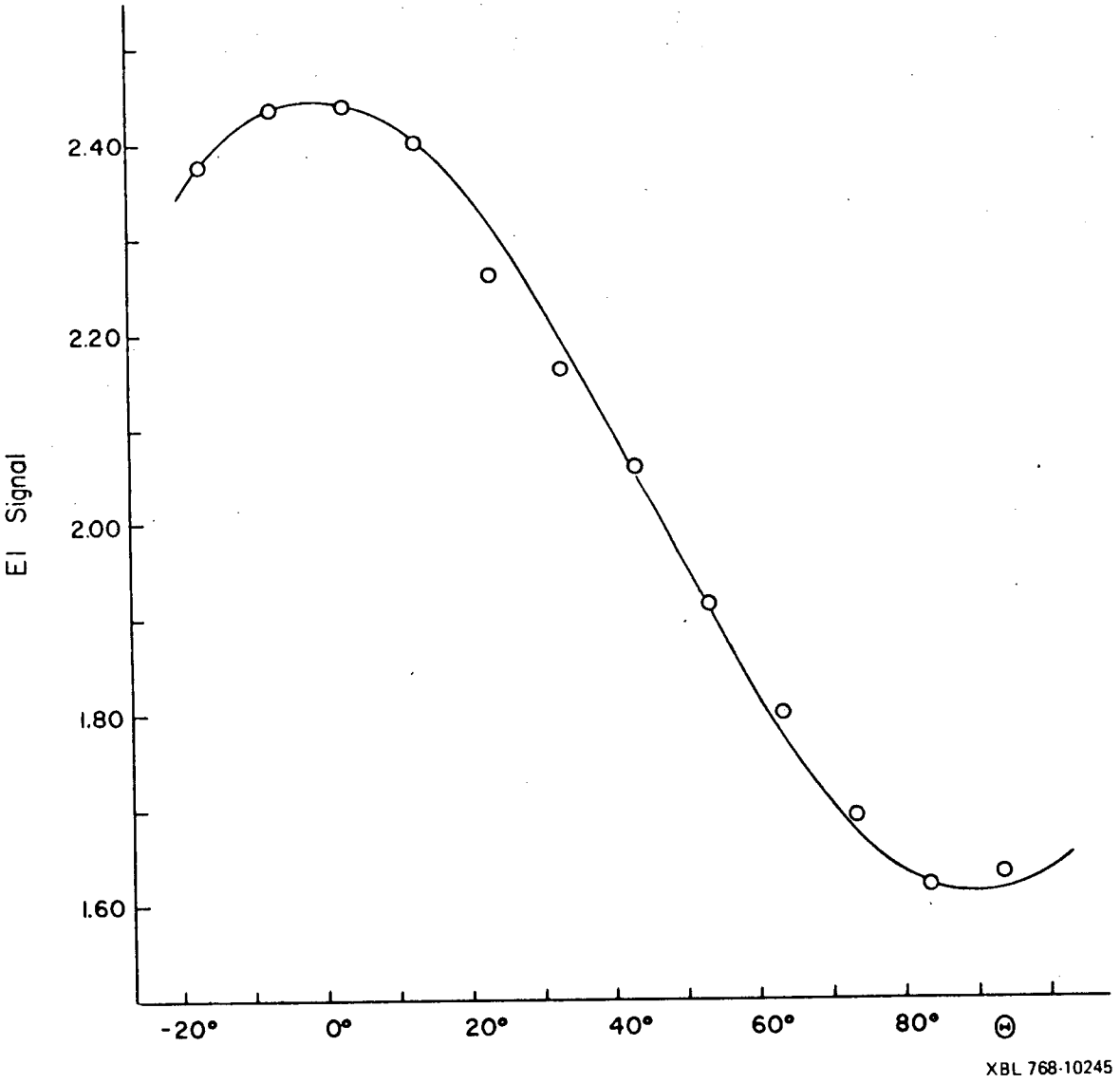

Fig. 25. Relative fluorescent signal vs. rotation angle θ between $\hat{\epsilon}$ and $\hat{E}$. The solid line is $a\cos^2\theta + b\sin^2\theta$ for a/b = .81.

different efficiencies.

The results of the induced E1 measurements are summarized in Table V with the predictions already given in Table III. These measurements provide an independent check on the radial integrals calculated by Neuffer. Since α and β are the sums of the products of two radial integrals, β/α should be approximately proportional to the fourth power of these integrals.

B. E1-M1 Asymmetry Results

The asymmetry data is analyzed according to the procedure given in part D, section III, and plotted as a function of 1/E in Fig. 26. The error bars are purely statistical "errors in the mean," and represent a 50% probability that the "true" value is within the range given. The dotted lines represent a least squares fit to the asymmetries for the different F→F' transitions. The 0→0 transition shows no asymmetry that scales as 1/E, and the ratio of the F = 1→1, $\hat{\epsilon} \parallel \underline{E}$, and the F = 0→1, $\hat{\epsilon} \perp \underline{E}$ asymmetries agrees with the experimentally measured valve of β/α. It is gratifying to note that the agreement is very good only if the 15% hfs correction to the M1 rate is included. Furthermore, all three lines have a common intercept, as expected. The results are summarized in Table VI along with calculated behavior already given in Table IV. The reason for the slight offset from zero has not been determined, but since all the other aspects of the data are consistent, we overlook this small peculiarity.

Table V.

Incident Light Polarization	Transition $6^2P_{1/2} \rightarrow 7^2P_{1/2}$ $F \rightarrow F'$	Theoretical Intensity	Calculated Relative Intensity Assuming E Large $\beta/\alpha_{theory} = .80$	Observed Relative Intensity (See Section V.)
$\hat{\varepsilon} \parallel E_o$	$1 \rightarrow 1$	$\frac{3}{4}\alpha^2 + \frac{1}{4}\mu^2$	3	3
	$0 \rightarrow 0$	$\alpha^2/4$	1	1
	$0 \rightarrow 1$	$\mu^2/4$	0	-
	$1 \rightarrow 0$	$\mu^2/4^2$	0	-
$\hat{\varepsilon} \perp E_o$	$1 \rightarrow 1$	$\frac{1}{2}\beta^2 + \frac{1}{2}\mu^2$	1.92	2.1
	$1 \rightarrow 0$	$\frac{1}{4}\beta^2 + \frac{1}{4}\mu^2$		
	$0 \rightarrow 0$	0	0	-
	$1 \rightarrow 0$	$\frac{1}{4}\beta^2 + \frac{1}{4}\mu^2$	.64	.70

Table VI.

Incident Light Polarization	Transition $6^2P_{1/2} \rightarrow 7^2P_{1/2}$ $F \rightarrow F'$	Theor. $7^2P_{1/2}$ Polarization	Theor. $7^2P_{1/2}$ Polarization for large E_o, assuming $\beta/\alpha_{exp.} = .84$	Observed Asymmetry
$\hat{\varepsilon} \parallel E_o$	$1 \rightarrow 1$	$\frac{4m\alpha}{3\alpha^2+2m^2}$	$P_{\parallel} = \frac{4}{3}\frac{m}{\alpha}$	$\Delta_{\parallel}$
	$0 \rightarrow 0$	0	0	0
$\hat{\varepsilon} \perp E_o$	$1 \rightarrow 1$	$-\frac{m\beta}{\beta^2+m^2}$	only partially resolved	
	$1 \rightarrow 0$	0		
	$0 \rightarrow 1$	$-\frac{2m'\beta}{\beta^2+m^2}$	$P_{\perp} = \frac{-2m'}{\beta} \simeq -2.07P_{\parallel}$	$\Delta_{\perp} \sim -2.12\Delta_{\parallel}$

$m' = 1.15\ m$ due to hfs correction

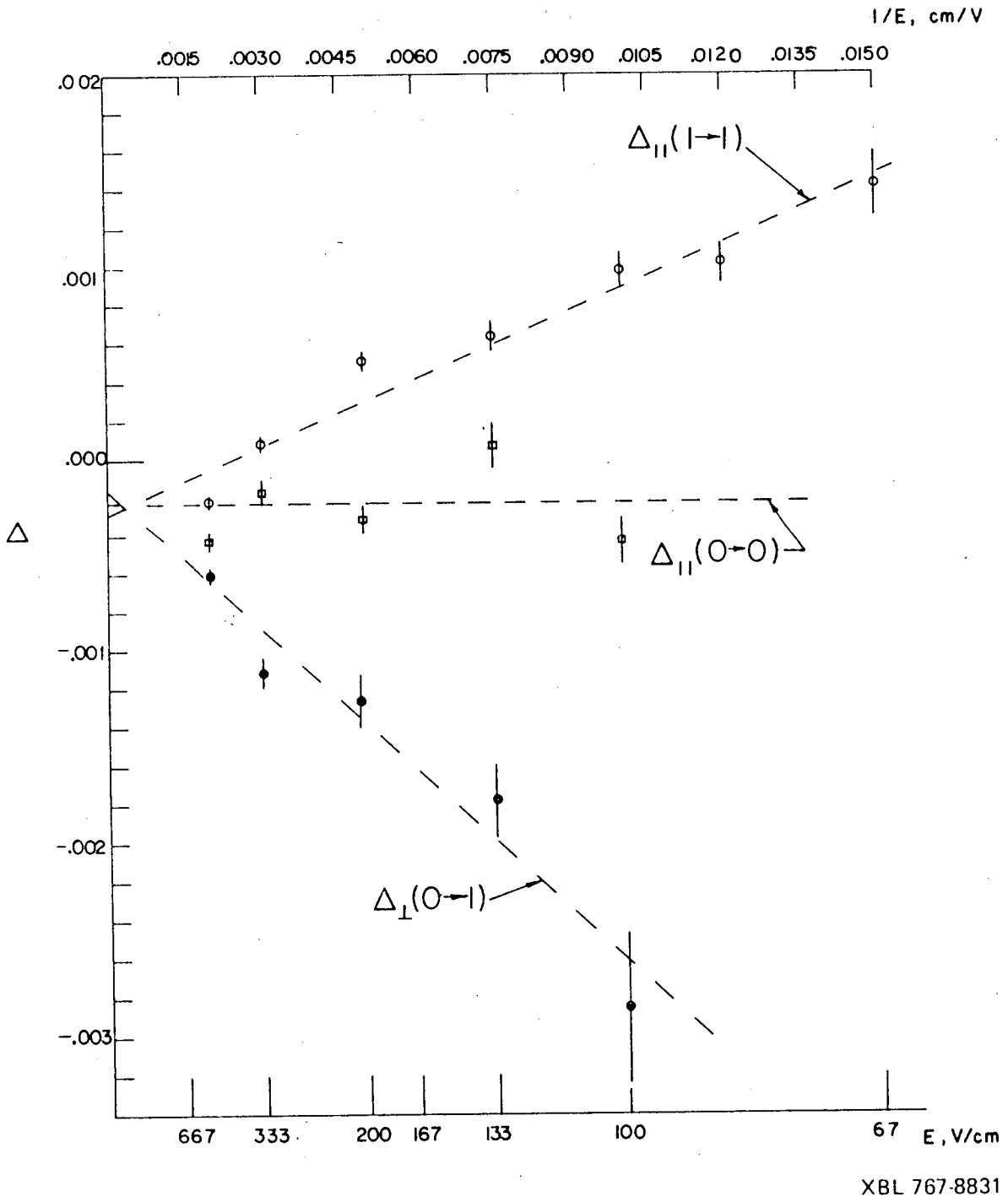

Fig. 26. Asymmetries, $\Delta(F\rightarrow F')$ for laser polarizations $\mathcal{E}$ both $\perp$ and $\parallel$ to $\mathcal{E}$ plotted as a function of 1/E. The dashed lines are least squares fits to the data points and the error bars represent probable errors in the means.

Since $P_{\|} \approx \frac{4}{3}\frac{m}{\alpha}$, knowledge of the slope of the line in Fig. 26 allows us to calculate both the sign and magnitude of the forbidden M1 matrix element, m. It remains to convert the asymmetry measurement $\Delta_{\|}$ into a value for the atomic polarization $P_{\|}$. (Only the F = 1→1, $\hat{\varepsilon} \| \hat{E}$ data will be used to determine m, while the other data can be regarded as a consistency check.) There are various mechanisms that dilute the atomic polarization so that the magnitude of $\Delta_{\|}$ is smaller than $P_{\|}$, and these corrections will now be considered.

1. Cascade Depolarization

The circular polarization of the 535 mm radiation is proportional to but smaller than the polarization of the $7^2P_{1/2}$ state. Also, only about half of the atoms in the $7^2S_{1/2}$ state decay to the $6P_{3/2}$ state, while the remainder return to the ground state. In this case, the polarization is lost, as shown in Fig. 27.

Define the populations of the $7^2P_{1/2}$ state as A, B, C for F = 1, m_F = 1,0,-1 and D for F = 0, m_F = 0. Similarly, the populations of the $7^2S_{1/2}$ states are labeled a,b,c for F = 1, m_F = 1,0,-1 and d for F = 0, m_F = 0. (see Fig. 28) From the Wigner-Eckart theorem, we can easily calculate the relative branching ratios for the m_F transitions. These ratios must be proportional to the square of Clebsch-Gordon coefficients, since the reduced matrix elements are all the same.

Suppose we have an initial polarization in the $7^2P_{1/2}$ state defined by

$$P_{int} = \frac{A-C}{A+B+C} . \qquad (5)$$

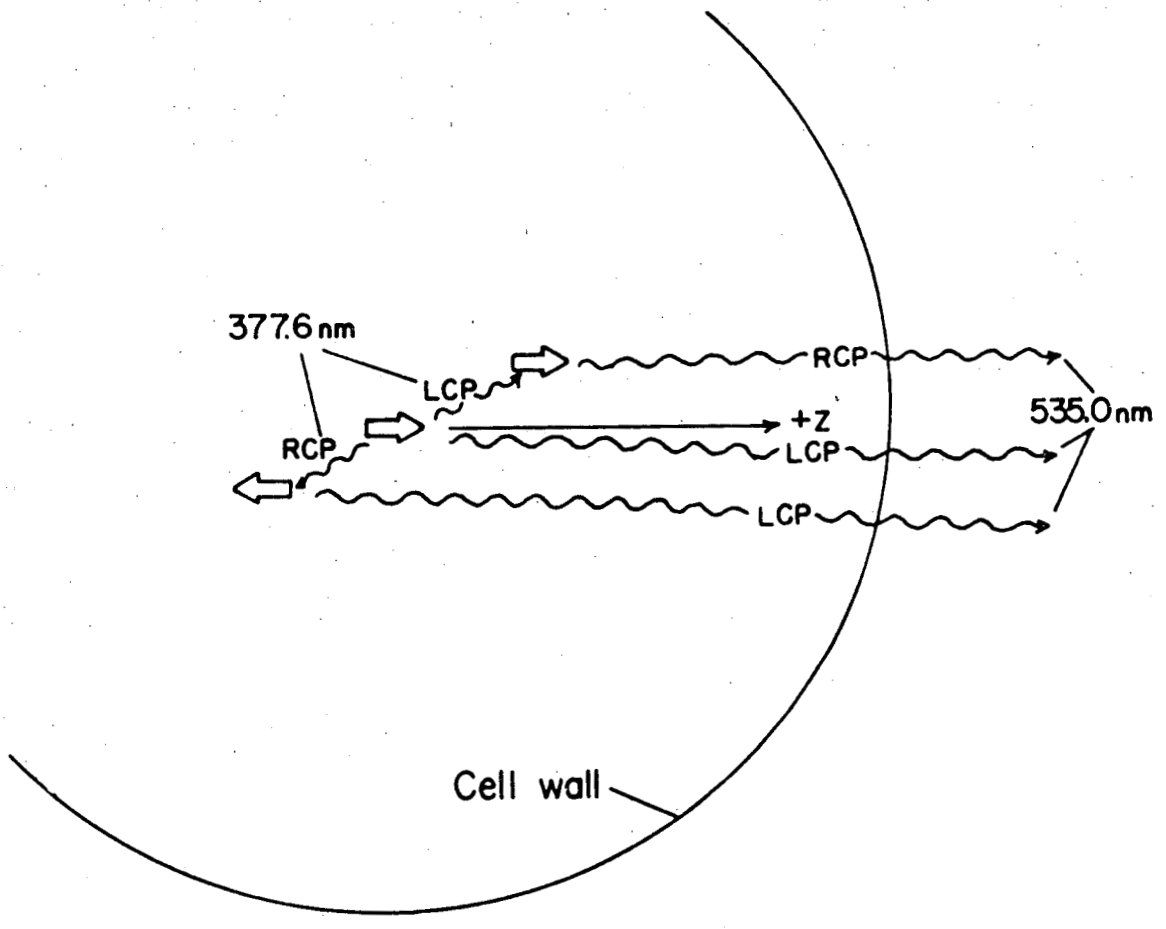

XBL 768-10238

Fig. 27. Suppose an Tl atom (1) is polarized in the $7S_{1/2}$ state along the +z-axis ($m_F = +1$). If it emits 535 nm light, the photon escapes carrying negative helicity and no polarization information is lost. If on the other hand, the atom decides to emit 338 nm light, the photon is quickly reabsorbed by a nearby ground state atom (2) Angular momentum is conserved so that the second atom is also polarized in the same direction. If the second atom emits 535 nm radiation along +z direction, the polarization will still be preserved. However, an equally likely possibility is for atom (1) to excite atom (3) which then gives off RCP 535 nm light along +z. Hence, any atom that decides to take the 378 nm road will give no polarization information.

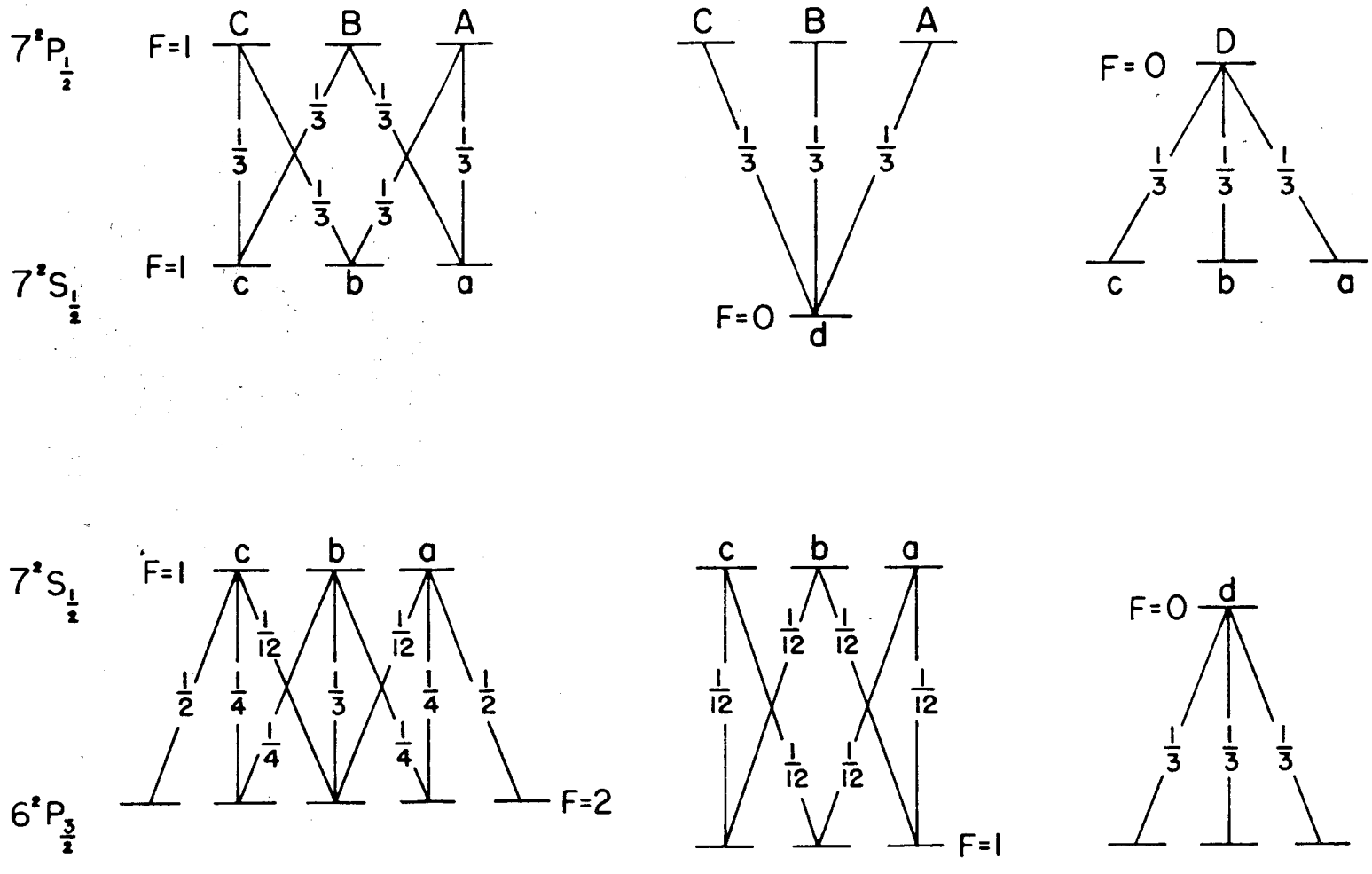

XBL 768-10231

Fig. 28. Branching ratios for transitions from the $7^2P_{1/2}$ and $7^3S_{1/2}$ states.

Then the $7^2S_{1/2}$ state polarization will be

$$P = \frac{a-c}{a+b+c+d} , \tag{6}$$

where

$$a = \frac{1}{3}(A+B) , \qquad b = \frac{1}{3}(A+C)$$

$$c = \frac{1}{3}(B+C) , \qquad d = \frac{1}{3}(A+B+C) , \tag{7}$$

and

$$A + B + C = 1, \qquad a + b + c + d = 1 \tag{8}$$

From the $7S_{1/2}$ states, we use Fig. 28 and add up all the RCP, LCP and linear polarized light the goes to the $6^2P_{3/2}$ state:

$$RCP = \frac{1}{6}a + \frac{1}{3}b + \frac{1}{2}c + \frac{1}{3}d$$

$$LCP = \frac{1}{2}a + \frac{1}{3}b + \frac{1}{6}c + \frac{1}{3}d \tag{9}$$

$$LIN = \frac{1}{3}a + \frac{1}{3}b + \frac{1}{3}c + \frac{1}{3}d$$

The dipole angular distribution of the 535 nm radiation is

$$\sin^2\theta \text{ for } \Delta m = 0 \text{ transitions}$$

$$\frac{1}{2}(1 + \cos^2\theta) \text{ for } \Delta m = \pm 1 \text{ transitions,} \tag{10}$$

where θ is the azimuthal angle from the z-axis. For detectors of infinitely small solid angle, no linearly polarized light will be seen, and the asymmetry between left and right circularly polarized light is

$$\Delta = \frac{RCP - LCP}{RCP + LCP}$$

$$= \frac{(\frac{1}{6}a + \frac{1}{3}b + \frac{1}{2}c + \frac{1}{3}d) - (\frac{1}{2}a + \frac{1}{3}b + \frac{1}{6}c + \frac{1}{3}d)}{(\frac{1}{6}a + \frac{1}{3}b + \frac{1}{2}c + \frac{1}{3}d) + (\frac{1}{2}a + \frac{1}{3}b + \frac{1}{6}c + \frac{1}{3}d)}$$

$$= \frac{-\frac{1}{3}(A-C)}{2(A+B+C)}$$

$$= -\frac{1}{6} P_{int} . \qquad (11)$$

where Eqs. (5) thru (9) were used. The correction for the finite solid angle of the detectors, assuming an f-1 lens geometry, leads to

$$\Delta = -\frac{1}{6.333} P_{int} .$$

Finally, the branching ratio from $7^2S_{1/2}$ to $6^2P_{3/2}$ or $6^2P_{1/2}$ levels must be included. We use the value measured by Gallagher and Lurio in a thallium atomic beam (Gal, 64)

	A-coeff.	Relative Intensity
$6P_{3/2}$	$7.05 \pm .32 \times 10^7 sec^{-1}$	.53
$6P_{1/2}$	$6.25 \pm .35 \times 10^7 sec^{-1}$	.47

Thus,

$$\Delta = -.0837 P_{int} \qquad (13)$$

2. Resonance Trapping of 535 nm Radiation

If the 535 nm light becomes partially trapped, the detected asymmetry Δ will decrease still further. We will now make a crude estimate of the degree of resonance trapping that can be expected in

typical operating conditions. The absorption coefficient μ, defined by

$$I = I_o e^{-\mu \ell} , \tag{14}$$

where I = intensity of the light after beginning with intensity I_0 and traversing a distance ℓ, is given by

$$\mu = \frac{\lambda^2}{8\pi} \frac{A}{\Delta\nu} n , \tag{15}$$

where $A = 7.05 \pm .32 \times 10^{-7}$ sec^{-1}, $\Delta\nu = 10^9$ Hz, $\lambda = 535$ nm and n is the density of the $6^2P_{3/2}$ state. The $6^2P_{3/2}$ density is related to the total density by a simple Boltzmann factor

$$n(P_{3/2}) = n(P_{1/2}) \times 2 \times e^{-\Delta E/kT_c} \tag{16}$$

where ΔE is the $6^2P_{3/2} - 6^2P_{1/2}$ fine structure splitting and T_c is the cell temperature. $n(P_{1/2}) \sim n_{tot}$ can be calculated from an empirical vapor pressure formula

$$\ln n_{tot.} = 54.3 - \frac{19.4}{T_{3,s}} , \tag{17}$$

where $T_{3,s}$ is the stem temperature of the cell in $°K/10^3$. The formula is fit to the vapor pressure data given by Nesmayanov (Nes, 63) and the perfect gas law, p = nkT. Figure 29 shows a plot of $e^{-\mu \ell}$ for various values of cell temperatures. Although the stem temperature is kept 3mV = 75°C less than the cell temperature, the difference in temperatures is not as great since the thermocouple that measures the stem temperature is not in good thermal contact with the stem. Therefore,

we assume an effective stem temperature that is 25°C less than the cell temperature. The length ℓ is the radius of the cell.

We have also measured the asymmetry of the F = 1→1 and F = 0→0 $\hat{\epsilon} \parallel \underline{E}$ transitions at 200 v/cm for various cell-stem temperatures above our operating temperature of ~ 950°K. We then take the difference, $\Delta_{1\to1} - \Delta_{0\to0}$, to eliminate the asymmetry due to our apparatus. The data is also shown in Fig. 29, and although the statistics are not very good, there is good evidence that there is very little resonance trapping and subsequent depolarization at our usual operating thallium densities. The change in density between T_c = 946°K and T_c = 1043°K is 2.9×10^{14} atoms/cm^3 to 2.1×10^{15} atoms/cm^3. (Strictly speaking, $e^{-\mu\ell}$ does not describe the depolarization due to resonance trapping, but the crudeness of the data does not warrant a more careful treatment.)

3. Collisional Depolarization

When the thallium atoms are in the excited $7^2P_{1/2}$ and $7^2S_{1/2}$ states, collisions with other atoms are possible and a subsequent depolarization will occur. A simple estimate can be made by comparing the average time the atom spends in these excited states and the mean time between atom-atom collisions. The lifetimes of the relavant excited states are

$$7^2S_{1/2} \quad .75\times10^{-8} \text{ sec}$$
$$7^2P_{1/2} \quad .58\times10^{-7} \text{ sec} .$$

The mean time between collisions can be roughly guessed as $\tau = \ell/\bar{v}$, where

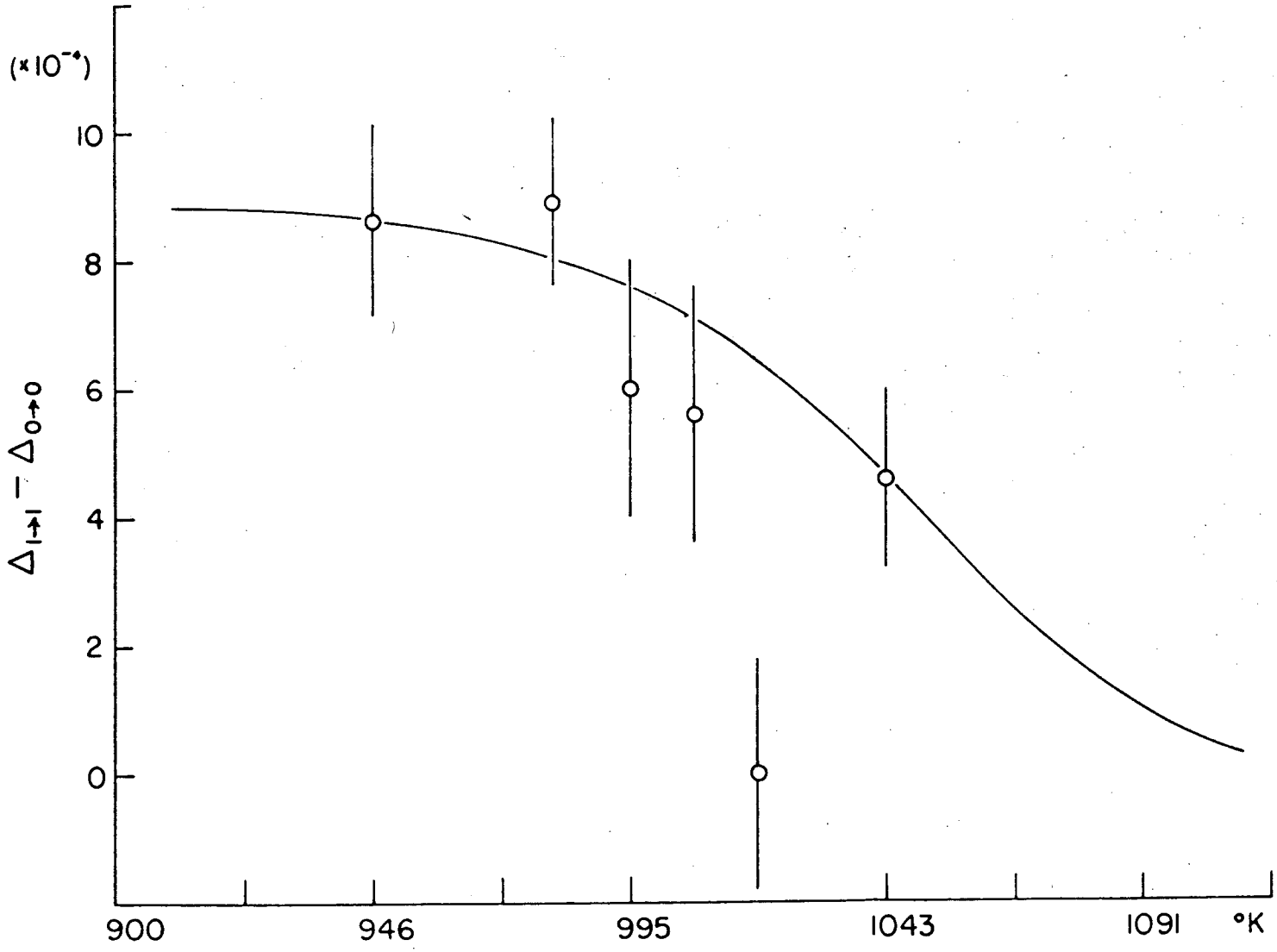

Fig. 29. The asymmetry $\Delta_{1\to1} - \Delta_{0\to0}$ as a function of the thallium cell temperature.

$$\ell = \text{mean free path} = \frac{1}{n\sigma} \text{ , and}$$

$$\bar{v} = \text{rms velocity} = \sqrt{\frac{3kT}{M}} \approx 3.4\times10^{4} \text{ cm/sec .}$$

Take cross-section σ to be the geometric cross-section, $\sigma \approx 30\times10^{-16}$ cm^2. Then $\ell \approx 1$ cm and $\tau \approx .3\times10^{-4}$ sec. Since the mean time between collisions is approximately 500 times longer than the lifetimes of the excited states, there is virtually no chance for collisional depolarization to occur.

4. Instrumental Depolarization

The most likely source of instrumental depolarization should come from the Polaroid circular polarizers. The HNCF37 left circular polarizers used have characteristics shown in Fig. 30., provided by Polaroid Corporation. These very inexpensive plastic polarizers are ideally suited for work at 535 nm and the extinction ratio is far better than we need for the present level of accuracy. However, the quarter-wave plate part of the polarizer necessarily has a secant θ dependence for light that enters at an angle θ from the normal of the filter. In our experiment, θ is kept small (cf Fig. 6) since the laser beam is placed at the focal spot of the lens. In fact, the interference filters can only accept 535 nm light if it is within ~ 5° of normal incidence. Thus, the secant error is constrained to be less than a .3% correction.

Other, unforseen effects can be examined directly by using the techniques given by Bouchiat and Pottier (Bou, 76a). They calibrated their apparatus by also measuring a known asymmetry that is created

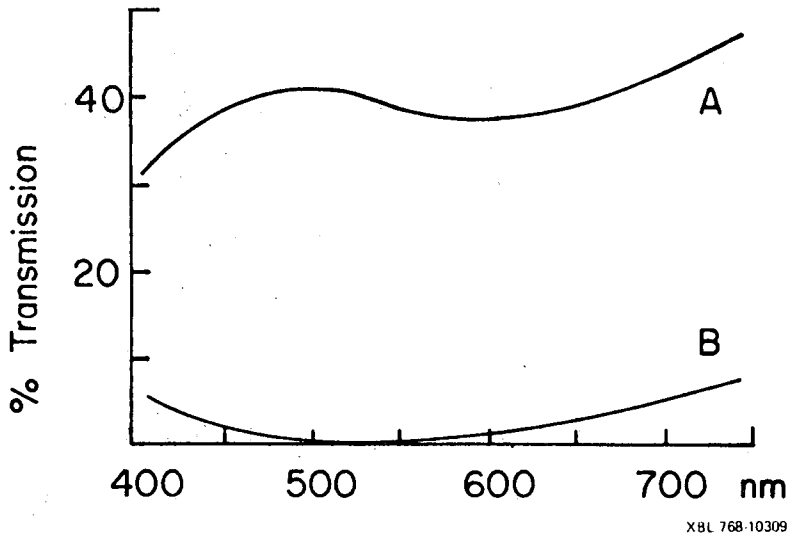

Fig. 30. Polaroid HNCF37 left circular polarizer. Curve A gives the transmission characteristics of unpolarized light at normal incidence, and curve B gives the rejection characteristics of right circularly polarized light.

when the incident laser light is circularly polarized. This creates an atomic polarization along the direction of laser, and a d.c. magnetic field parallel to the static electric-field is then used to rotate the atomic state polarization in line with the phototubes. This is actually the Hanle-effect, a well-known optical pumping technique. (Hap, 72) This technique has not yet been used, but will be tried in the near future.

5. The Experimental Value for the M1 Matrix Element

We will use Eq. (13) of this section to calculate the M1 matrix element between the $6^2P_{1/2}$ and $7^2P_{1/2}$ states of thallium. The values of α and β are given in Eq. (10) of Section II. The least-squares fit to the data in Fig. 26 give the following values for Δ:

	Slope	Intercept
$\Delta(0\rightarrow1)$	$-.147\pm.025$	$-1.58\times10^{-4}\pm2.4\times10^{-4}$
$\Delta(1\rightarrow1)$	$+.0693\pm.0072$	$-2.81\times10^{-4}\pm1.12\times10^{-4}$
$\Delta(0\rightarrow0)$	$-.00177\pm.017$	$-2.21\times10^{-4}\pm2.01\times10^{-4}$

Care must be exercised in calculating the sign of $\langle\mu\rangle$. We must remember that left circular polarizers are used, the north channel is looking in the negative $\hat{z}$-direction, and the E-field is negative when the top plate has a positive voltage on it. When all of these effects are included, we get

$$\langle\mu\rangle_{expt} = -\ (2.11\pm0.30)\times10^{-5}\ \frac{|e|\hbar}{2mc}$$

in reasonable agreement with Neuffer's calculation (see Table I) of

$$\langle \mu \rangle_{\text{theo.}} = - 1.8\times10^{-5} \frac{|e|\hbar}{2mc}$$

The error in $\langle \mu \rangle$ rises from approximately equal uncertainties in the theory and in the slopes of Fig. 26. The result can also be expressed as an A-coefficient

$$A = \frac{4}{3} \frac{\omega^3}{\hbar c^3} |\langle \mu \rangle|^2 = 1.4\times10^{-6} \text{ sec}^{-1} \simeq 8 \text{ day lifetime} ,$$

or and oscillator strength

$$f = \frac{\lambda}{8\pi^2 c a_o} A = 1.8\times10^{-15} ,$$

where λ, ω are the wave length and frequency of the transition, and a_o is the Bohr radius.

To the best of our knowledge, this is the smallest atomic oscillator strength ever measured.

V. BACKGROUND

We previously stated that a large non-resonant background prevents us from measuring the M1 rate by scanning the laser frequency through the $6^2P_{1/2} - 7^2P_{1/2}$ transition. From the interference method we use to measure the M1 matrix element, we estimate that the number of photons due to the M1 transition we would detect at zero electric field would be approximately 1/300 of the total number of photons detected. Indeed much of our experimental work has been directed towards understanding and reducing the background.

A. Backgrounds Not Involving Thallium

There are actually many components to our background, but many portions are not significant. For example, dark counts from the 8850 phototubes and amplifier noise contribute in negligible amounts. Gating of the phototube output to be conincident with the microsecond laser pulse eliminates counts from blackbody radiation and extensive RF filtering eliminates noise from the laser.

At the thallium densities we normally operate, laser light scattering or fluorescence from the quartz cell creates about 15-20% of the total unwanted counts. This component of the background is measured by condensing the thallium vapor in the stem while keeping the main oven at 950°K and measuring the signal from the phototubes coincident with the laser pulses. Apparently, the intense UV light from the laser creates transient color centers in the Suprasil windows

and the scattering and especially fluorescence from these color centers in a region around 535 nm can pass through the interference filters and be detected by the phototube. (Bro, 71), (Hol, 69) The light scattering increases when the cell is allowed to cool to room temperature, presumably due to a longer lifetime for the color centers at lower temperatures.

Also, small fraction of the scattered light background is due to 293 nm light scattering into the 535 nm interference filter and causing the glass substrate of the filter to fluoresce. (Also see part D of this section for a discussion of Raleigh scattering)

The remaining sources of background require the presence of laser light and cell and stem temperatures necessary to produce an appreciable density of thallium. Our efforts to produce an ultra-clean environment for the thallium (see the description of the cell and oven in part B of section III) indicate that the background is reduced by using a cleaner cell, but after a certain level of cleanliness, nothing is gained. ("Cleanliness" is measured by the pressure measured at the vac-ion pump when the cell is hot.) Thus, we are lead to believe that the background is generated in the cell by the action of the 293 nm laser light on thallium atoms and/or molecules involving thallium. Our attempts to reduce the background have lead us to experiment with a variety of cells. The earliest versions were sealed off cells, made from commercial grade quartz and filled with thallium by standard vacuum distillation techniques. (Gib, 70) The sections of the quartz in contact with macroscopic amounts of thallium (for example, the bottom

of the stem) appeared slightly frosted by the thallium. When the quartz was replaced with Suprasil quartz, the frosting decreased and we surmise that the chemical reactions of the thallium and quartz at elevated temperatures were reduced by using higher purity quartz. Later cells, all made from Suprasil quartz, included a valve system (see Fig. 17) that enabled us to pump away contaminants freed from the walls of the cell by the high temperatures. Finally, a tantalum envelope was placed in the quartz stem so that the bulk of the thallium was in contact with the tantalum and not the quartz. A molybdenum stem, connected directly to the quartz via a "Housekeeper" seal (copied from the "Moly Cup" design, manufactured by Bomco Inc.) was also tried, but with unsatisfactory results. (See the discussion on the electric field dependent background.) The eventual cell design also calls for a small amount of getter material placed in the cell.

Crude measurements indicate that the eventual background level is approximately 50-100 times lower than the level of the first sealed off cells.

B. Electric Field Dependent Background

A small fraction of the background is present only when an electric field is on. Figure 31 shows a plot of the field dependent background taken with the laser tuned away from the $6^2P_{1/2} - 7^2P_{1/2}$ line. The abscissa is the electric potential across 1 cm × 2 cm electrodes inside the cell separated by 1 cm, and the ordinate is the south channel background signal $S_- - S_o$ where S_- is the background with the field on and S_o is the field independent background. The

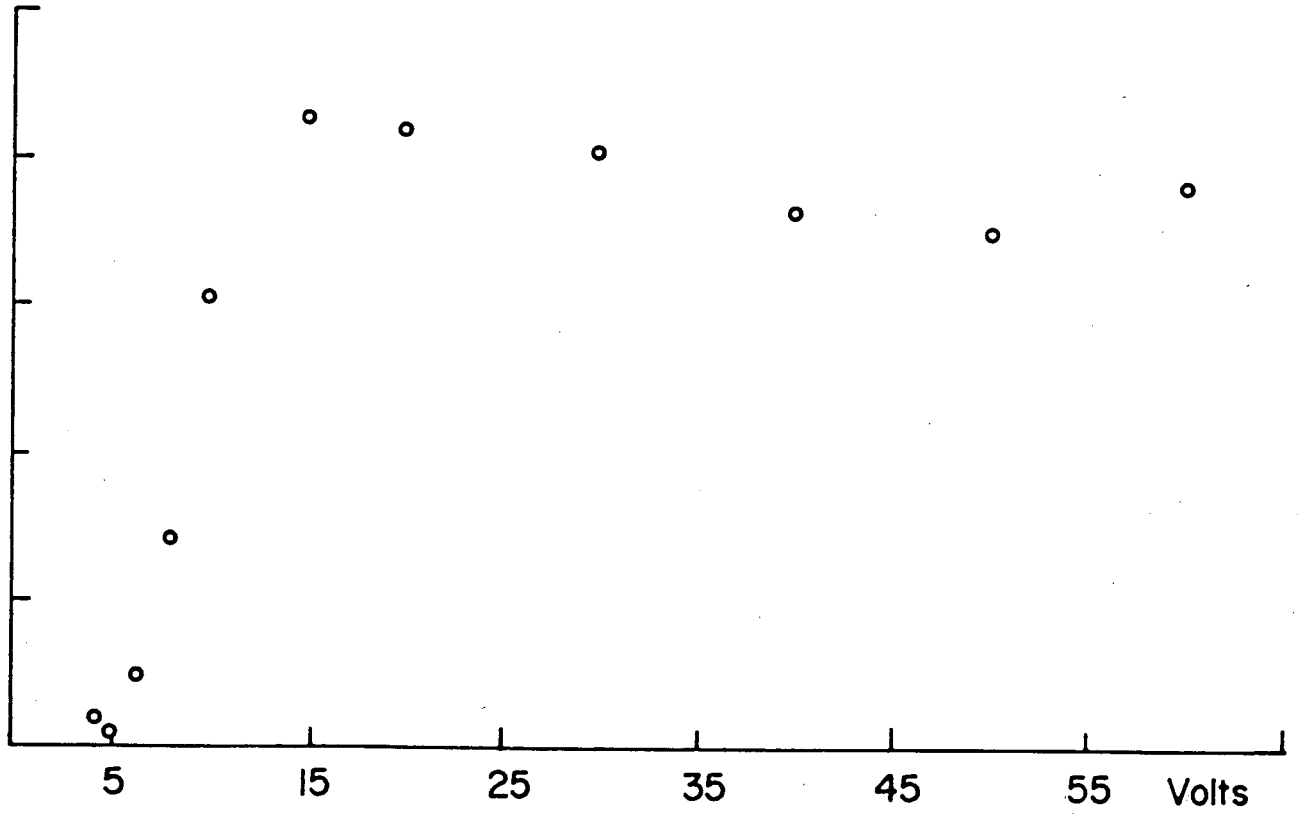

XBL 768-10230

Fig. 31. Field-dependent background plotted in arbitrary units vs. the electric field in volts/cm.

background exhibits a sharp threshold around 5 volts and rises to a relatively constant level at voltages of 15 volts or more. We believe that this behavior can be explained by the intense ultraviolet light of the laser ionizing thallium atoms in a two-photon ionization process (Zer, 64), (Kla, 72) or a single photon excitation of more loosely-bound molecules involving thallium. The electrons are then accelerated by the electric field and collisionally excite thallium atoms which then radiate 535 nm radiation. Indeed, the curve in Fig. 31 shows a remarkable similarity to typical graphs of cross-sections between slow electrons and atoms or molecules (Mot, 69).

We believe that the electric field-dependent background results from the ionization of molecules involving thallium. Cells which allowed the bulk of the thallium to touch the quartz had roughly an order of magnitude higher field-dependent background than cells with a tantalum liner. Moreover, the background level seemed to increase in proportion to the amount of time the cell was hot, indicating that some undesirable chemistry was happening. The cell with the molybdenum stem also showed a steady deterioration of the noise level, and after roughly 100 hours in which the cell and stem were hot, the ratio of the field-induced E1 rate to the off-resonance field-induced background at 50 volts/cm went from less than .05 to 1.2. The cells in which tantalum liners were used showed no appreciable time-dependent increase in this component of the background, and the primary background is a field independent component.

C. Electric Field Independent Background

A cell using a tantalum liner shows no appreciable increase in the field-dependent background as a function of experimental running time, and most of the background is from a field-independent component. This portion of the background remains the most difficult part to deal with, but before considering speculations as to the cause of the background, we review our present knowledge.

(1) The background appears to be the result of a non-resonant broadband absorption. The signal to background ratio measured when the laser is operating with 1 etalon (linewidth ~5 GHz) is approximately 2 times smaller than with the laser running with 2 etalons. (linewidth ~ 2.5 GHz) We have also made measurements at several laser frequencies, tens of thousands of GHz away from the $6^2P_{1/2} - 7^2P_{1/2}$ transition frequency. There is some frequency dependence to the background, but we see nothing resembling the 1.1 GHz absorption width of a thallium atomic line. (A continuous scan was not made since the wavelength at which the ADA crystal operates efficiently is a function of its temperature, and the crystal oven was not set up for temperature scanning.)

(2) The fluorescent radiation does not exhibit the broadband absorption features. By tilting the 535 nm interference filters with respect to the phototube axis, it is possible to look at wavelengths a few nanometers away from the atomic line wavelength. In Fig. 32 off-resonance data for various tilt angles of the interference filter is shown together with on-resonance data with the electric field-induced

signal at 133 volts/cm. At these high electric fields the background is less than 10% of the total signal. Thus, Fig. 32 allows us to conclude that the background fluorescence is the same frequency as the 535 nm atomic line, to within the ~ 1 nm resolution of the interference filter.

(3) The background signal scales linearly with the intensity of the laser light over an order of magnitude (see Fig. 33). Thus, non-linear effects that scale as the square of the laser power are not contributing to the background.

(4) The background varies approximately as the atomic thallium density to the 1.8 power over a factor of 10 change in the thallium density (see Fig. 34). The atomic density is measured by monitoring the field induced E1 rate at 58 volts/cm for stem and cell temperatures and comparing the on resonance signal S to the off-resonance background B. The quantity S-B is taken to be linearly proportional to the atomic density. The vapor pressure in the cell is allowed to stabilize between temperature changes by waiting for several minutes after the thermocouple readings reach their new values. However, the temperature dependence measurement of the background must be treated with caution. First of all, the stem and cell were never kept at temperatures over 950°K for more than a few hours and the less volatile impurities may not have been pumped out before the measurements were made. Secondly, earlier (and perhaps less careful) measurements of the temperature dependence indicate that the background is proportional to the thallium density to the 1.5 power, and the two sets of data are not consistent with each other.

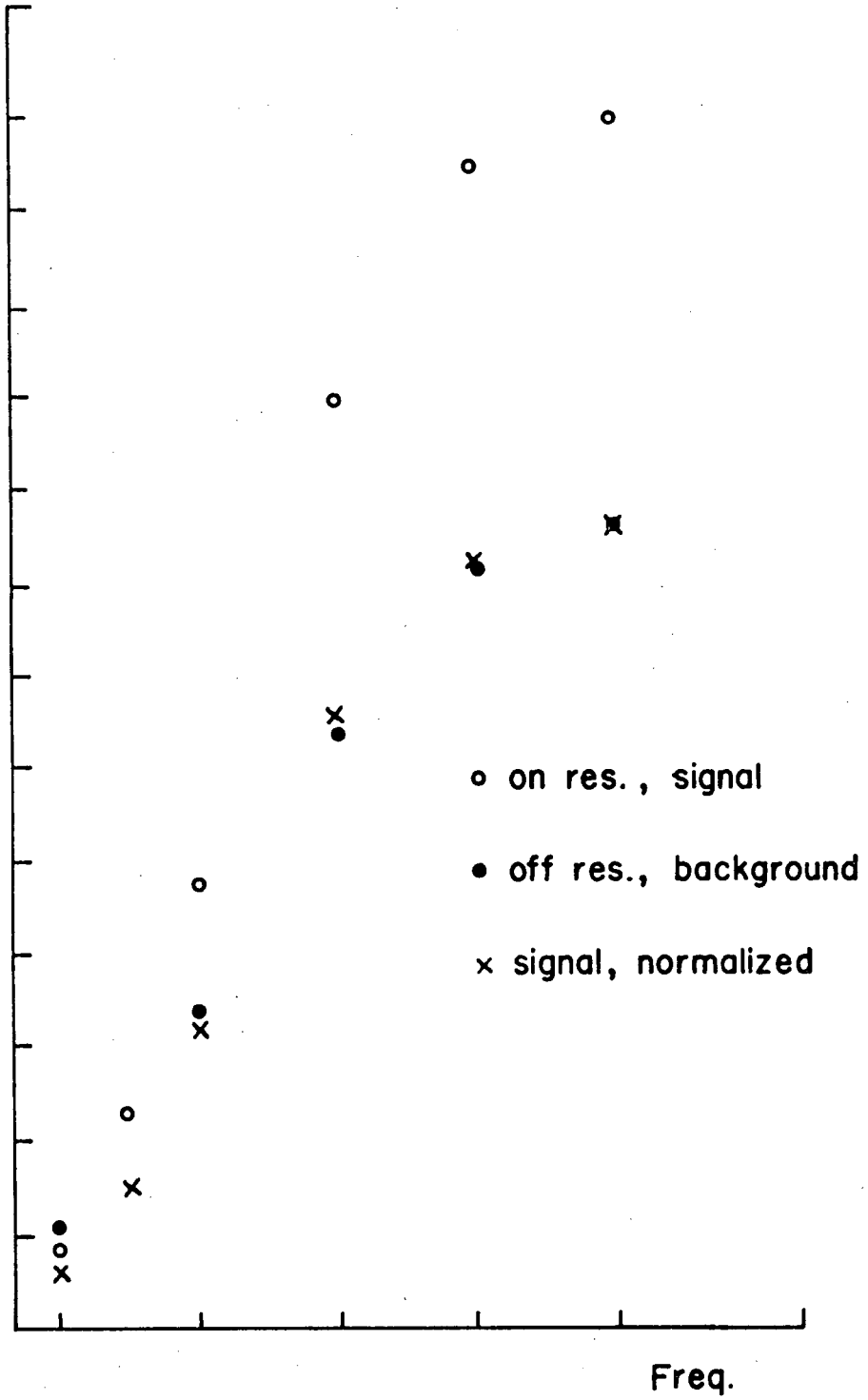

Fig. 32. Background counts (arb. units) vs. the tilt angle of the 535 nm interference filter.

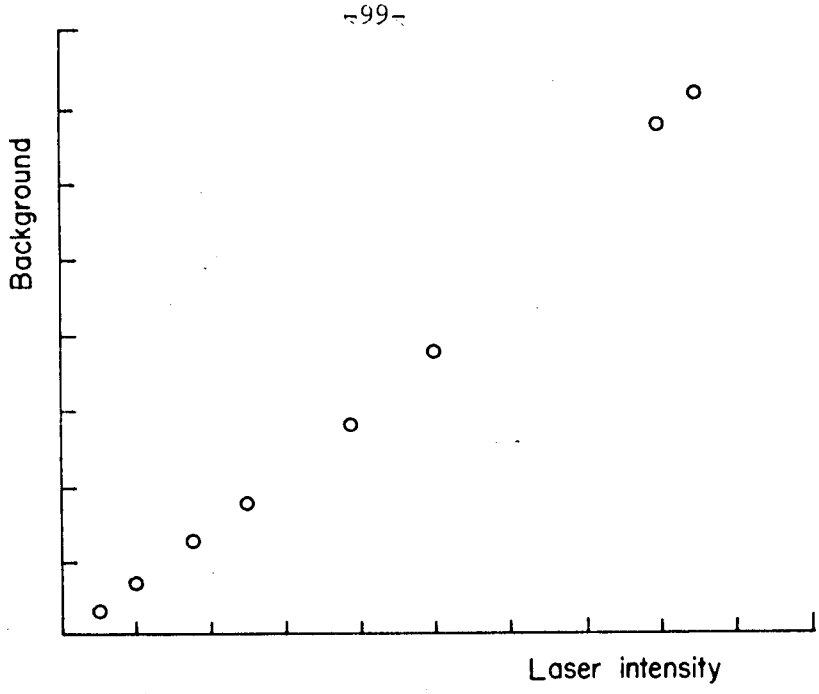

Fig. 33. Background signal vs. laser intensity in arbitrary units. At the highest laser intensities, the RCA 931 photodiode used to measure the laser power is beginning to saturate.

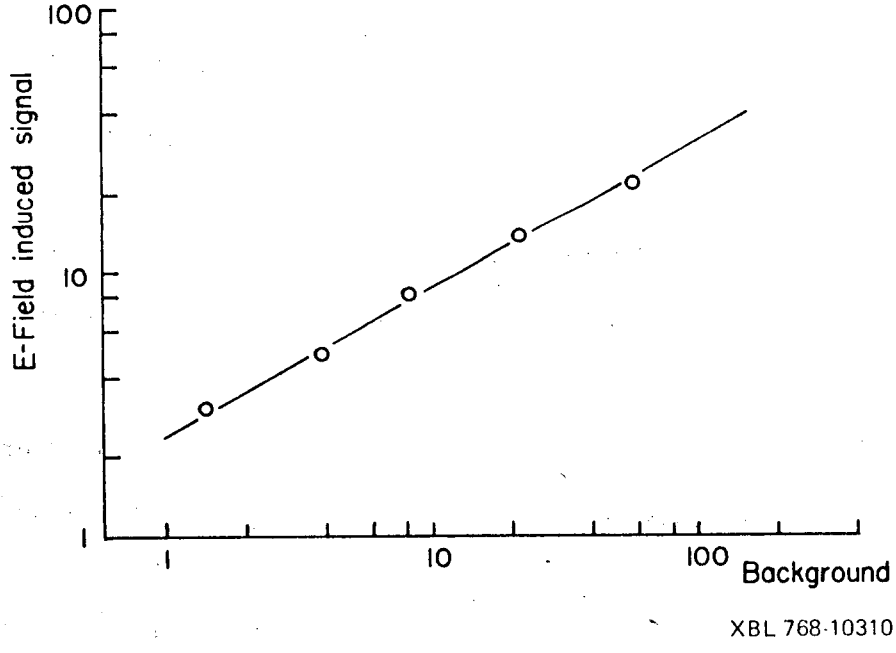

Fig. 34. E-Field induced signal vs. background for various thallium densities in the cell. The background varies as the E1 signal to the 1.8 power.

D. Possible Sources for the Non-Resonant, Zero-Field Background

1. Rayleigh Scattering

Nearby allowed electric dipole transitions have broad Lorentzian wings in their absorption curves that extend over the 292.7 nm M1 transition. If we assume that an atom first absorbs a 292.7 nm photon, is excited to a D or S state and then cascades down in the usual manner and emits a 535.0 nm photon, the process will not conserve energy. For example, if an atom absorbs a photon, is excited to the $7^2S_{1/2}$ state, and then returns to the ground state, the re-emitted photon cannot be a 377.6 nm photon. The correct treatment of the absorption process is not a 2-step first order process but a second order 1-step process. We then find that the proper description is Rayleigh scattering and the 292.7 nm light is elastically scattered. The narrowband interference filters should reduce this background to levels far below the M1 signal.

2. Raman Scattering from the $6^2P_{3/2}$ State

Raman scattering can occur from the $6^2P_{3/2}$ state to the $7^2P_{1/2}$ states via virtual intermediate S and D states (see Fig. 35). The formula for the total, cross-section for Raman scattering from unpolarized atoms in an initial state a to a final state b is

$$\sigma_{Ram} \approx r_o^2 m^2 \left(\frac{\omega'}{\omega}\right)\left(\frac{2}{3}\right)^2 \left| \sum_i \frac{\langle x \rangle_{bi} \langle x \rangle_{ia} \omega_{bi} \omega_{ia}}{E_i - E_a - h\omega} \right|^2 , \qquad (4)$$

where the sum is over the S and D-states. The classical electron radius r_o is defined by $r_o = e^2/mc^2$, and ω = laser frequency, and

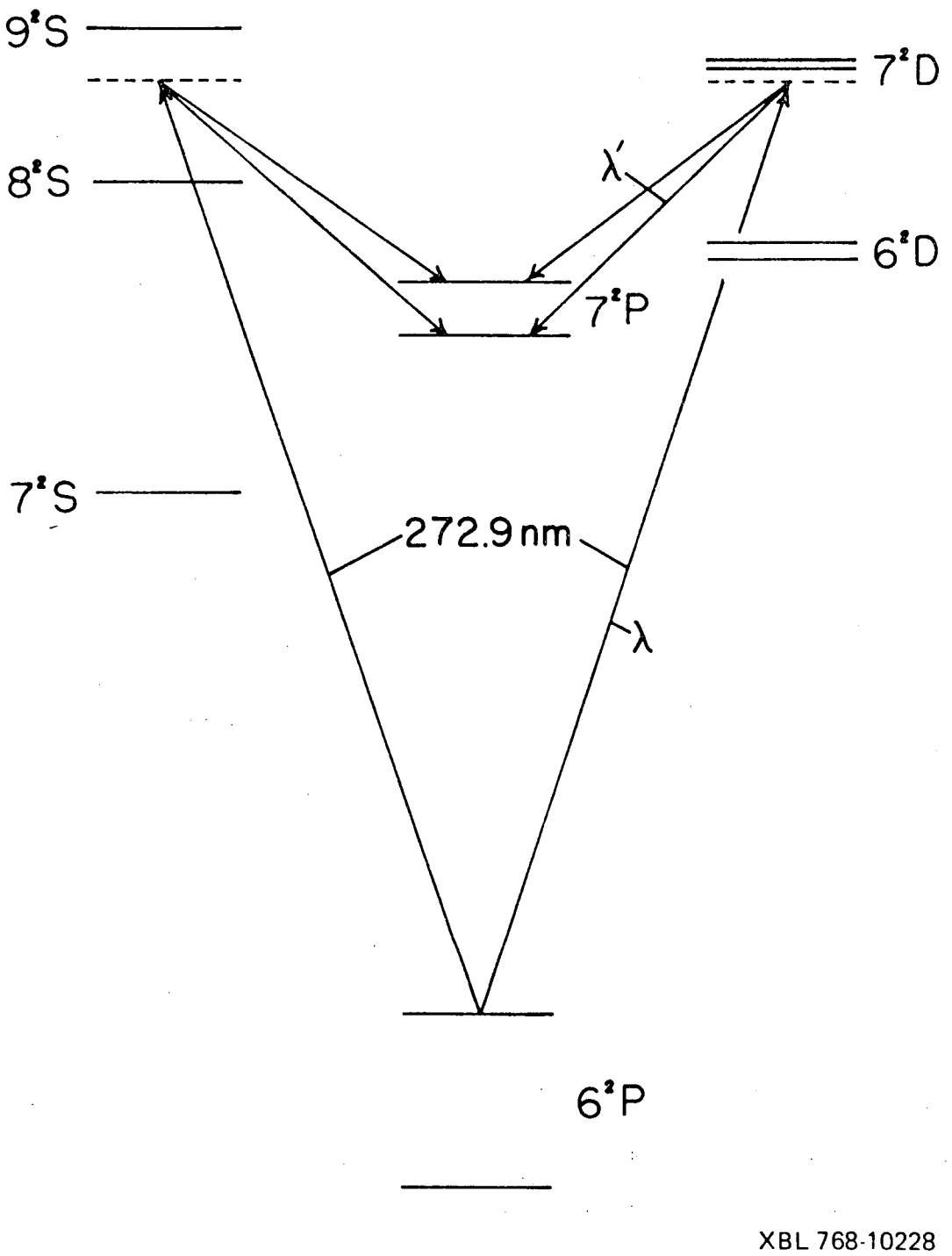

Fig. 35. The most significent Raman scattering transitions that contribute to the background.

ω' is the frequency of the Stoke's line $\omega' = \omega - \omega_{ab}$. If we consider the states giving the largest contribution to the background:

$$a = 6^2P_{3/2}\ , \quad b = 7^2P_{1/2}, \quad i = 7D_{3/2}\ ,$$

$$\sigma_{Ram} = 4.4\times10^{-25}\ cm^2\ .$$

This cross-section should be compared to the M1 cross-section defined by the transition probability

$$\omega_{M1} = \frac{4\pi^2}{hc}\ \frac{I(\omega)}{\Delta\omega}\ |\langle\mu\rangle|^2 = \frac{\sigma_{M1}I(\omega)}{\hbar\omega}\ . \tag{5}$$

The ratio of background due to Raman scattering to the M1 signal is then

$$\frac{\sigma_{Ram}}{\sigma_{M1}} \times \frac{n(6^2P_{3/2})}{n(6^2P_{1/2})} \approx .7\times10^{-4}\ , \tag{6}$$

where $n(6^2P_{1/2,3/2})$ are the atomic densities of the $6^2P_{1/2,3/2}$ states. Note that if there was significant Raman scattering from the ground state, the scattering background would be an order of magnitude larger than the M1 signal.

3. Collision Induced Transitions

Two colliding thallium atoms will induce dipole moments in each other and the electric field produced by one atom will mix states of opposite parity in the other atom. Hence, a collisionally induced E1 transition can occur between the $6^2P_{1/2}$ and $7^2P_{1/2}$ states of thallium. This background can be estimated by calculating the probability P(r)

of a transition of one atom from one photon as a function of the distance r between atoms, and the distribution n(r) of atoms that will exist at any given instant of time. Then the transition probability is proportional to $\int_0^\infty P(r)\, n(r) dr$. P(r) is calculated by finding an expression for the Van der Waals (induced dipole-dipole) attraction between two thallium atoms. Once we have the electric field of the induced dipole as a function of r, the treatment of part B, section II can be used to calculate P(r).

The difficulty in treating collision induced transitions lies in finding a suitable expression for the atomic distribution n(r). If there are no forces between the atoms, $n(r) = 4\pi r^2 \eta$, where η is the mean atomic density. However, the Van der Waals attraction will make the collisions "sticky" and n(r) will be larger for small values of r. Since P(r) is such a strong function of r, the collision-induced rate is a very sensitive function of n(r) and a reliable calculation would be very difficult to perform.

A problem related to sticky thallium-thallium collisions is that of thallium-noble gas collisions. (We would expect collisions between thallium and noble gases to be less sticky than collisions betweeen thallium and thallium.) Using the apparatus outlined in Fig. 36, we introduce small amounts of helium and neon into the cell. The 535.0 nm background is measured for different pressures of the noble gases and plotted in Fig. 37. We find that the background due to a pure thallium density of $\sim 2\times10^{13}$ atoms/cm^3 is equivalent to a thallium + neon background when the neon density is $\sim 8\times10^{14}$ atoms/cm^3.

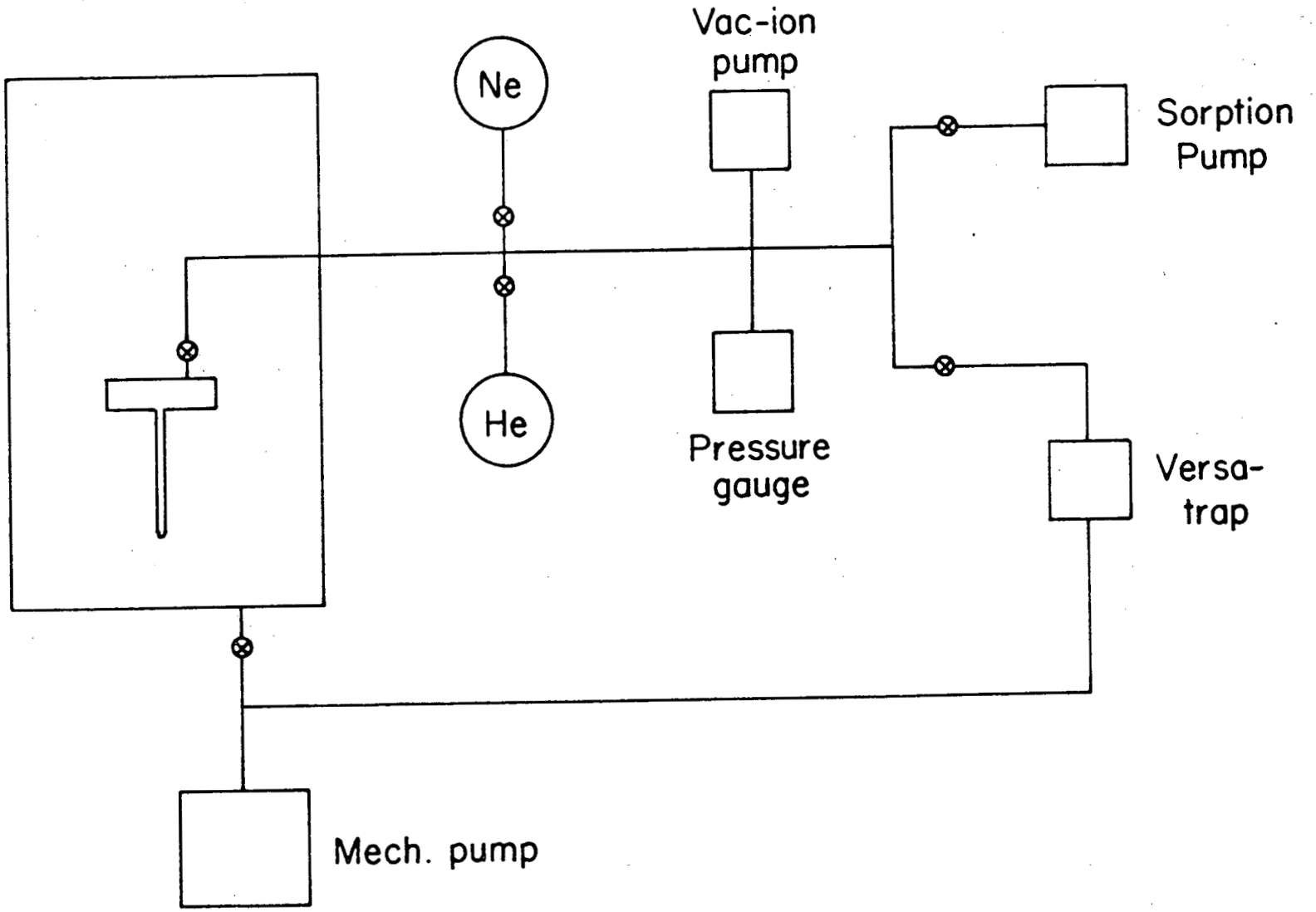

XBL 768-10227

Fig. 36. Schematic of the apparatus for the Tl-noble gas background measurements.

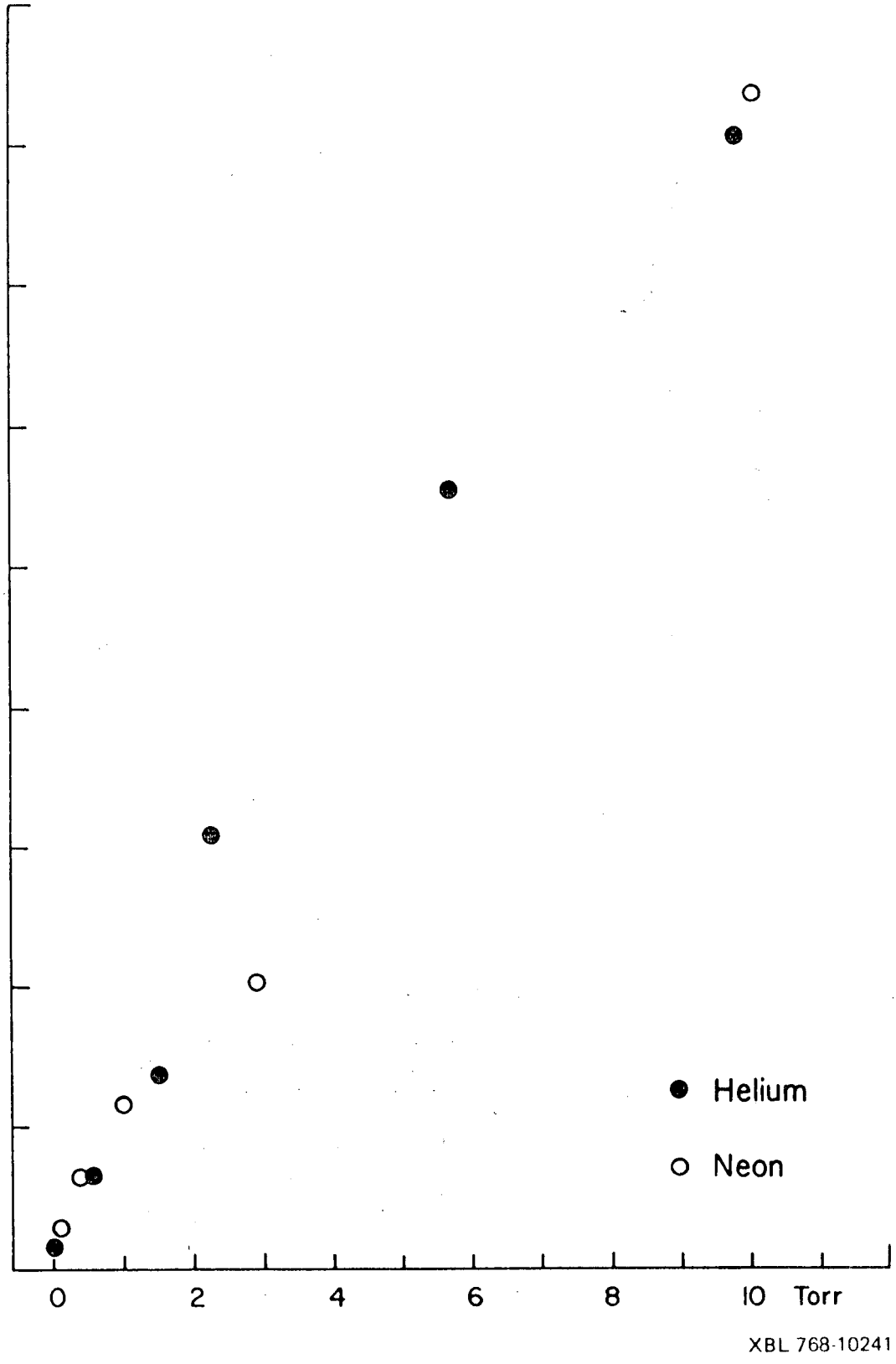

Fig. 37. Background due to sticky collisions and/or metastable molecules of thallium and the noble gases helium and neon for various noble gas pressures.

Other related work on metal vapor - rare gas collisions has been done by Penkin, et al. (Pen, 73) and Bouchiat, et al. (Bou, 69, 75d). Penkin and co-workers consider the broadening of resonance lines of Ga, In, Tl atoms due to collisions with atoms of inert gases, while Bouchiat, et al. measure the relaxation of polarized Rb atoms in encounters with rare gases.

4. Background from Thallium Dimers or Molecules of Thallium and Other Atomic Species

In addition to the two body collisions considered in the previous section thallium dimers or molecules of thallium and other atomic species may contribute to the background. These molecules may be stable or they may be metastable in the sense that they are very loosely bound and are broken up by thermal collisions with other atoms or with the cell walls. The quasi-molecules would be formed by either a 3-body collision, (necessary to conserve energy and momentum) or by a 2-body collision that includes a thallium atom in the excited $6^2P_{3/2}$ state. A senario for the background might be as follows: The molecule will absorb the laser radiation in a band around 292.7 nm, but once in the excited state, it will predissociate into its component atoms. (See Hertzberg (Her, 50) for an elementary discussion of predissociation.) One of the atoms might be an excited thallium atoms which then produces 535.0 nm radiation.

We have found no experiments that demonstrate the existence of stable thallium dimers. Hamada (Ham, 31) observed broadband emission spectra from thallium metal placed in a hollow cathode D.C. arc

discharge and attributes the band structure to thallium molecules of the form Tl_n. However, given the conditions of the discharge, the spectra is hard to interpret and could have been due to other molecular species. In any case, other researchers (e.g. Rec, 65) have not reported band structure due to thallium molecules, and since the level of background we see in our experiment is roughly 10 orders of magnitude less than a typical allowed-El transition, it would be very doubtful if it could be detected by conventional spectra-photographic techniques.

Many molecules (Tl_2O, TlH, etc.) involving thallium are known to exist at high temperatures, and it would be impossible to rule out possible contributions to the background due to these molecules.

Finally, we feel there is a strong possibility that metastable Van der Waals molecules (Tl_2) exist. The experiments of Bouchiat, et al. (Bou, 75d) provide strong evidence for Rb-rare gas Van der Waals molecules, and there seems to be no reason why there should not be similar weakly bound thallium dimers. Clearly, there is room for more experimental and theoretical work in this area.

VI. FUTURE EXPERIMENTS

Work is now under way to improve several features of the experiment in the hope that an asymmetry in the absorption of left and right circularly polarized light at $6^2P_{1/2} - 7^2P_{1/2}$ transition frequency due to weak neutral currents can be detected. Improved light collection and a multiple-pass geometry should give us more than an order of magnitude larger signal. Also a more sophisticated counting system will reduce instrumental asymmetries. Finally, we plan to increase the output power of the laser by an order of magnitude and simultaneously narrow the bandwidth of the laser to less than 1 GHz by cw laser injection into a flashlamp pumped forced oscillator. (The forced oscillator scheme has been reported using a variety of lasers for injectors. For example, see (Vre, 72), (Eri, 71), (Mag, 72), (Mae, 72).) Experiments are also under way to generate cw UV-light by means of intracavity doubling in a cw dye laser. We hope to improve the results of Gabel and Hercher, (Gab, 73) and generate a few milliwatts of continuous uv light at 293 nm in a single longitudinal mode with a bandwidth of approximately 10 MHz. A very narrow band dye laser might make an atomic beam experiment feasible; and consequently, we could expect a drastic reduction of the absorption width of the $6^2P_{1/2} - 7^2P_{1/2}$ line. Since the background is broadband, the signal-to-background ratio may improve by over two orders of magnitude.

ACKNOWLEDGEMENTS

I wish to thank my friend, adviser, and mentor, Eugene Commins for his active participation in every aspect of this work, from the design and construction of the apparatus to the most grubby chores of an experimental physicist,

Ralph Conti, who worked with Gene and me from the first exciting planning days of the experiment,

Dane Anderberg, and extremely able and ingenious glass blower,

Ed Lampo, who coordinated much of the data handling system,

Mel Magliocco, an exceptional machinist and instructor,

Dave Neuffer, who discussed with me much of the theoretical work associated with the experiment in his sporadic wakeful moments,

the many kind and helpful members of the Atomic Beams Group, especially Dick Marrus, Howard Shugart, Mike Prior, Mel Simmons, Phil Bucksbaum, Peter Mohr, John Clauser and Pat Yarnold,

Ken Tani and John Clarke, who introduced me to dye lasers,

Virginia Lam for typing the rough draft, and Alice Ramirez for typing the final draft, and

to my wife, Lily, whose support and devotion provided a welcome retreat from the laboratory.

This work was done under the auspices of the U.S. Energy Research and Developement Administration.

REFERENCES

(Adh, 73) R.S. Adhav, R.W. Wallace, IEEE J. of QE., QE9, 855 (1973).

(Aip, 63) Amer. Institute of Physics Handbook, ed. D.E. Gray, (McGraw-Hill, New York, 1963) p. 4-12.

(And, 67) E.M. Anderson, E.K. Anderson, V.F. Trusov, Optics and Spectroscopy, 22, 471 (1967).

(Bar, 34) R. Barrer, J. Chem. Soc., 378 (1934).

(Bar, 74) S.J. Barish, et al., Phys. Rev. Lett., 32, 800 (1974).

(Bar, 75) S.J. Barish, et al., Phys. Rev. Lett., 33, 448 (1974).

(Bar, 75b) B.C. Barish, et al., Phys. Rev. Lett., 34, 538 (1975).

(Bee, 72) D. Beer, J. Weber, Opt. Comm., 5, 307 (1972).

(Bei, 71) I.L. Beigman, U.I. Safronova, Sov. Phys. JETP, 33, 1102 (1971).

(Ben, 74) A. Benvenuti, et al., Phys. Rev. Lett., 32, 800 (1974).

(Ben, 76) A. Benvenuti, et al., Univ. of Wisconsin preprint E (11-1)-881-UW550 (1976).

(Ber, 71) V.B. Berestetskii, E.M. Lifshitz, L.P. Pitaevskii, trans. by J.B. Sykes, J.S. Bell, Relativistic Quantum Theory, Part 1 (Pergamon Press, New York; 1971).

(Ber, 74) J. Bernabeu, T.E.O. Ericson, C. Jarlskog, Phys. Lett., 50B, 467 (1974).

(Big, 74) I.I.Y. Bigi, J.D. Bjorken, Phys. Rev., D10, 3697 (1974).

(Bjo, 64) J.D. Bjorken, S.D. Drell, Relativistic Quantum Mechanics, (McGraw-Hill Co., New York, 1964), Chap. 4.

(Boe, 75) F. Boehm, A. Zehnder, Phys. Lett., 59B, 440 (1975).

(Bou, 69) C.C. Bouchiat, M.A. Bouchiat, L.C.L. Pottier, Phys. Rev., 181, 144 (1969).

(Bou, 74a) M.A. Bouchiat, C. Bouchiat, Phys. Lett., 40B, 111 (1974).

(Bou, 74b) M.A. Bouchiat, C. Bouchiat, J. de Physique, 35, 889 (1974).

(Bou, 75a) M.A. Bouchiat, C. Bouchiat, J. de Physique, 36, 493 (1975).

(Bou, 75b) M.A. Bouchiat, L. Pottier, J. de Physique Lett., 36, L-189 (1975).

(Bou, 75c) C. Bouchiat, Phys. Lett., 57B, 184 (1975).

(Bou, 75d) M.A. Bouchiat, J. Brossel, P. Mora, L. Pottier, J. Physique, 36, 1075 (1975).

(Bou, 76) M.A. Bouchiat, 5th International Conference on Atomic Physics (Plenum Press), 1976, (to be published).

(Bou, 76a) M.A. Bouchiat, L. Pottier, J. de Physique Lett., 37, (1976).

(Bou, 76b) M.A. Bouchiat, L. Pottier, Physics Letters, 62B, 327 (1976).

(Bra, 62) L.C. Bradley, N.S. Wall, Nuovo Cim. 25, 48 (1962).

(Bre, 40) G. Breit, E. Teller, Astrophys. J., 91, 215 (1940).

(Bro, 76) S.J. Brodsky, G. Karl, Comments on At. and Mole. Phys., to be published.

(Bru, 71) R. Brückner, J. of Non-Crystalline Solids, 5, 177 (1971).

(Bun, 72) J. Bunkenburg, Rev. Sci. Instr., 43, 1611 (1972).

(Car, 68) J. P. Carrico, et al., Phys. Rev., 174, 125 (1968).

(Che, 74) H. Cheng, C.Y. Lo, Phys. Lett., B52, 453 (1974).

(Chu, 76) S. Chu, E.D. Commins, R. Conti, Phys. Rev. Lett., to be published.

(Com, 71) E.D. Commins, Proc. of 2nd Int. Conf. on Atomic Physics, (Plenum Press, New York; 1971), p. 25.

(Cun, 74) D.C. Cundy, 17th International Conf. on High Energy Phys., (London, 1974) IV, 131.

(Dra, 71) G.W.F. Drake, Phys. Rev., A3, 908 (1971).

(Dra, 72) G.W.F. Drake, Phys. Rev., A5, 1979 (1972).

(Dre, 65) S.D. Drell, J.D. Sullivan, Phys. Lett., 19, 516 (1965).

(Dus, 62) S. Dushman, Sci. Foundations of Vacuum Tech., 2nd ed., (John Wiley, New York; 1962) sec. 7.7.

(Eri, 71) L.E. Erickson, A. Szabo, Appl. Phys. Lett., 18, 433 (1971).

(Fei, 71) G. Feinberg, J. Sucher, Phys. Rev. Lett., 26, 681 (1971).

(Fei, 74) G. Feinberg, M.Y. Chen, Phys. Rev. D, 10, 190 (1974). J. Bernabeu, T.E.O. Ericson, C. Jarlskog, Phys. Lett., 50B, 467 (1974).

(Fen, 72) S. Feneuille, E. Koenig, C.R. Acad. Sci. Ser B, 274, 46 (1972).

(Fis, 73) E. Fischbach, D. Tadic, Phys. Rep., 6C, 123 (1973).

(Flu, 76) A. Flusberg, T. Mossberg, S.R. Hartmann; Columbia Univ. preprint, 1976, to be published.

(For, 76) N. Fortson, Fifth International Conference on Atomic Physics, 1976 (Plenum Press), to be published.

(Gab, 73) C. Gabel, M. Hercher, J. Opt. Soc. Am., 63, 1321 (1973).

(Gal, 64) A. Gallagher, A. Lurio, Phys. Rev., 136, A87 (1964).

(Gar, 73) M. Gari, Phys. Rep., 6C, 317 (1973).

(Gib, 70) H.M. Gibbs, G.C. Churchill, T.R. Marshall, J.F. Papp, F.A. Franz, Phys. Rev. Lett., 25, 263 (1970).

(Gon, 65) J.H. Goncz, J. Appl. Phys., 36, 342 (1965).

(Gor, 74) V.G. Gorshkov, L.I. Labzovskii, JETP Lett., 19, 394 (1974).

(Gor, 75) V.G. Gorshkov, L.I. Labzovskii, JETP Lett., 21, 8 (1975).

(Gou, 70) H. Gould, Phys. Rev. Lett., 24, 1091 (1970).

(Ham, 31) H. Hamada, Philosophical Mag., 12, 50 (1931).

(Hap, 72) W. Happer, Rev. of Mod. Phys., 44, 169 (1972).

(Har, 69) G.E. Harrison, P.G.H. Sandars, S.J. Wright, Phys. Rev. Lett., 22, 1263 (1969).

(Has, 73) F.J. Hasert, et al., Phys. Let., 46B, 138 (1973).

(Has, 75) F.J. Hasert, et al., Proc. Paris Colloquium on Neutrino Physics, C.N.R.S., Paris, p. 257 (1975).

(Hen, 76) E.M. Henley, L. Wilets, U. of Washington preprint RLO-1388-713, (1976).

(Her, 50) G. Herzberg, Spectra of Diatomic Molecules, 2nd ed., (Van Nostramd, Princeton; 1950) p. 405.

(Hil, 74) O. Hildebrand, Opt. Comm., 10, 327 (1974).

(Hin, 76) E.A. Hinds, C.E. Loving, P.G.H. Sandars, Phys. Lett., 62B, 97 (1976).

(Hol. 69) J.F. Holzrichter, J.L. Emmett, J. of Appl. Phys., 40, 159 (1969).

(Hol, 70) J.F. Holzrichter, M.S. and A.L. Schawlow, Annals of the New York Academy of Sci., 168, 703 (1970).

(Hug, 76) V. Hughes, private communication, 1976.

(Ipp, 71) E.P. Ippen, C.V. Shank, IEEE J. of QE., QE7, 178 (1971).

(Jar, 74) C. Jarlskog, 17th Intern. Conf. on High Energy Phys., (London), 1974.

(Jet, 74) J. Jethwa, F.P. Schäfer, Appl. Phys., 4, 299 (1974).

(Joh, 74) W.R. Johnson, C. Lin, Phys. Rev., A9, 1486 (1974).

(Kay, 74) B. Kayser, G.T. Garrey, E. Fischback, S.P. Rosen, Phys. Lett., B52, 385 (1974).

(Khr, 74) I.B. Khriplovich, JETP Lett., 20, 315 (1974).

(Khr, 76) I.B. Khriplovich, Sov. J. Nucl. Phys., 21, 538 (1976).

(Kin, 74) R.L. Kingsley, F. Wilezeck, A. Zee, Phys. Rev., D10, 2216 (1974).

(Kin, 75) R.L. Kingsley, R. Shrock, S.B. Treiman, F. Wilesek, Phys. Rev., D100, 1043 (1975).

(Kla, 72) S. Klarsfeld, A. Maquet, Phys. Rev. Lett., 29, 79 (1972).

(Kus, 48a) P. Kusch, H.M. Foley, Phys. Rev., 73, 412 (1948).

(Kus, 48b) P. Kusch, H.M. Foley, Phys. Rev., 74, 250 (1948).

(LcC, 56) G.W. LcCompte, H.E. Edgerton, J. of Appl. Phys., 27, 1427 (1956).

(Lee, 56) T.D. Lee, C.N. Yang, Phys. Rev., 104, 254 (1956).

(Lee, 63) R.W. Lee, J. Chem. Phys. 38, 448 (1963)., J. Chem. Phys., 35, 1451 (1961).

(Lee, 75) W. Lee, Proc. 17th Int. Conf. on High Energy Phys., London, 1974, p. IV-127.

(Lew, 75) R.R. Lewis, W.L. Williams, Phys. Lett. B, 59B, 70 (1975).

(Lov, 75) C.E. Loving, P.G.H. Sanders, J. Phys. B: Atom Mol. Phys., 8L, 336 (1975).

(Mae, 75) M. Maeda, O. Uchino, T. Okada, Y. Miyuzoe, Jap. J. Appl. Phys., 14, 1975 (1975).

(Mag, 72) G. Magyar, H.J. Schneider - Muntao, Appl. Phys. Lett., 20, 406 (1972).

(Mar, 40) H. Margenav, Phys. Rev., 57, 383 (1940).

(Mic, 65) F. Curtis-Michel, Phys. Rev., 138B, 408 (1965).

(Mil, 41) S. Millman, P. Kusch, Phys. Rev., 60, 91 (1941).

(Moo, 73) H.W. Moos, J.R. Woodworth, Phys. Rev. Lett., 30, 775 (1973).

(Mor, 52) C. Moore, Atomic Energy Levels, Vol. III, (Nat. Bureau of Standards, 1952).

(Mos, 74) A.N. Moskalev, JETP Lett. 19, 229 (1974).

(Mot, 69) H.S.W. Mott, E.H.S. Burhop, Electronic and Ionic Impact Phenomena, 2nd ed. (Clarendon Press, Oxford, 1969).

(Mck, 70) B.H.J. McKellar, Proc. 3rd Int. Conf. on High Energy Phys. and Nuc. Structure, ed. S. Devons, (Plenum Press, 1970).

(Nes, 63) A.N. Nesmayanov, Vapor Pressure of the Chem. Elements, (Elsevier, Amsterdam, 1963) p. 447.

(Neu, 76) D. Neuffer, to be published.

(Orn, 74) M.H. Ornstein, V.E. Derr, Appl. Optics, 13, 2100 (1974).

(Ott, 76) E.W. Otten, private communication (1976).

(Pen, 73) N.P. Penkin, V.P. Ruzor, L.N. Shabanova, Optics and Spectroscopy, 35, 351 (1973).

(Phi, 41) M. Phillips, Phys. Rev., 60, 100 (1941).

(Phi, 52) M. Phillips, Phys. Rev., 88, 202 (1952).

(Pla, 70) M.A. Player, P.G.H. Sandars, J. of Physics, B3, 1620 (1970).

(Pop, 70) R. Poppe, Physica, 50, 88 (1970).

(Ram, 76) N. Ramsey, Fifth International Conference on Atomic Physics, July, 1976 (Plenum Press), to be published.

(Ree, 65) E.M. Reeves, W.R.S. Garton, A. Bass, Proc. Phys. Soc. 86, 1077 (1965).

(Rei, 76) F. Reines, H.S. Gurr, H.W. Sobel, Phys. Rev. Lett., 37, 315 (1976).

(Ros, 57) M.E. Rose, Elem. Theory of Angular Momentum, (Wiley, New York; 1957) p. 62.

(Sak, 74) J.J. Sakurai, Phys. Rev., D9, 250 (1974).

(Sal, 68) A. Salam, in Elem. Particle Theory, ed. N. Svartholm, (Almquist and Forlag, Stockholm, 1968).

(San, 75) P.G.H. Sandars, Proc. Fourth Int. Conf. on Atomic Physics, (Plenum Press, New York; 1975), p. 71.

(San, 76) P.G.H. Sandars, Fifth International Conference on Atomic Physics, 1976 (Plenum Press), to be published.

(Sch, 48) J. Schwinger, Phys. Rev., 73, 416 (1948).

(Sch, 68) L.I. Schiff, Quantum Mechanics, 3rd ed., (McGraw-Hill, New York; 1968), p. 263.

(Sch. 70) R.W. Schmieder, R. Marrus, Phys. Rev. Lett., 25, 1245 (1970).

(Sch, 70) C. Schwartz, unpublished LBL preprint, Oct. 1970.

(Sch, 73) Dye Lasers, ed. F.P. Schäfer (Springer-Verlag, New York; 1973).

(Sel, 76) Beam-Foil Spectroscopy, vol. 1, ed. I.A. Sellin, D.J. Pegg, Plenum Press (1976).

(Sor, 69) P.P. Sorokin, Sci. Am., p. 30 (Feb. 1969).

(Sor, 76) D.C. Soreide, D.E. Roberts, E.G. Lindahl, L.L. Lewis, C.R. Apperson, E.N. Fortson, Phys. Rev. Lett., 36, 352 (1976).

(Sra, 69) B.B. Snavely, Proc. IEEE, 57, 1374 (1969).

(Vre, 72) Q.H.F. Vrehen, A.J. Breimer, Optics Comm., 4, 416 (1972).

(Wei, 67) S. Weinberg, Phys. Rev. Lett., 19, 1264 (1967).

(Wei, 71) S. Weinberg, Phys. Rev., D5, 1962 (1971).

(Yan, 74) T.C. Yang, Phys. Rev., D10, 3744 (1974).

(Yar, 75) A. Yariv, Quantum Electronics, 2nd ed., (John Wiley, New York; 1975) Chap. 16.

(Zel, 59) Ia B. Zel'dovich, JETP, 36, 964 (1959).

(Zer, 64) W. Zernick, Phys. Rev., 135, A51 (1964).

This report was done with support from the United States Energy Research and Development Administration. Any conclusions or opinions expressed in this report represent solely those of the author(s) and not necessarily those of The Regents of the University of California, the Lawrence Berkeley Laboratory or the United States Energy Research and Development Administration.

TECHNICAL INFORMATION DIVISION
LAWRENCE BERKELEY LABORATORY
UNIVERSITY OF CALIFORNIA
BERKELEY, CALIFORNIA 94720